UNIVERSITY OF HAMBURG

Structure of complex fluids under shear flows

Dissertation zur Erlangung des Doktorgrades

an der Fakultät für Mathematik, Informatik und Naturwissenschaften
Fachbereich Chemie
der Universität Hamburg

vorgelegt von
JOANA VALERIO

Hamburg
2018

The work described in this thesis was carried out at the Photon Science division of Deutsches Elektronen-Synchrotron, a Research Centre of the Helmholtz Association.

Gutachter/in der Dissertation:	Prof. Dr. G. Grübel
	Prof. Dr. H. Weller
Gutachter/in der Disputation:	Prof. Dr. H. Lange
	Prof. Dr. M. Fröba
	Prof. Dr. G. Grübel
Datum der Disputation:	05.10.2018

Abstract

With the recent developments of modern synchrotron and X-ray Free Electron Laser (XFEL) light sources high speed and micrometer sized liquid jets have become one of the most important sample delivery systems. For that reason it is highly important to develop liquid jet devices compatible with micrometer X-ray beams, which are optimized for the investigation of nanostructures and the behavior of complex liquids behavior under flow.

This thesis reports a detailed X-ray scattering study of a liquid jet produced by a gas dynamic virtual nozzle (GDVN) system. Due to the very special microjet formation mechanism these injection devices offer a unique possibility to perform rheological studies at very high shear rates.

In the framework of this thesis two main topics have been studied:

1. The behavior of spindle-shaped hematite particles in a GDVN produced flow by WAXS.

2. The impact of microjet and microdroplet geometries on the scattering patterns by SAXS.

Therefore, an existing experimental setup was improved in accordance with the demands of the experiments at PETRA III, P10 beamline.

The WAXS study shows a pronounced alignment of spindle-shaped particles parallel to the flow direction. The particles' alignment is found to be depend on the particles' aspect ratio, the used flow rates and the nozzle diameter. The degree of orientation of the particles was quantified by modeling Debye Scherrer rings describing the behavior of the spindles along and across the microjet and the microdroplets. Hematite particles show a decrease in alignment downstream the nozzle tip and no orientation was detected in the droplets regime. The degree of alignment was studied with increasing distance from the nozzle tip. The observed loss of alignment is far higher than expected from simple rotational diffusion. The difference between these two values indicates that the particles behavior is dominated by the flow and shear cessation.

The second topic of this work is a SAXS study on the impact of microjets and microdroplets geometries on the scattering patterns. A detailed map on the scattering signal was created taken along and across the jet resulting in different diffractions patterns which arise from the different jet geometries. The experimental findings were successfully modeled suggesting that both, micrometer-beam-sizes and micrometer-jet-sizes have to be taken into account in describing the results of the SAXS experiments.

Zusammenfassung

Durch die jüngsten Entwicklungen moderner Synchrotron-Quellen und Freie-Elektronen-Laser im Röntgenbereich sind Liquid Jets im Größenbereich von Mikrometern zu einer der wichtigsten Probenumgebungen geworden. Aus diesem Grund ist es von großer Wichtigkeit, Liquid Jet-Systeme zu entwickeln, die mit einem Röntgenstrahl im Mikrometerbereich kompatibel sind, der für die Untersuchung von Nanostrukturen und dem Verhalten fließender komplexer Flüssigkeiten optimiert ist.

Die vorliegende Arbeit beschäftigt sich mit einer detaillierten Röntgenstreustudie von Liquid Jets, die durch ein "gas dynamic virtual nozzle" (GDVN)-System erzeugt werden. Wegen des besonderen Mechnismus der Entstehung des Mikrojets bieten solche Injektionsvorrichtungen eine einzigartige Möglichkeit, rheologische Untersuchungen bei sehr hohen Scherraten durchzuführen.

Im Rahmen dieser Arbeit wurden hauptsächlich zwei Themenkomplexe untersucht: 1. Das Verhalten von spindelförmigen Hämatit-Partikeln in einer von einem GDVN-System erzeugten Strömung mit Hilfe von Röntgenweitwinkelstreuung (WAXS). 2. Die Auswirkung der Mikrojet- und Mikrotröpfchengeometrien auf das Streubild im Bereich der Röntgenkleinwinkelstreuung (SAXS). Hierzu wurde ein bereits existierender Versuchsaufbau verbessert, um ihn für Experimente an der Beamline P10 bei PETRA III zu optimieren.

Die WAXS-Studie zeigt eine ausgeprägte Ausrichtung der spindelförmigen Partikel parallel zur Strömungsrichtung. Die Orientierung ist dabei von dem Halbachsenverhältnis der Partikel, der Strömungsgeschwindigkeit und dem Düsendurchmesser abhängig. Die Stärke der Ausrichtung der Partikel wurde durch Modellierung von Debye-Scherrer Ringen quantifiziert, die das Verhalten der Spindeln entlang des Mikrojets, quer durch diesen hindurch, sowie innerhalb der Mikrotröpfchen beschreiben. Die Partikel zeigen eine abnehmende Ausrichtung mit zunehmender Entfernung von der Düsenspitze und keine bevorzugte Orientierung innerhalb des Tröpfchenregimes. Der Grad der Orientierung wurde mit zunehmendem Abstand von der Düsenspitze untersucht. Die beobachtete Abnahme der Ausrichtung ist dabei viel höher als bei reiner Rotationsdiffusion zu erwarten wäre. Der Unterschied deutet darauf hin, dass das Verhalten der Partikel von der Strömung und dem abrupten Erlöschen der Scherkräfte dominiert wird.

Das zweite Thema dieser Arbeit ist eine SAXS-Studie zur Auswirkung der Geometrien von Mikrojets und -tröpchen auf das erhaltene Streubild. Es wurde eine detaillierte Abbildung von Streusignalen, die durch verschiedene Jetgeometrien hervorgerufen werden, entlang und durch den Jet hindurch erstellt. Die experimentellen Ergebnisse konnten erfolgreich modelliert werden und suggerieren, dass sowohl die Größe des Röntgenstrahls als auch die Größe des Liquid Jets im Mikrometerbereich bei der Auswertung von SAXS-Experimenten berücksichtigt werden müssen.

To baby M.

Contents

List of Figures

List of Tables

Introduction

Liquid jets form a subset of free-surface flows and play an important role in many practical applications, for example, ink jet printing, engineering, agriculture, fuel injection, DNA sampling and medical applications. Jets can also be found in many areas of our daily life, such as irrigation systems, showers, perfumes or deodorants and sprayers.

With the recent developments of modern synchrotron and X-ray Free Electron Laser (XFEL) light sources, exciting possibilities arise, such as studies of structure and dynamics of soft condensed matter with unprecedented spatial and temporal resolution.

In the experiments with these new types of X-ray sources, the high speed and micrometer sized liquid jets have become one of the most frequently used sample delivery systems for several reasons. Most importantly, a jet is a fast and steady stream injection system that refreshes the sample permanently avoiding extensive radiation damage.

The X-ray scattering experiments, in particular those using FEL beams on radiation sensitive samples, such as complex liquids and macromolecules, are nowadays typically performed with these steady streaming liquid jets. For that reason it is highly important to develop liquid jet devices compatible with micrometer X-ray beams, which are optimized for the investigation of nanostructures and the behaviour of complex liquids in flows.

Gas dynamical virtual nozzles (GDVN) are the sample injection system used in the framework of this thesis. Due to the mechanism of jet collimation and the small dimensions in microfluidic environments very high pressures and high shear forces are created that influence the liquid jet behavior and the sample system under investigation. This exceeds shear rates present in standard rheology approaches by at least two orders of magnitude, allowing for studies under extreme conditions from the sheared to the unsheared regimes.

This thesis focuses on the rheological properties of colloidal suspensions in GDVN produced flows by studying the behavior of anisotropic particles under shear flow using a Wide Angle X-ray Scattering (WAXS) setup. As a sample system, aqueous dispersions of spindle-shaped hematie particles were used, whose alignment is known to be sensitive to shear flows. In this work the results of a detailed study of the degree of orientation of the particles along and across the jet is presented. Special attention is paid on particles with different aspect ratios.

This thesis contributes as well to an understanding of the impact of the jet geometries on the scattering patterns obtained by Small Angle X-ray Scattering (SAXS). A detailed characterization of the scattering signal collected along and across the microjet and microdroplets is shown using both experimental and simulated data.

In order to address all these questions, a liquid jet setup was optimized in the framework of this thesis and the upgrade it is presented. While in this thesis more attention has been given to rheological studies, the described setup can be used in a wide range of liquid jet experiments.

This thesis is structured as follows:

Chapter 1 describes an introduction to liquid jets and some of the major contributions to the liquid jets' stability field. The different kinds of liquid jets used in X-ray scattering experiments and the construction of a GDVN are discussed as well as advantages and disadvantages of a GDVN.

Chapter 2 deals with the physical properties of liquid jets and their production and stability.

Chapter 3 describes the rheological properties of fluids and gives a short overview on nano-particles in shear flows.

Chapter 4 contains SAXS and WAXS theory used to study the alignment of the particles under flow. Furthermore, a short overview on the model of spindle-shaped particles is given in order to describe their alignment.

Chapter 5 presents the details of sample preparation and characterization using transmission electron microscopy (TEM), high resolution transmission electron microscopy (HRTEM), selected area electron diffraction (SAED) and X-ray diffraction (XRD).

Chapter 6 gives the experimental details used during the experiments. This includes information on the setup emphasizing the upgrades performed in the framework of this thesis and a short overview of the P10 beamline at PETRA III.

Chapter 7 is focused on the analysis of the behavior of spindle-shaped hematite particles under flow measured by WAXS.

Chapter 8 reports a detailed SAXS study, mapping the microjet and microdroplets regions of pure water and hematite dispersions. The impact of the jet geometries using experimental data and computational model studies is also described.

Chapter 9 presents the conclusions and outlook.

Chapter 1

Liquid jets - A review

Jets are collimated steady streams of matter with a columnar shape that break-up into droplets, a phenomenon occurring from micrometers up to a large scale structures. Liquid jets play an important role in many applications of our daily life, for example, water running in our taps, perfumes, sprayers, irrigation systems, etc. Technologically these systems can be found in many practical applications such as ink jet printing, diesel engines, agriculture, manufacturing, coating and in medicine as targets for drugs delivery [1].

With the advent of modern light sources producing intense X-ray beams from micro-nanometer sizes new types of experiments using liquid jets injection systems were enabled such as the study of structure and dynamics of liquids and soft condensed matter.

In this chapter, a short overview of the scientific history of liquid jets and Gas Dynamical Virtual Nozzles (GDVN) based devices for X-ray scattering experiments is presented.

1.1 History of jets and their stability

A liquid jet can be described as a cylindrical column of fluid with instabilities travelling along its surface that lead to its disaggregation into droplets.

The investigation of liquid jets goes back to the 15^{th} century when da Vinci studied their behavior and break-up. He reported that the force of gravity is responsible for water dropping from a orifice, see Figure 1.1, illustrating the first studies with jets [1]. The same argument was debated later in 1686 by Mariotte [17]. Both authors suggested that cohesive forces provide a certain tensile strength of water, which has to be overcome by gravity during the jet break-up [1].

The first experimental observation of liquid jets and the instabilities along their surface was achieved by Savart, see Figure 1.2. He illuminated the jets with a sheet of light and examined the decay of liquid jets into droplets concluding that the break-up depends only on inherent properties of fluid motion [1]. Later in 1849, it was discovered by Plateau that surface tension is the actual source of instabilities which reduces the surface area of the jet leading to droplet formation.

In 1878 Rayleigh showed the first mathematical analysis of the mechanism responsible for instabilities of liquid jets [18]. He studied inviscid jets and introduced a linear temporal stability analysis

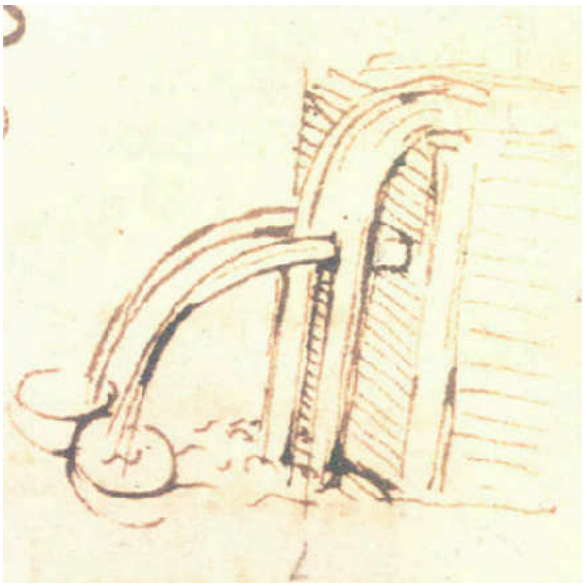

Figure 1.1: Sketch by Leonardo da Vinci from Codex Leicester [1].

for an infinitely long cylindrical column of incompressible fluids by including surface tension. Concluding that waves with wavelength larger than the undisturbed jet circumference are unstable and thus grow and break the jet. Thus a good agreement was achieved between the Rayleigh's theory and Savart's experimental results.

Weber extended Rayleigh's analysis in 1931 by including the influence of viscosity on the stability of a liquid jet under the influence of surface tension. He showed that for a given liquid and nozzle radius, the break-up length of the jet depends linearly on its velocity. He also observed that the wavenumber of the most unstable mode increases with viscosity. Thus, larger droplets are formed at smaller flow rates leading to an increased break-up time [18].

Keller and coworkers [19] observed the impact of disturbances at an orifice, introducing the spacial instability analysis, which deals with instabilities that propagates in space. Therefore the linear temporal stability analysis which governs the initial stages of the jet break-up, fails to predict the formation of satellite droplets. Assuming that the size of the droplets is approximately equal to the wavelength of the disturbance. The behavior of satellite droplets was investigated afterwards, theoretically and experimentally, by Pimbley and Lee [20] in 1980.

Peregrine et al. (1990) found that the break-up behavior of a liquid jet depends highly on three internal properties of the jet: the density, the surface tension and the viscosity.

Figure 1.2: Figure from Savarts' original paper, showing the formation of primary and satelite droplets and oscillations when the jet breaks up[1].

The non-linear nature of the instability, as it is understood nowadays was studied by Hilbing and Heister in 1996 using a boundary element method. They showed that the size and the formation of the satellite droplets depends on the magnitude of disturbance, the Weber number We and the wavelength.

At the break-up, the jet radius goes to zero while the velocity of the jet goes to infinity, which results in a singularity in the solution of the liquid jet equations. These singularities were studied by Eggers' who used Navier-Stokes equations to derive a one-dimensional model describing the break-up region [21].

Understanding the behavior of the liquid jets and the physical parameters behind them is essential to study the different topics related to the flows. As showed from this short overview, the jet, break-up and droplet regimes depend on the viscosity, density and surface tension on the jet, therefore, the knowledge of the jet properties is crucial to study its performance in different injection devices [22]. Thus to develop or upgrade the design of the new sample injection systems these liquid properties should be taken into account.

The use of different injection devices became important with the advent of microfocused X-rays at Free Electron Lasers and synchrotron sources. These sample environments are very important in the control of the jets, samples and flow studies. In the next section a brief description of different injection devices for liquid jets production employed in the X-rays scattering experiments will be presented.

1.2 Liquid jets for X-ray scattering experiments

The emergence of modern X-ray scattering techniques together with different sample environments results in the development of novel injection systems. New types of sample injection devices used in X-ray scattering experiments allow for a precise control over time, sample and alignment, offering numerous advantages:

1. The possibility to have background-free measurements.

2. Micro-channel devices can mimic better the real sample environment and provide additional structural resolution of samples.

3. Small channel sizes scale down the sample volume allowing higher accuracy in chemical analysis [23], biotechnology [24] and drug discovery [25].

4. The radiation damage issue is overcome due to the continuous flow of the sample [26].

Various sample delivery systems for X-ray scattering experiments were developed to study different samples properties with high precision and control. Some of these injection techniques will be reviewed over the course of this chapter:

Electrospinning microjets In the electrospinning microjet, the liquid is focused by electrostatic forces, where an electrostatic fiber accelerates the liquid, to form the microjet [27]. Thus, the jet has to be charged to interact with the electric fields. Therefore this method requires a liquid sample with a polymer solution since it facilitates the electro spinning. However the presence of the polymer turns out to be a limitation for this type of injectors as well as for the high flow

rates, since these samples tend to have higher viscosities. Although, they are easy to operate in vacuum.

Rayleigh nozzle The Rayleigh nozzle produces a free standing continuous and cylindrical liquid jet formed by simply forcing the liquid through an orifice with sufficient velocity. Since the jet has a higher surface free energy than droplets, it tends to break up after a certain break-up length *L*.

The Rayleigh nozzles are the simplest type of injection devices that can produce a stream as wide as its nozzle, and operate a flow of droplets, whose theory dates back to Rayleigh in 1878 [18]. In Figure 1.3 a) the nozzle principle is shown where the liquid is pressed from a reservoir with a pressure P and flows through an exit orifice of the nozzle.

Supersonic microjets - Supersonic microjets are a special case of Rayleight jets. As the jet's name indicates this liquid microjets are accelerated up to v_{jet} = 850 m/s and their lifetime is in the order of few ms. When a laser beam heats up the capillary a small portion of the liquid evaporates and expands, afterwards the remaining liquid gets accelerated and forms a microjet [28–30].

Gas dynamic virtual nozzle In order to obtain jets sizes in the order of μm, Gañán-Calvo $et\ al.$ [31] developed a flow focusing nozzle, formed by a cone shaped glass tube with a concentric micro tube for liquid. This nozzle design is called "Gas-dynamic virtual nozzle" (GDVN) or "flow focusing" nozzle, where a co-flowing gas stream is used to establish a steady tip streaming. Therein the tangential stress, viscosity and surface tension result in a meniscus until a microjet is emitted, see Figure 1.3 b). This technique generates a continuous cylindrical liquid jet of diameters down to the micrometer-regime with break-up length L of thousands of μm. These nozzles use far less sample material than the standard Rayleigh jet at typical flow rates from 1 to 50 μl/min. The liquid jet produced by a GDVN behaves similar to Rayleigh jets breaking up into a stream of droplets.

In order to improve some aspects of flow focusing nozzles such as ice formation on the nozzle tip, more control during the nozzle production, access to lower flow rates and clogging problems, different nozzles based on GDVN principle were developed (see descriptions below):

Microfluidics devices - Microfluidic injection nozzles present GDVN technology which enables reliable and essentially clogging-free jetting over long periods of time.

These microfluidic devices are based on an open nozzle geometry and produce μm sized (0.9 - 5 μm) liquid jets at very low flow rates under atmospheric or vacuum conditions. These devices are fabricated by using soft lithographical techniques which enable precise and reproducible micro-channel design control, what is critical for the liquid jet optimization at low flow rates. Contrary to the typical glass nozzles, lithographic nozzles are easier to produce within only one production step by the simple integration of the additional microfluidic features or different nozzle geometries.

Nowadays the most commonly used material for the production of lithography nozzles is PDMS (Polidimethylsiloxane) which exhibit controllable elasticity and non-toxicity as well as excellent optical transparency and permeability [32–35]. The principal drawback of these microfluidic nozzles is the strong scattering signal scattered from the nozzle tip which preclude X-ray scattering measurements at the jet formation.

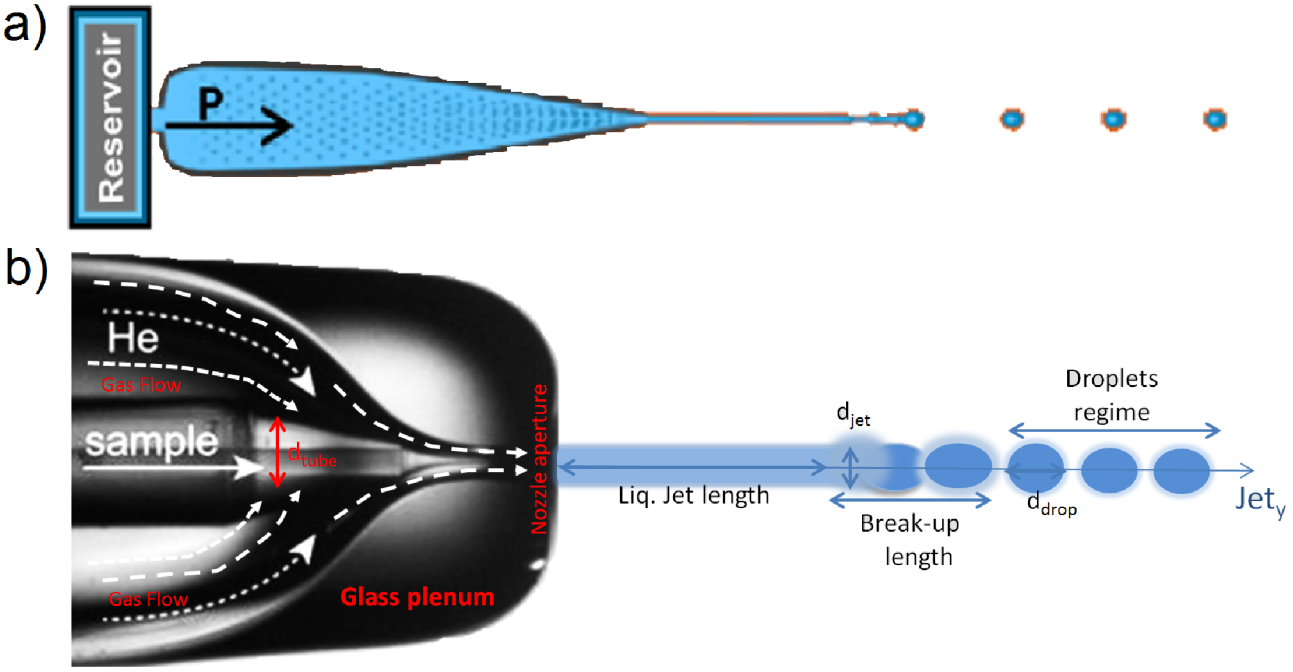

Figure 1.3: Scheme with two different kinds of liquid jets nozzles. a) Rayleigh nozzle, adapted from [2]. b) Glass GDVN Nozzle, d_{jet} and $d_{drop.}$ is the definition of jet and droplet diameter, respectively while d_{tube} is the inner tube diameter.

Double flow-focusing nozzles - The Double flow focusing nozzles (DFFN) are a GDVN technique as well, in which an inner liquid jet (sample liquid) is focused by a faster outer liquid jet, which in turn is focused by a gas flow, see the scheme of Figure 1.4 a). The meniscus of the outer jet is shaped into a jet similar to the classical GDVN. The inner jet is guided into the meniscus of the outer jet and these two jets form a laminar flow without mixing, depending on the system in use. The sample consumption is lower in this nozzle design compared to the classical GDVN. For more details about nozzle construction see ref. [36].

3D printed nozzles -

3D printing seems to be a promising technology for the future development of the GDVN, improving the reproducibility and reliability of the gas aperture of the nozzle further from the rotation melting process. 3D printed nozzles are based in a GDVN principle, allowing for μm resolution. Ideally 3D printing allows for a perfectly built gas aperture, within a μm range size, as well as a perfect cone-shaped form required for the exterior glass. The 3D printing technique uses a die and other materials such as polymers and ceramics for the nozzle fabrication. Since every part is designed separately and in a control manner this method gives the flexibility to produce the desired geometries and dimensions [37].

Different injection techniques, as the drop on command technology, due to their properties, see below, are mostly employed to ionic liquids studies such as water in supercooling regimes probed by X-ray scattering. During the framework of this thesis the initial implementation steps were performed in order to have an alternative sample injection system in our group [8].

Drop on Demand Systems Drop on demand systems describe a class of injectors that produces single uniform and equidistant droplets, instead of a continuous jet of liquid. The nozzle operational principle as well as the droplets formation mechanism are presented in Figure 1.4 b). The droplets formation can occur by acoustic levitation [38] or by piezo triggered droplets ejection. As an alternative to continuous stream injectors, the drop on demand systems consume a reduced amount of sample and the size of droplets can be uniform.

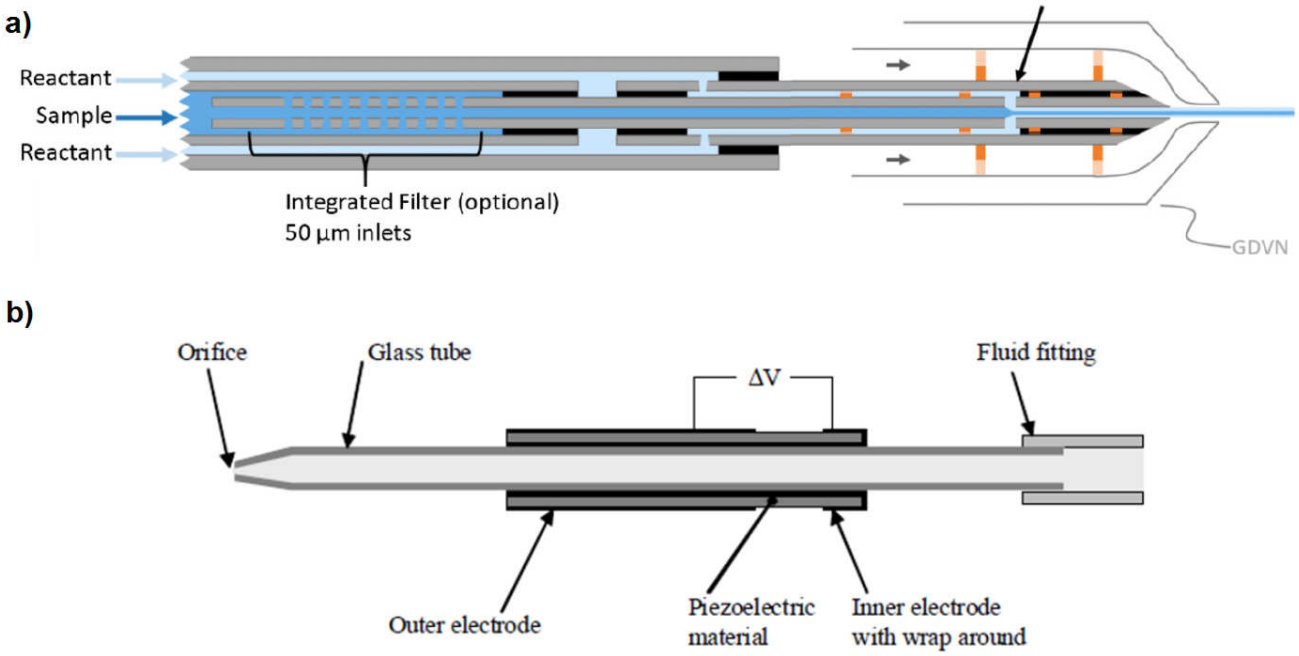

Figure 1.4: Scheme of two different nozzles. a) Double-flow focusing nozzle and b) Piezo nozzle. Images adapted from [2, 3], respectively.

The choice of the injection device system depends on the experimental techniques to be used as well as some requirements that have to be taken into account. In the framework of this work, glass nozzles based on the GDVN principle were chosen due to their characteristics:

- GDVNs form μm sized jets whose dimensions can be tuned.
- GDVNs form jets with high stability. Thus these nozzles can run stable over several hours, which is an important requirement for X-ray experiments.
- The stability of these jets in high vacuum environments is also an important requirement for X-rays experiments in order to reduce the background scattering.

- A GDVN offers different operating modes such as dripping, and jetting. The jet and dripping mode offer the possibility to measure at different jet regimes which makes them promising for different types of experiments.
- The jet collimation mechanism used by GDVN produces higher shear rates allowing for studies of sample's behavior in different flow regimes.

In this thesis different glass GDVNs were produced to study the behavior of different complex fluids in flows. The main steps of fabrication as well as the common GDVN issues faced along this project will be presented in detail in section 6.2.1.

Chapter 2

Physics of liquid jets

When a cylindrical liquid jet exits a circular nozzle, the jet structure is determined by forces acting on the jet surface giving rise to the disintegration of the jet. Understanding these processes is crucial for a wide range of applications involving liquid jets. The complexity of the fluid mechanics is high for a satisfactory mathematical description. Thus additionally to the theory, several methods and dimensionless flow parameters are used to characterize the liquids jet.

In this chapter, an overview of the phenomena that influence the jet regimes and the structure of the jet is presented. A detailed jet characterization based on dimensionless flow parameters will be discussed as well as some process that determines the jet break-up process, jet length and droplets sizes.

2.1 Flow characterization

The dynamics of fluids on microscopic scales is found to be significantly different from what is observed at a macroscopic scale. At small scales the surface area to volume ratio becomes large and consequently increases the effect of surface and interfacial properties.

When a cylindrical liquid micro-jet exit a circular nozzle, the jet structure is determined by the cohesive and disruptive forces acting on the jet surfaces. These instabilities can become amplified and give rise to the jet break-up [39, 40].

To understand the liquid jet behavior and describe the process behind its disintegration we consider a viscous liquid jet emerging from an aperture a which describes the different diameters of the microtubes used (10 μm $-$ 50 μm were used in this work). A jet meniscus b is pulled out by a pressure gradient ΔP_g which is defined as the difference between gas P_g and liquid pressure P_l, see Figure 2.1 a). In the case of the GDVN glass nozzles used in this thesis the gas is Nitrogen N_2 with pressures from 65 bar $< P_l <$90 bar and the gas used to focus the sample is Helium He for 15 bar $< P_g <$ 25 bar. A recent study showed that the use of different focusing gas influences the jet properties, showing that He is the most suitable gas to produce a thin, long and fast jet [41].

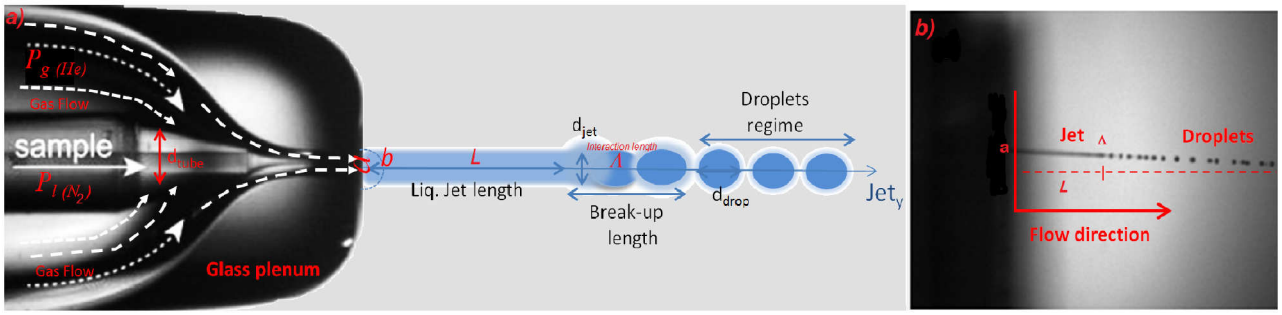

Figure 2.1: a) Illustration of a liquid jet formed by a GDVN. b) Microscope image from a liquid jet being ejected from a nozzle under a vacuum atmosphere a is the aperture of the nozzle, b the jet meniscus and L the jet length. In the droplets regime, Λ is the interaction length.

After a certain jet length L the jet breaks-up into droplets. These droplets are formed at an interaction length Λ where the jet diameter goes to zero and the jet breaks up. When $L > \Lambda$ an undisturbed jet is formed, while if $L < \Lambda$ only droplets are formed.

Assuming high pressure gradients towards the nozzle, the jet diameter can be calculated by:

$$d_j \simeq (\frac{8\rho_1}{\pi^2 P_l})^{1/4} \mathrm{Q}^{1/2} \tag{2.1}$$

where ρ is the fluid density and Q the applied flow rate. Note, that the equation 2.1 is independent of nozzle parameters, viscosities of liquid and gas or liquid-gas surface tension. However it has been successfully applied experimentally for GDVN [7, 31].

Depending on the type of flow, different dimensionless parameters are often used to describe the break-up mechanisms and the jet instability. In the case of collimated-jets four independent parameters will be introduced:

Reynolds number

The Reynolds number is a fundamental dimensionless number which describes the ratio between the inertial and viscous forces and is used to predict the fluid flow [42]:

$$Re = \frac{\text{inertial forces}}{\text{viscous forces}} = \frac{\rho \upsilon d}{\eta} \tag{2.2}$$

where υ denotes the flow velocity, ρ liquid density, d is the nozzle internal diameter and η the liquid viscosity. Re is an indicator of the probability of a flow being turbulent. Higher Re numbers indicate a turbulent flow and consequently an unstable liquid jet. Below a critical value, $Re_{crit} = 2040$ [43], the flow will be laminar. However, the onset of turbulence in nozzles have been reported to start at $1000 < Re_{crit} < 18000$ [5, 44].

As an example, for a laminar stable flow of water injected from a 5 μm to 20 μm diameter GDVN small Reynolds numbers ranging from Re = 250 to 1200 are expected [45].

Péclet number

The Péclet number determines the ratio of the shear motion and the Brownian motion. The Péclet number Pe is a class of dimensionless numbers relevant in the study of transport phenomena in a continuum moiety. It is defined to be the ratio between the shear rate $\dot{\gamma}$ and the particle diffusion coefficient D_r of Brownian motion [46]:

$$Pe = \frac{\dot{\gamma}}{D_r} \tag{2.3}$$

is a dimensionless flow parameters used to describe the physical mechanisms that affects the way of jet break-up into droplets.

We note that:

- $Pe > 1$ - High shear rates, where shear forces dominate.
- $Pe < 1$ - Low shear rates, where diffusion dominates.

In the framework of this project, the studies were performed at low Re, which is typically the case for small jet dimensions and low flow rates, as required to produce a laminar jet and high Pe achieved by high shear rates, leading to a flow alignment of anisotropic particles.

Weber Number

The Weber number is a dimensionless number in fluid mechanics that is often useful to analysing fluid flows where there is an interface between two different fluids, especially for multiphase flows with strongly curved surfaces.

We_L is the ratio between the inertial forces of the fluid compared to its surface tension, is a very useful number to quantity thin film flows and the formation of droplets, defined as:

$$We_L = \frac{\text{inertial forces}}{\text{surface forces}} = \frac{\rho v^2 d}{\sigma} \tag{2.4}$$

where σ is the surface tension.

The influence of the surrounding atmosphere on the liquid jets properties is very important and is measured via the atmospheric Weber Number, We_A, by the following expression:

$$We_A = \frac{\rho_A v^2 d}{\sigma} \tag{2.5}$$

where ρ_A is the density of the surrounding atmosphere. It was shown that parameters $1 < We_A < 5$ start to influence the jet break-up [47, 48].

A short overview on the jet stability will be shown in the next sections, where the different mechanisms which affect the jet's stability are shown.

2.2 Jet stability - phenomenological description

The jet stability is perturbed by continuous disturbances which travel along its surface, such as fluctuations in pressure or density, which grow along the jet surface and lead to its disintegration into a series of droplets. During this process the jet radius near the break-up becomes small and the associate velocity diverges to infinity.

Reitz and Bracco [49] discuss the various mechanisms associated with the jet instability and consequently the break-up of liquid jets. However, no single mechanism is considered responsible for all jet breakup process, but a combination of factors is postulated to be involved. Concerning this different mechanisms, the jet break-up is classified into four primary modes:

1. The Rayleigh regime
2. The first wind-induced regime
3. The second wind-induced regime
4. The atomization regime

Rayleigh and the first wind-induced regime, are both characteristic for lower speed-jets, large jet lengths and droplets size close to the nozzle orifice diameter, while atomization and the second wind-induced regimes are typical from higher speed-jets with smaller jet lengths and consequently small droplets diameters. A fifth regime can also be described, the liquid dripping mode, as the most elementary mode of drop formation, characterized by very low flow rates and uniform and large droplets sizes. For more detailed information about characteristics of the different kind of break-up regimes see [4, 49, 50].

In Figure 2.2 a classification of the different break-up regimes is presented by the study of the break-up length as a function of jet speed. The initial part (ABC) is called drip-flow regime, where only a train of droplets is formed, because the jet speed is not enough to create a jet. The jet is formed in point C. Here the jet length increases almost linearly with the jet velocity up to the jet break-up (D). Region CD is known as Rayleigh break-up, or Rayleigh regime where the break-up of the jets is dominated by the surface tension forces well described by Rayleigh and Webber [18]. The drop radius formed is about twice the one of the liquid jet diameter (more details will be given in section 2.3.1). The longest possible jet (E) is formed at the so-called jet speed V_c. After V_c any further speed increase results in shorter break-up lengths, until point F is reached. The resulting region DEF is called Wind-induced break-up. Beyond point F only spray is detected - Atomization regime, characterized for large atmospheric interactions. The droplets appear to be stripped off from the surface rather then pinched off by segments. As the jet velocity increases beyond point G the entire jet is completely atomized except near the nozzle tip. The average radius of the droplets in the spray decreases with the inlet jet velocity. The description of the dynamics of Newtonian fluids (as studied in this work)

are based on the conservation of energy, mass and momentum, the so called Navier-Stokes equations.

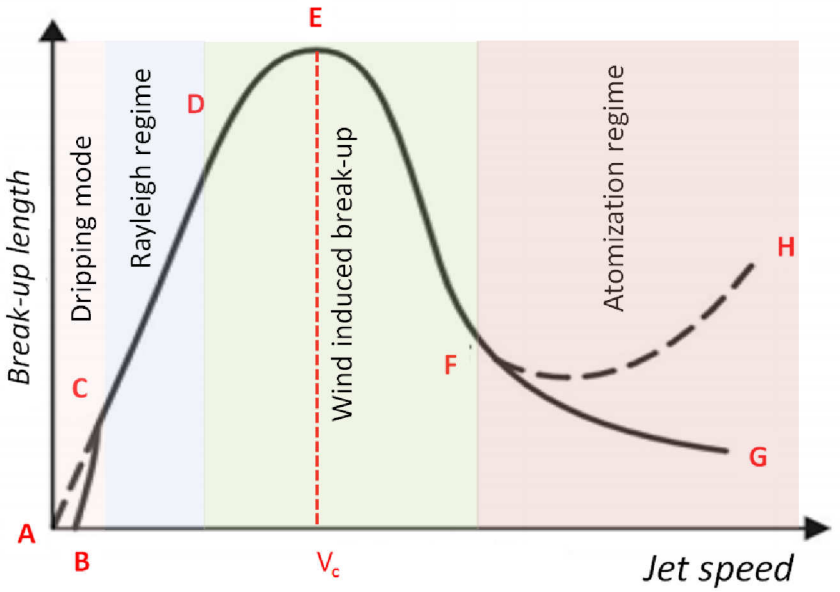

Figure 2.2: Jet stability curve presenting the variation of break-up length as a function of jet speed (Adapted from [4, 5])

These equations can be applied to study the influence of the flow parameters on the jet break-up, yielding [43, 51]:

- Momentum equation:

$$\rho_i(\frac{\partial}{\partial \mathrm{t}} + \upsilon_i \cdot \nabla)\upsilon_i = -\nabla P_i, \tag{2.6}$$

- Mass equation:

$$\frac{\partial}{\partial \mathrm{t}}\rho_i + \nabla \cdot (\rho_i \upsilon_i) = 0, \tag{2.7}$$

- Energy equation:

$$(\frac{\partial}{\partial \mathrm{t}} + \upsilon_i \cdot \nabla)e_i - Pi(\frac{\partial}{\partial \mathrm{t}} + \upsilon_i \cdot \nabla)\frac{1}{\rho_i} = 0, \tag{2.8}$$

$$P_i = P_i(\rho_i, T_i)\ (i = 1, 2), \tag{2.9}$$

where $i = 1, 2$ is, respectively, the jet fluid and the ambient fluid, ρ is the density, υ is the velocity, e is the internal energy per unit mass, t is the time, T is the temperature and P the pressure. The equation (2.9) is known as "equation of state".

The equations above can be applied to an incompressible Newtonian fluid describing its velocity field. If stationary conditions are assumed, as a laminar flow in a device, the Navier-Stokes equation

is given by:

$$\rho(\upsilon_i \cdot \nabla)\upsilon_i = \eta\nabla^2\upsilon_i - \nabla P_i + \mathrm{F}, \tag{2.10}$$

$$\rho\nabla \cdot \mathrm{u} = 0, \tag{2.11}$$

With $\rho(\upsilon_i \cdot \nabla)\upsilon_i$ being representative of inertia, and $\eta\nabla^2\upsilon_i - \nabla P_i$ represents the stress forces per volume due to the viscosity and pressure gradient. F is the volume force. Equation 2.11 is known as continuity equation which should be applied to an incompressible fluid taking into account mass conservation.

Under certain conditions, such as the microjet dimensions or very small nozzles diameters as the GDVN and the jets studied in this work, the influence of shear from the fast-flowing gas streams on the liquid surface increases. Thus the equations described above are not neglectable and Re and We number can became inaccurate.

Vega $et\ al.$ studied the stability of GDVN jets identifying 3 different regions, see Figure 2.3 [7]:

- Global instability regime - described by the instability of the liquid meniscus, no jet formation.
- Local instability regime - described by the stability of the liquid meniscus but unstable jet.
- Steady jetting - describes the stability of both, liquid meniscus and jet.

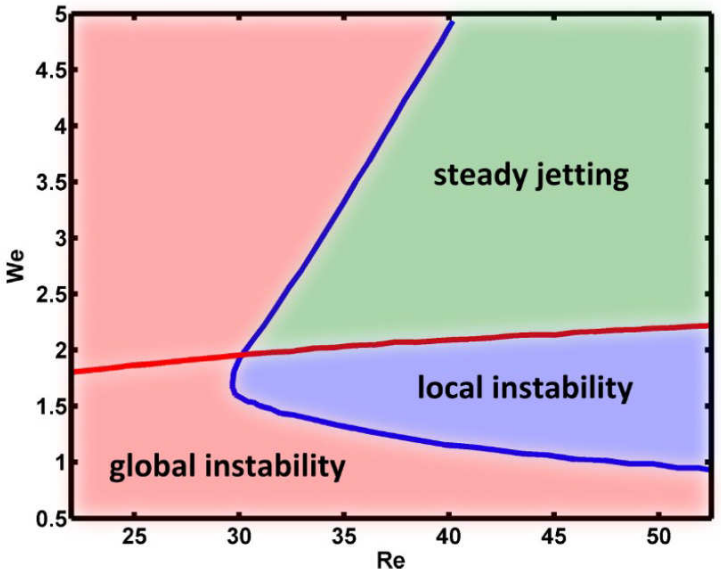

Figure 2.3: Reynolds and Weber number diagram. The red curve shows stability-instability transition achieved for capillary jets [6] and the blue curve the transition obtained for GDVN produced jets using low flow rates [7].

Figure 2.3 presents a comparison between the stability-instability transition achieved for capillary jets [6] with the curve obtained for GDVN produced jets using low flow rates [7].

The different regions in the $We - Re$ diagram are thus, dependent on the nozzle geometry and consequently on the flow parameters used for the jet formation [7].

2.3 Physical break-up mechanisms

Free standing liquid jets are inherently unstable, thus the instability of a jet prior to the break-up is of special importance. There are several different physical mechanisms that affect the way of how jets break up into droplets where a few of these will be discussed in the next sections:

2.3.1 Surface tension

The first analysis of the mechanism of instability in jets, performed by Rayleigh, showed that capillary jet break-up is caused by surface tension and the capillary wave modes increase in time [18]. The linear instability of a cylindrical column of an inviscid fluid can be modeled by assuming that the jet is in an equilibrium state to which small disturbances are imposed. The jet radius is defined by:

$$r = s + \delta \cos(kx) cos(m\theta), \tag{2.12}$$

where r is the disturbed jet radius, s is the original jet radius, k is the wave number, m is an integer, δ is the initial disturbance, σ is the azimuthal coordinate and x is the axial length.

By using the standard equation of motion and considering the wave mode of the form $\exp(\lambda t + i(kx + m\theta))$, being t the time and λ the wavelength. Rayleigh developed an eigenvalue relation given by:

$$\lambda^2 = \frac{\sigma(ks)}{\rho s^3}(1 - m^2 - (ks)^2)\frac{I'_m(ks)}{I_m(ks)}, \tag{2.13}$$

where ρ is the density of the fluid, σ is the surface tension, and $I_m(ks)$ is a modified Bessel function of order m. If $m \neq 0$ disturbances are neutral when the growth rate $Re(\lambda) = 0$, meaning that λ is the imaginary part and waves will be stable for $Re(\lambda) > 0$. The case of $m = 0$ yields to positive values of $Re(\lambda)$ corresponding to a growing amplitude for $0 < Re(\lambda) < 1$. Thus the Rayleigh "mode of maximum instability", corresponds to the maximum value of $Re(\lambda)$ for all k.

The Bessel equations are used to obtain Rayleigh's classical formula for an inviscid infinite circular cylinder of fluid:

$$\lambda^2 = \frac{\sigma(ks)}{\rho s^3}(1 - (ks)^2)\frac{I_1(ks)}{I_0(ks)}. \tag{2.14}$$

The maximum growth rate is at ks =0.697 which leads to an interaction length of the capillary waves of λ = 9.01 with $\lambda = 2\pi/Ks$, see Figure 2.4. The characteristic break-up time, t_b can be found by taking the inverse of the growth rate as, $Re(\lambda) = 0.34(\sigma/\rho s^3)^{1/2}$, which yields:

$$t_b = 2.94(\frac{\rho s^3}{\sigma})^{1/2}. \tag{2.15}$$

Rayleigh equated the volume of the jet cylinder over one wavelength of the most amplified wave with that of a sphere of radius R to give an estimate of the size of the drop resulting from the jet break-up

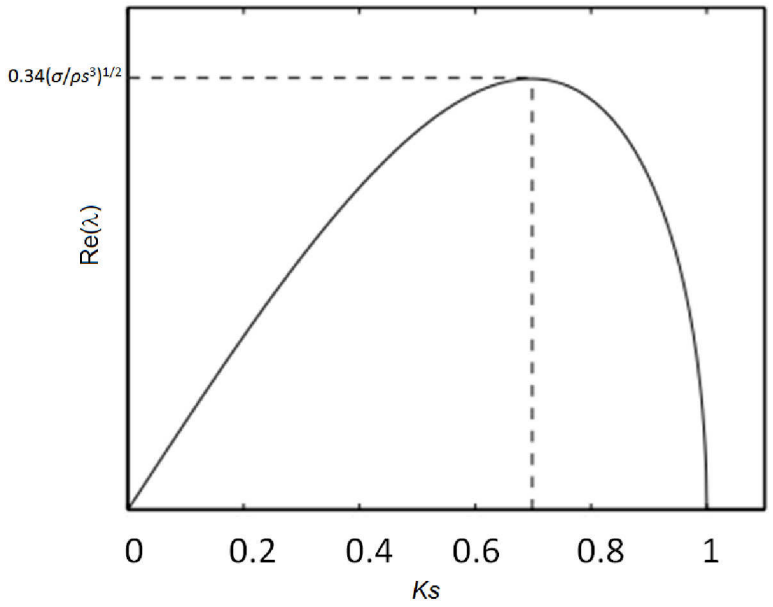

Figure 2.4: Wavelength as a function of temporal growth rate. (Adapted from [4])

as:

$$r_{droplet} = 1.89.r_{jet}, \tag{2.16}$$

where r_{jet} and $r_{droplet}$ are the radius of the jet and droplets respectively. This Rayleigh assumption is used to characterize the droplets dimensions produced by Rayleigh jets. In the case of jets formed by GDVN (nozzles used in the framework of this thesis) the shear created between the jet-gas interface should be taken into account.

The shear impact on the capillary waves was analysed first by the so-called Helmholtz-Kelvin instability describing the impact of a gas stream on the amplification of the instabilities of the liquid jet [4]. At increasing gas velocities the size of droplets decreases, due to the vorticities generated by the gas stream which influences the capillary waves on the jet surface leading to a reduction of the interaction length and consequently in the dimensions of th droplets.

The ratio between water droplets and jet diameters was also estimated in the framework of this thesis using a GDVN [8] with microtubes diameters from 10 μm - 50 μm, see Figure 2.5.

The linear correlation obtained between the jet diameter and the droplets diameter is visible in Figure 2.5 resulting in the relation of $d_{drop.} \approx 1.81 d_{jet}$. The experimental data obtained by us for the GDVN is in agreement with the literature calculated by Rayleigh using Rayleigh type nozzles (equation 2.16).

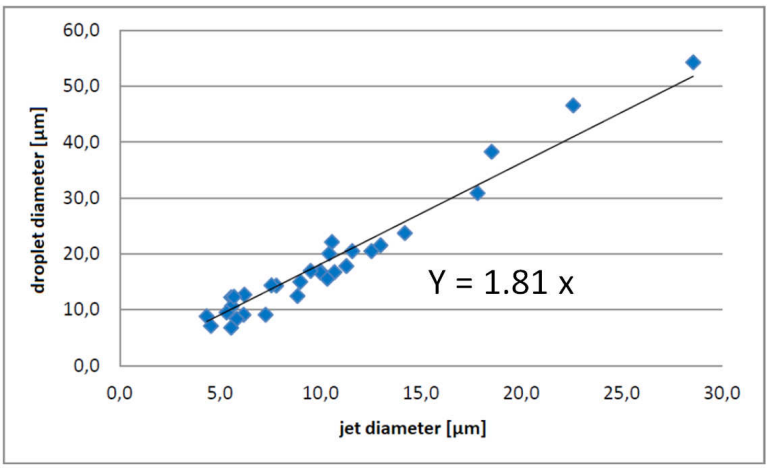

Figure 2.5: Study of water droplets diameter as a function of jet diameter using GDVN nozzles which microtube diameters vary from 10 μm to 50 μm [8].

2.3.2 Viscosity

The instability and disturbances of viscous liquids jets were investigated by Weber [52]. The main contribution of Weber's work to the understanding of the jet disintegration was on how viscosity affects the jet break-up. By adding viscosity parameter to the stationary jet, yields:

$$\lambda^2 + \lambda\frac{2\mu K^2}{I_0(KR)}\left[I_1'(KR) - \frac{K\tilde{K}I_1(KR)I_1'(\tilde{K}R)}{K^2+\tilde{K}^2I_1(\tilde{K}R)}\right] = \frac{\sigma R}{\rho\mu^2}\frac{KR(K^2-\tilde{K}^2)I_1(KR)}{(K^2+\tilde{K}^2)I_0(KR)}(1-K^2R^2), \tag{2.17}$$

with μ being the dynamic viscosity and $\tilde{k}^2 = k^2 + \lambda/\mu$.

By examining the equation we can conclude that higher viscosity jets lead to larger droplets delaying the break-up mechanism, as well as that the viscous effects increase the jet stability. In the limit of infinite viscosity, the jet will never break-up. The equation above is based on the assumption that the liquid is Newtonian, as the liquids studied in the framework of this thesis, where those viscosity is dependent on temperature, but independent of the applied shear rate [53].

The jet stability is a very important parameter for the feasibility of the work of this thesis, since the main focus is the study of a GDVN produced flow using the high-brightness hard-x-ray sources on microjets and microdroplets. For that it is fundamental to have directionally stable, microscopic, high speed liquid jet in vacuum. Therefore all these physical parameters, discussed in this chapter separately, have to be taken into account since the jet will be subject to them simultaneously, together with the nozzle parameters used to generate the jet (presented in 6.2.1 in nozzle preparation section).

Chapter 3

Fluids under external forces

Liquid jets produced by GDVN can be an alternative tool to study rheological properties of complex liquids at high shear rates. The flows produced by GDVN are known to created shear rates 3 or 4 times higher than with a normal rheometer, due to the mechanism of microjet collimation [15].

A study of the flow properties and the particles' behaviours dispersed in shear flows is of special importance because such flows are present in a wide range of systems, both in nature and industry.

This chapter presents the necessary theory [1] to understand the physical properties of the shear flows and the particles' behavior in such flows as well as the interactions between particles.

3.1 Rheological properties of fluids

Most simple fluids such as water, air and gases (with low molecular weight) are considered to be Newtonian. For such fluids the shear stress τ is linearly proportional to the shear-strain-rate $\dot{\gamma}$. The constant proportionality known as shear or coefficient of viscosity μ describing the Newton's law of viscosity's defined by:

$$\tau = \mu\dot{\gamma}. \tag{3.1}$$

On the other hand, many fluids of particular interest exhibit viscous and elastic responses when subject to deformations and are thus called Non-Newtonian fluids. These fluids can be defined as a material whose viscosity is dependent of forces like shear or elongation.

The shear flow is the movement of fluid layers such that they slide over each other, when a force F acts on a certain cross-sectional area of the fluid (Figure 3.1). The shear force F always acts in the parallel direction to the surface plane.

The shear stress is defined as the shear force acting per unit area and known by τ:

$$\tau = \frac{F}{A} \tag{3.2}$$

The velocity of the layers which slide over each other, increases proportionally relative to the bottom

[1] The basic concepts and equations described in this section were adapted from [54].

layer. The velocity gradient between the layers in the direction perpendicular to the flow, defines the shear rate $\dot{\gamma}$. If v is the velocity of the top layer and h the distance between the two extreme layers, then the shear rate is given by:

$$\dot{\gamma} = \frac{v}{h} \tag{3.3}$$

The resistance of the fluid to the forces in shear flow is defined as viscosity μ. As described above, for a Newtonian fluid the viscosity is given by Newton's law, as $\mu = \tau/\dot{\gamma}$, yielding

$$\mu = \frac{\text{shear stress}}{\text{shear strain rate}} = \frac{F/A}{v/h}. \tag{3.4}$$

Fluids are classified depending on the relationship between the shear stress and shear rate. A Newtonian fluid is a fluid in which the viscous stresses arises from its flow, at every point. Such fluids are linearly proportional to the local strain rate. Non-Newtonian fluids do not follow Newton's Law of viscosity. Most commonly, the viscosity of non-Newtonian fluids is dependent on shear rate or shear rate history. Included in the non-Newtonian fluids group there are some fluids in which it is possible to observe different behaviours even being characterized by a shear-independent viscosity. Furthermore, in a certain range of shear rates some fluids can present Newtonian behavior. Figure

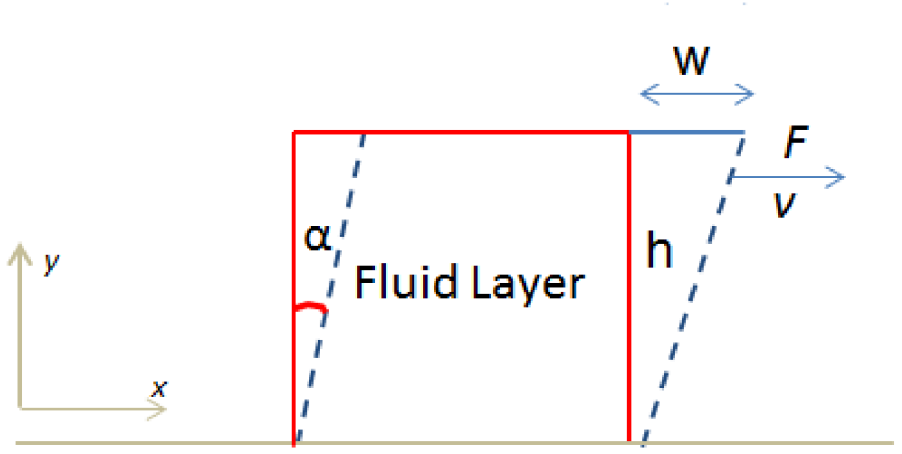

Figure 3.1: Illustration of a fluid deformation by a force F deforming the geometry by an angle α and a length w. h is the height between the two adjacent layers of the fluid with a velocity v.

3.2 shows the schematic differences between Newtonian and non-Newtonian fluids according to the shear stress and shear rate relationship. A non-Newtonian fluid shows a shear thinning regime when the viscosity decreases with increasing shear rate, and shows a shear thickening regime when the viscosity increases with increasing shear rate. An illustration of non-Newtonian fluids regimes is presented in Figure 3.3, for colloidal samples, according to the relation between viscosity and shear rate.

A shear thickening fluid is typically obtained by dispersing small particles within a liquid phase. Increasing the particles concentration beyond the dilute limit leads to particle-particle interaction,

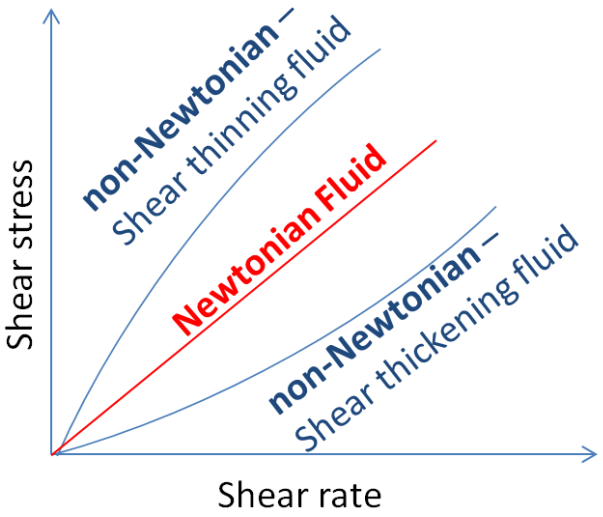

Figure 3.2: Illustration of the rheological behavior of the fluids, adapted from [9].

creating long-range order which results in non-Newtonian effects. These effect can be explained with a transition from an ordered to a disordered state [9].

When the fluids are subject to a relatively low shear rate, particles are able to form an ordered and layered structure, due to the repulsive interactions between particles, reducing in this way the viscosity of the solution [9]. At this point, if the shear rate increases above the critical point $\dot{\gamma}_c$, particle-particle interactions are overcome by the shear forces and the particles are squeezed together, resulting in a disordered and more complex structure. Therefore, shear thickening occurs when the repulsive forces are overcome by attractive hydrodynamic shear forces leading to the formation of hydroclusters, which increases the fluid viscosity [9].

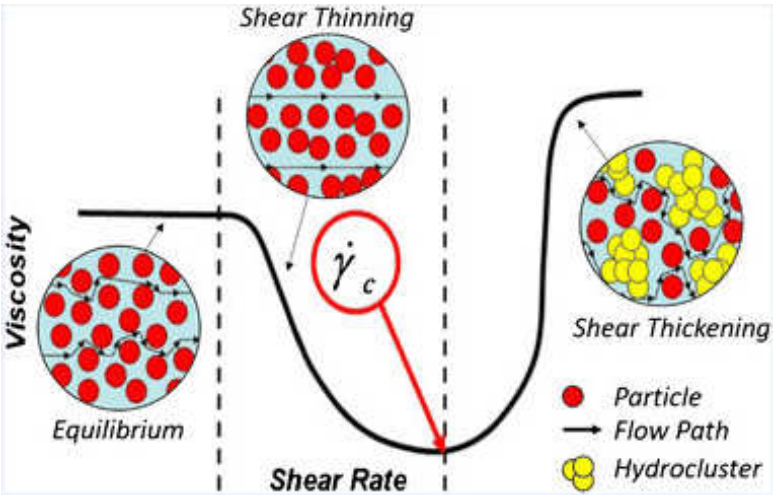

Figure 3.3: Schematics of shear thinning and shear thickening effect, from [9]

In the framework of this thesis one of the most common Newtonian fluids will be studied, water and its behavior in a microjet produced by a GDVN. Additionally, the behavior of spindle-shaped hematite dispersions in water will be analysed, in shear flows produced by GDVN. Such particles, are known to be sensitive to shear flows by aligning to a preferred direction. Therefore, in the following

section, a general overview of the behavior of nano-scale sized anisotropic particles in sheared flows will be presented.

3.2 Particles in shear flows

Understanding the behavior of particles in fluid flows and the rheological properties of suspensions on microscopic scales is fundamental not only from a theoretical point of view but also experimentally.

Although restricting the analysis to monodisperse and rigid spheres in viscous or laminar regimes, the flow of these suspensions shows peculiar rheological properties, such as particle deposits or agglomerates as a result of sedimentation inertia or diffusion [55, 56]. Early work in the field was performed by Einstein in 1906, who derived an expression to calculate the effective viscosity of suspension of monodisperse spheres, assuming very low volume fraction ($\phi < 0,1\%$) (neglecting the hydrodynamic interactions between particles). This expression is know as Einstein viscosity and is given by [57]:

$$\mu_e = \mu(1 + \frac{5}{2}\phi), \tag{3.5}$$

where the normalized viscosity μ_e / μ grows linearly with the volume fraction ϕ.

A correction to this equation was introduced by Batchelor in 1972 [58] assuming higher volume fractions. However, for system with the maximum packing limit, the effective viscosity μ_e of the suspension diverges. μ_e and and ϕ were described by Krieger and Dougherty [59] as:

$$\mu_e = \mu(1 + \frac{\phi}{\phi_m})^{[\mu]\phi_m} \tag{3.6}$$

where μ is the viscosity of the sample and ϕ_m the maximum packing fraction. The effective viscosity can be related to the shear rate by using the Buckingham theorem, assuming neutrally buoyant systems at steady-state, as a function of Reynold's number and Péclet number as: $\mu_e/\mu = f(\phi, Re_{\dot{\gamma}}, Pe_{\dot{\gamma}})$ [55].

Following the Stokes-Einstein-Sutherland fluctuation-dissipation relationship it is possible to describe the particles diffusion in a dispersed phase through the continuous phase, by [9, 60]:

$$D = \eta k_B T = \frac{k_B T}{6\pi\mu a}, \tag{3.7}$$

where η is the mobility of the continuous phase, expressed by Stokes' law: $\eta = 1/\zeta = 1/(6\pi\eta a)$ [9]. However, equation 3.7 is only valid for spheres. In the case of anisotropic particles, such as spindles, equation 3.7 has to be modified taking into account the particles aspect ratio (see Chapter 7).

From the expression above, it is possible to estimate the time required for a particle to diffuse a distance equal to its hydrodynamic radius as $\tau = a^2/D$.

A large number of studies have focused on the case of spherical particles however in our daily life the majority of the particles are anisotropic, e.g., micro-organisms in flow [61], dynamics of ice

crystals in clouds [62], and fibers process in paper industry [63].

Samples with different shape, concentrations and aspect ratios, lead to different effects under shear. At high concentrations, particle-particle interactions dominate the dispersions, while at small concentrations particle-fluid interactions, and the particle-wall interactions play an important role in rheological response. In the next section, the behavior of anisotropic particles in flow with concentration < 1 vol.$\%$ will be discussed.

3.2.1 Elongated particles in flow

Anisotropic particles are present in our daily life, in biological, industrial and environment process. Elongated particles, such as the spindles studied in this thesis, have interesting behaviours in flow. Among those, these suspensions present peculiar properties such as agglomeration or different orientations depending on the flow regimes and the particles volume fractions.

There are many ways to study the effect of fluid flows on elongated particles, both of nano-scale size. For instance, the observation of the anisotropic particles orientation distributions in a defined flow provides insight in to the dynamics of the system and the interaction between particles and fluid as well as the interaction between particles.

Ellipsoidal particles in shear flow were studied for the first time by Jeffery [64] and Taylor [65] in 1922. When ellipsoidal particles are small compared to the smallest length scales in the flow, their rotation rate is determined by the velocity gradient tensor, known as Jeffery's equation [64]:

$$\dot{p}_i = \Omega_{ij} p_j + \frac{\alpha^2 - 1}{\alpha^2 + 1}(S_{ij} p_j - p_i p_k S_{kl} p_l), \tag{3.8}$$

where p_i is a component of the orientation director and α is the particles aspect ratio of the ellipsoid, Ω is the vorticity and S the strain rate.

If the particles are very small, they tend to move with the same local fluid velocity than the fluid. For particles whose density is different from the surrounding fluid and with large aspect ratios one observes preferred aligned directions [66]. The behaviour of small rods, for example, presenting different aspect ratios was studied in shear flow; the authors concluded that the aspect ratio of this elongated particles plays the main role on the rods behavior in shear flow [67].

The dynamics of an anisotropic particle in a high shear flow offers a rich variety of behaviours, such as diffusion, rotation and particle vibrations. The alignment of such particles under high shear rates is faster leading to a small particles rotation period, T_{rot}, while, for small shear rates, particles rotate slowly, which can be calculated by [64]:

$$T_{rot} = \frac{2\pi}{\dot{\gamma}} \left(\nu + \frac{1}{\nu} \right), \tag{3.9}$$

where ν is the particle aspect ratio.

In shear flow the concentration plays an important role. For low concentrations, the interactions between particles can be neglected and there are only fluid-particle interactions [68].

Kerekes $et\ al$ quantify the number of mechanical interactions in a suspension containing elongated particles [68]:

$$N = \frac{2}{3} C_V \left(\frac{l}{d}\right)^2, \tag{3.10}$$

where d is the particle diameter and l the particle length and C_v is the volume fraction. N assumes a sphere volume that encloses the particle over all angles to the total available volume. Thus, N represents the degree of overlapping between the spheres, hence, the number of interactions between the particles when allowed to rotate freely. N can vary $1 < N < 60$ from the dilute to concentrated regimes. In between, the system is known as semi-dilute.

In the semi-dilute regime mechanical particle-particle interactions become important, contrary to the concentration regime where a network is formed due to the restricted movements of particles. Different authors studied these semi-dilute regime, due to is complexity, because different sizes and particles shapes cause different particle behavior and consequently different particle alignments in the flow [69, 70]. In a semi-dilute and in a concentrated regime the hydrodynamic interactions of elongated particles plays an important role leading to a preferred orientation in flow, while the Brownian motion randomizes the particle orientation [46].

Particle migration is an important feature observed in wall-bounded flows. Particle migration leads to an increase of the particle volume fraction, depending on the particle shape and flow rate [71]. Different types of migrations can be observed as well, depending on the particle Reynolds number, $\mathrm{Re}_{\dot{\gamma}}$. Small particles tends to flow towards the walls as a result of diffusion, this particle deposition depends on their relaxation time τ_P. Small sized particles, with low viscosity and in contact with low shear rates tend to a randomized orientation by the Brownian motion.

For large aspect ratios, viscosities or shear rates, elongated particles align to a preferable direction. However elongated particles in shear flow do not align always in the same direction; thus an orientation distribution function (ODF) has to be taken into account as a function of polar and azimuthal angles. This will be discussed in more detail in chapter 7.

The behaviour of spindle-shaped hematite particles under shear for different aspect ratios was investigated for the first time by Gunes $et\ al$ using rheo-optical methods and flow microscopy [72]. For $Pe > 70$ they reported a particle alignment parallel to the flow direction, while for $Pe < 50$ particles are orientated perpendicular to flow direction, the transition in between these two regions is characterized by multiple particle orientations.

Several groups have studied orientation dynamics in flows with uniform velocity gradients, where the effects of inertia and aspect ratio have been investigated [72**?** –75]. In complex flows the rotational diffusion and the orientation distributions have been measured as well [76, 77].

In the framework of this thesis the orientational behavior of spindle hematite particles under shear flows will be studied as a function of particles' volume fraction and aspect ratio. This short overview on elongated particles under shear aims to give insight into the characterization of the laminar flow itself and spindle-shaped particle behaviour in such fluids.

Chapter 4

X-ray scattering theory

X-ray radiation has been discovered by W. C. Röntgen in 1895 belonging to the electromagnetic spectrum with wavelengths in the range from 0.1 to 100 Å.

X-rays photons of high energies enable the penetration of opaque materials. Its wavelength allows atomic resolution which makes the X-ray scattering technique suitable for vast scientific, medical and industrial applications. The possibility to reveal the structure of matter down to the atomic scales makes X-ray scattering very useful and well suited to investigate soft matter materials.

This chapter introduces various aspects of X-ray scattering theory necessary to analyse and interpret the small and wide angle X-ray scattering experiments (SAXS and WAXS) presented in this thesis. The equations and concepts necessary to understand the structure of the samples in this study are adapted from [11, 78, 79].

4.1 Elastic scattering

When electromagnetic radiation, in particular X-rays, interacts with matter, several processes can occur depending on the energy of the incident wave: (1) Elastic or coherent scattering (Rayleigh); (2) Inelastic or Compton scattering; (3) Photoelectric effect and (4) Pair production.

In the following, only the elastic scattering, where the energy of the scattered light does not change, will be discussed.

Elastic scattering results from the interaction between a electromagnetic wave with the electrons of the material. The electric field $E(\mathbf{r}, t)$ defined by the wave vector $\mathbf{k}$, is given by:

$$E(\mathbf{r}, t) = E_{\mathrm{rad}} e^{i(\mathbf{k}\cdot\mathbf{r}-\omega t)}, \tag{4.1}$$

where E_{rad} is the amplitude of the electric field. The term ωt gives the temporal dependence, with ω the frequency of the incoming wave, and the term $\mathbf{k} \cdot \mathbf{r}$ represents the spatial dependence of the wave. Note that the wave vector $\mathbf{k}$ is inversely proportional to the wavelength λ of the incoming wave with the modules $|\mathbf{k}| = \mathrm{k} = 2\pi / \lambda$. For a typical scattering experiment (see Figure 4.1) the incoming beam, $\mathbf{k}_{\mathrm{i}}$, and the outgoing beam $\mathbf{k}_{\mathrm{o}}$ can be defined.

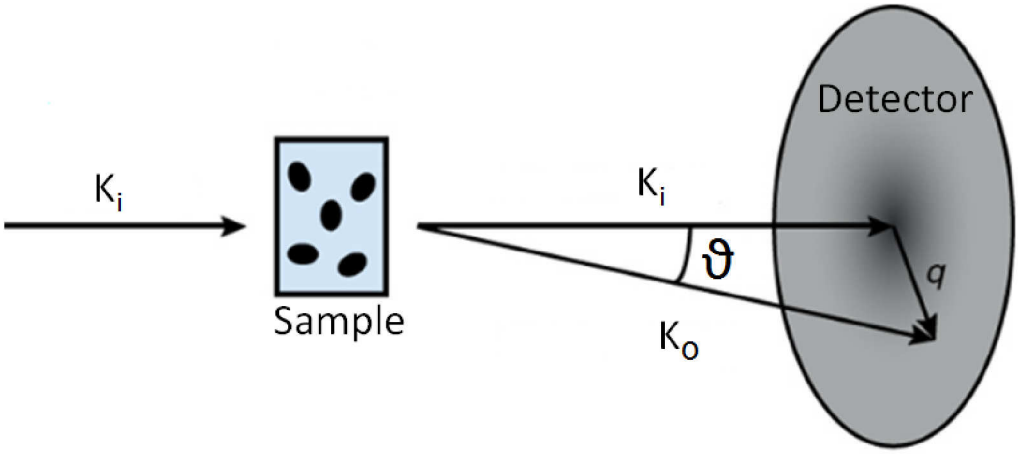

Figure 4.1: Representation of a scattering experiment. The incident X-ray beam with wave vector k_i is scattered by the sample by the outgoing beam k_o. The scattering angle between k_i and k_o is denoted as ϑ.

Considering the scattered radiation observed at the angle ϑ from the incident wave, it can be described by the wave vector transfer $\mathbf{q}$ given by: $\mathbf{q} = \mathbf{k}_o - \mathbf{k}_i$. Thus the modulus of the wave vector transfer q, is given by:

$$|\mathbf{q}| = \mathbf{q} = |\mathbf{k}_o - \mathbf{k}_i|. \tag{4.2}$$

Since in an elastic scattering process $|\mathbf{k}_i| = |\mathbf{k}_o|$, the wave vector transfer can be calculated depending on the scattering geometry:

$$|q^2| = |k_i - k_o|^2 = {k_i}^2 + {k_o}^2 - 2k_i k_o = 2k_i^2 - 2k_o^2\cos(\vartheta/2) = 4k_i^2\sin^2(\vartheta/2), \tag{4.3}$$

$$q = \frac{4\pi}{\lambda}\sin\left(\frac{\vartheta}{2}\right). \tag{4.4}$$

4.2 Scattering intensity

In this section the total scattering intensity by an electron and by complex systems will be presented guided by [11, 79].

Assuming elastic scattering, the total scattered intensity (or amplitude) is defined as the sum of all scattered intensities (or amplitudes) an is given by: $I(\mathbf{q}) = |A(\mathbf{q})|^2$.

4.2.1 Scattering from a single electron

Consider the most elementary scattering process of X-rays on a single free electron. When a plane and polarized electromagnetic wave hits the electron, the electron vibration starts in the direction of the incident electric field. Afterwards a force -e$\mathbf{E}$ is created leading to an acceleration e$\mathbf{E}$ / m_e where m_e is the electron mass.

The electron acceleration leads to a scattered field, which can be calculated in terms of the scattered intensity as: $I_{\mathrm{rad}} = E^2_{\mathrm{rad}}$, being the result:

$$I_{rad}(R,t) = \left(\frac{e^2}{4\pi\varepsilon_0 mc^2}\right)^2 \frac{I_{in}}{R^2}\cos^2\psi = r_e^2\frac{I_{in}}{R^2}\cos^2\psi, \tag{4.5}$$

$\mathrm{r_e}$ is the well known Thomson scattering length or by the electron radius $\mathrm{r_e} = 2.8179 \times 10^{-6}$ nm. The intensity of the scattered spherical wave depends on the distance R to the scattering centre and the polarization direction ($\cos\psi$).

In the case of a synchrotron source polarized in the horizontal plane, it follows that:

Polarization = 1 for intensity scattered in the vertical plane.

Polarization = $\cos^2\psi$ for intensity scattered in the horizontal plane.

The polarization factor is important as a correction to the scattered intensity. For small angles this correction can be omitted since $\cos^2\psi \approx 1$. However, the scattering correction at larger angles has to be applied, as described in the data analysis of chapter 7.

4.2.2 Scattering from complex systems

Considering now the scattering intensity by complex systems (composed by two or more electrons) in a scattering experiment. The scattering intensity $I(\mathbf{q})$ is defined as the number of scattered x-ray photons per unit-time and unit-area and is given by:

$$I(\mathbf{q}) = I_0\frac{\mathrm{d}\sigma}{\mathrm{d}\Omega}(\mathbf{q})\mathrm{d}\Omega, \tag{4.6}$$

where I_0 is the intensity of the incident beam. $\mathrm{d}\sigma/\mathrm{d}\Omega$ is the differential scattering cross section and $\Delta\Omega$ a solid angle at the detector.

The differential cross section $\mathrm{d}\sigma$ / $\mathrm{d}\Omega$ is given by:

$$\frac{\mathrm{d}\sigma}{\mathrm{d}\Omega} = \frac{\text{N. of X-ray photons scattered per second into } \Delta\Omega}{NI_0\Delta\Omega}, \tag{4.7}$$

where N is the number of particles per unit area, I_0 is the number of incident x-ray photons per unit cross section of the incident beam.

Scattering from one atom

When considering all electrons in the atom, or in a large scale, all electrons from one sample, they can not be regarded as free electrons. Thus the atomic form factor $F^{\mathrm{atom}}(\mathbf{q})$ for an atom can be obtained by re-writing the equation above integrating over its electron density:

$$F^{\mathrm{atom}}(\mathbf{q}) = \int \rho(r)e^{(i\mathbf{q}\cdot\mathbf{r})}d\mathbf{r}. \tag{4.8}$$

Scattering from molecules

For a single particle, the molecular form factor, $F^{\mathrm{mol}}(\mathbf{q})$ is the sum of the atomic form factors:

$$F^{\mathrm{mol}}(\mathbf{q}) = \sum_{\mathbf{r}j}^{\mathrm{mol}} F_j^{\mathrm{atom}}(\mathbf{q}) e^{(i\mathbf{q}\cdot\mathbf{r}_j).} \tag{4.9}$$

where F_j are the form factors of the j atoms and $\mathbf{r}_j$ their respective positions in the molecule.

4.3 Form factor

The form factor refers to the Fourier transform of the electron density $\rho(r)$ which can be generalized by the equation 4.8 integrating over the particle volume. The form factor can be calculated taking into account the far-field approximation, when the sample-detector distance is assumed to be larger than the sample size, as well as in the first Born approximation, neglecting multiple scattering events, by:

$$F(\mathbf{q}) = \int_V \rho(r) e^{(i\mathbf{q}\cdot\mathbf{r})} d\mathbf{r}, \tag{4.10}$$

where $\rho(\mathbf{r})$ is the electron density distribution at the position $\mathbf{r}$, and V denotes the integration over the all space.

Since the form factor represents the scattering of the particle shape and morphology at small $\mathbf{q}$ values, a specific model to describe the spindle-shaped particles behavior in the flow will be presented in the next section.

4.3.1 Form factor - spindle-shaped particles

A model form factor to describe single spindle-shaped particles was presented by Märkert $et\ al$ [80]. The expressions and deductions presented in this section are based on [15, 80].

A form factor from a spindle shape particle describes a body of revolution resulting from two intersecting circles with radius R (Figure 4.2). The spindle geometry is composed by a minor semi-axis R_1 and a major semi-axis L which are parallel to the x and z-axis of the particle, respectively. Since $L > R_1$ the resulting form factor is anisotropic, and for a single spindle shape can be deduced by:

$$P_{single}(q, \vartheta_q, R_1, R_2, \nu) = \left(\frac{4\pi}{V(R_1, \nu)} \int_0^{L/2} \cos(qz\cos(\vartheta_q)) \frac{R_1 - R_2 + (R_2^2 - z^2)^{1/2}}{q\sin(\vartheta_q)} \right.$$
$$\left. \cdot J_1 q\sin(\vartheta_q)[R_1 - R_2 + (R_2^2 - z^2)^{1/2}]dz \right)^2, \tag{4.11}$$

where J_1 is Bessel function of first kind, d_z is the differential increment of particle length, L. The

radius is given by R = (L^2 + R_1^2 / 4 R_1). ν is the particle aspect radius defined by ν = L / R_1. Thus, the volume of a spindle particle can be calculated to:

$$V_{single}(R_1,\nu) = \frac{2\pi}{3}\left\{\frac{(2R_1)^3}{8}\nu\left[\frac{3}{4}(1+\nu^2)-\nu^2\right]\right\} + \frac{2\pi}{3}\left\{\frac{3(2R_1)^3}{32}(1+\nu^2)^2\left[1-\frac{1}{2}(1+\nu^2)\right]\arcsin(\frac{2\nu}{1+\nu^2}\right\}. \quad (4.12)$$

The real particle system underlies a natural distribution of particle sizes, quantified by the size polydispersity. A Schulz-Flory distribution can be used to model the size distribution of particle's minor semi-axis [10, 15]. Thus, the form factor of a polydisperse spindle-shape particles system can be derived by:

$$P_{poly}(q,\vartheta_q,R_1,R_2,\nu,Z) = \frac{1}{\langle V^2\rangle}\int_0^\infty c\,(R,R_1,Z)V^2(R,\nu)\cdot P_{single}(q,\vartheta_q,R,R_2,\nu)\,dR, \quad (4.13)$$

where $c(R,R_1,Z)$ represents the particles size distribution with particle radius R particle semi-minor axis R_1 and Z is related to the polydispersity by:

$$p = \frac{\Delta R}{R_0} = \sqrt{\frac{1}{Z+1}}, \quad (4.14)$$

being R_0 the particle mean radius.

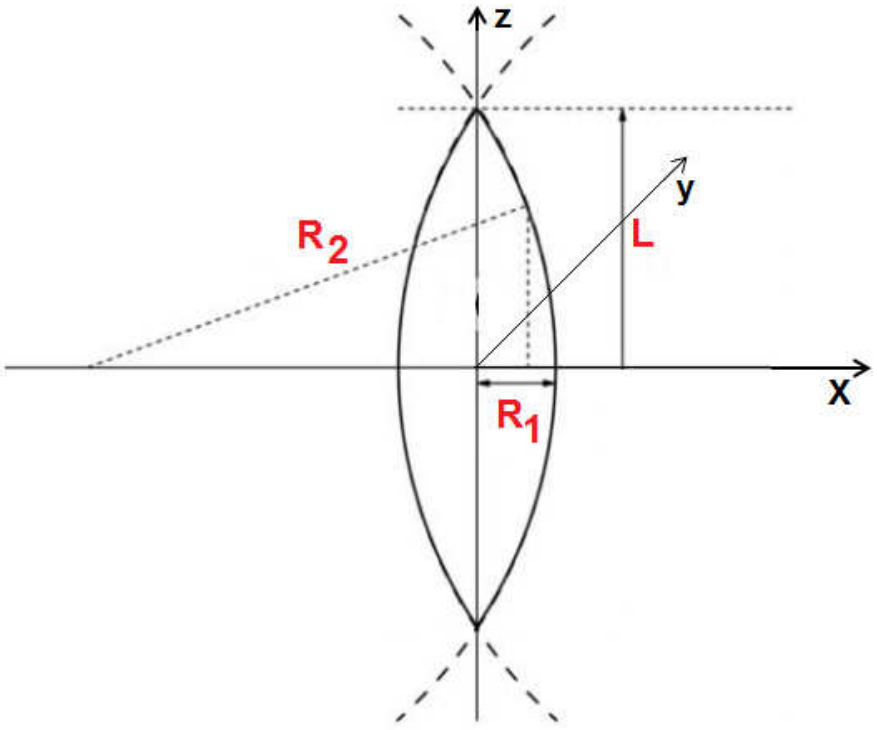

Figure 4.2: Sketch of the geometry of the spindle-shaped particles as a body revolution resulting from two intersecting circles, adapted from ref. [10].

4.4 Structure factor

Let's distinguish now the structure factor for random oriented systems (liquids) and oriented systems, crystals:

4.4.1 Randomly oriented systems

Considering now concentrated systems composed by N particles randomly oriented, the scattering for such systems can be written as:

$$F(\mathbf{q}) = \sum_{\mathbf{r_j}}^{\mathrm{N}} F_j^{single}(\mathbf{q}) e^{(i\mathbf{q}\cdot\mathbf{r}_j)\cdot} \tag{4.15}$$

Supposing that such particles are formed by N identical scatters, the scattering intensity is given by $I(q) = F^2(q)$, or:

$$\begin{aligned} I(q) &= \sum_{j}^{\mathrm{N}} \sum_{k}^{\mathrm{N}} F_j^{single} F_k^{*single} e^{(i\mathbf{q}(\mathbf{r}_j - \mathbf{r}_k)} \\ &= N \cdot |F^{single}|^2 + |F^{single}|^2 \sum_{j\neq k} \sum_{k} e^{(i\mathbf{q}(\mathbf{r}_j - \mathbf{r}_k)} \\ &= N \cdot |F^{single}|^2 (1 + \frac{1}{N} \sum_{j\neq k} \sum_{k} e^{(i\mathbf{q}(\mathbf{r}_j - \mathbf{r}_k))}). \end{aligned} \tag{4.16}$$

being the term last term of the equation $= S(\mathbf{q})$.

$S(\mathbf{q})$ takes the interparticle interactions into account and is called structure factor:

$$S(\mathbf{q}) = 1 + \frac{1}{N} \sum_{j\neq k} \sum_{k} e^{(i\mathbf{q}(\mathbf{r}_j - \mathbf{r}_k))\cdot} \tag{4.17}$$

4.4.2 Structure factor of crystals

A crystal can be considered as a repetitive system (lattice) composed by symmetry elements. For an infinite lattice with point-like scatterers which are organized into a crystal a lattice vector $\mathbf{R}_\mathrm{n}$ can be defined:

$$\mathbf{R}_n = n_1\mathbf{a}_1 + n_2\mathbf{a}_2 + n_3\mathbf{a}_3, \tag{4.18}$$

where $\mathbf{a}_1$, $\mathbf{a}_2$ and $\mathbf{a}_3$ are the basis vectors for the lattice containing the definition of the unit cell [1] and n_1 n_2 and n_3 are integers. The scattering amplitude from a crystalline material comprised of atoms

[1] Unit cell is the repeated structural entity of a crystal.

can be factorized into the product of the form factors of a unit cell and the lattice, as given by equation 4.19 [11, 78].

The first summation is the unit cell structure factor, equivalent of the form factor for isolated particles. The sum is taken over the form factors of the atoms or molecules in the unit cell with their respective phase factors. The second term is the lattice sum or, alternatively, the structure factor or interference function $S(\mathbf{q})$.

$$F^{\text{crystal}}(\mathbf{q}) = \sum_{j}^{\text{unit cell}} F_j^{\text{atom}}(\mathbf{q}) e^{(i\mathbf{q}\cdot\mathbf{r}_j)} \sum_n e^{(i\mathbf{q}\cdot\mathbf{R}_n)} = F^{\text{unit cell}}(\mathbf{q}) \sum_n e^{(i\mathbf{q}\cdot\mathbf{R}_n).} \tag{4.19}$$

Here $\mathbf{R}_n$ is the vector that defines the origin of the cell in the lattice and $\mathbf{r}_j$ the atoms in the unit cell, thus the position of the atoms in the sample can be described by $\mathbf{R}_n$ +$\mathbf{r}_j$.

Hence, using the S($\mathbf{q}$) definition given above, it can be described as:

$$F^{crystal}(\mathbf{q}) = F^{unit\ cell}(\mathbf{q}) S(\mathbf{q}) \tag{4.20}$$

The amplitude of the scattered wave is negligible unless the scattering vector fulfils the condition:

$$\mathbf{q} \cdot \mathbf{R}_n = 2\pi \times integer. \tag{4.21}$$

Therefore, $\mathbf{q}$ has to correspond to a so-called reciprocal lattice vector, defined as:

$$\mathbf{G} = h\mathbf{a}_1 + k\mathbf{a}_2 + l\mathbf{a}_3, \tag{4.22}$$

where h, k and l are integers, and known as Miller indices. A crystalline diffraction is only observed when $\mathbf{G}_{hkl}$ = $\mathbf{q}$, following the Laue condition. The distances d between lattice planes in reciprocal space are related to those in real space by

$$d = \frac{2\pi}{|q|}. \tag{4.23}$$

This is equivalent to the well-known Bragg diffraction condition, which is usually expressed as a function of real-space distance of lattice planes d, the Bragg angle ϑ from which radiation is scattered, the wavelength of the incident radiation λ and the diffraction order n, that describes the maximum interference:

$$n\lambda = 2d\sin(\vartheta). \tag{4.24}$$

The diffraction of a polycrystalline powder[2] is characterized by continuous diffraction rings (Debye - Scherrer rings) if the particle crystallites are randomly orientated. Each ring corresponds to a particular vector $\mathbf{G}$ see Figure 4.3 a). After a circular averaging a linear plot of the diffracted intensity,

[2]Polycrystalline powder consists of many of tiny crystallites with randomly distributed orientations.

I as a function of ϑ, can be obtained (Figure 4.3 b)).

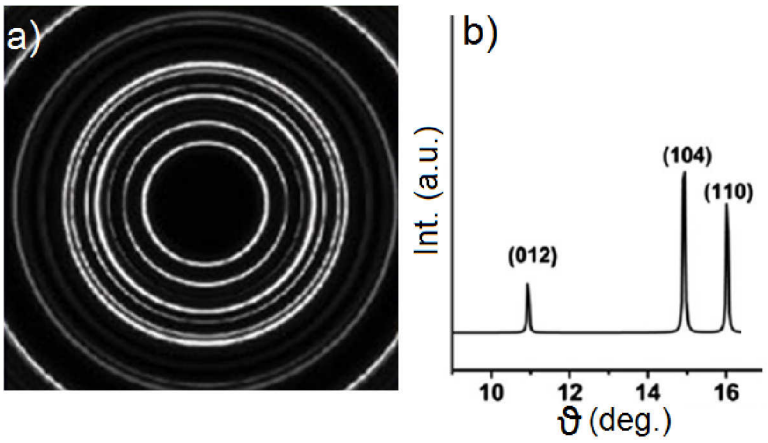

Figure 4.3: Example of a powder diffraction pattern from a randomly oriented sample. a) Scattering pattern. b) Diffractogram after a circular averaging. Figure adapted from [11].

An exemplary diffractogram provides information on the crystalline structure of the sample. If allows to understand the size and the symmetry of the unit cell. The structure factors of the crystal can be obtained extracting the measured intensities, and the structural model can be recalculated using the entire diffraction profile via a so-called Rietveld analysis.

Single crystals and larger isolated crystals are identified in scattering patterns showing isolated spots. However, if the system is composed by an alignment of crystalline structures can be characterised by discontinuous Debye - Scherrer rings, as presented in Figure 4.4, indicating an high degree of orientation in the system. Several diffraction patterns will be analyzed in the framework of this thesis. The scattering patterns under analysis present continuous and discontinuous Debye Scherrer rings providing structural information on the crystal orientation. A detailed analysis to hematite crystalline structure is presented in chapters 5 and 7.

4.5 Small and wide angle scattering

Although the base equations for the scattering intensity calculations are equivalents for atoms, molecules and nano-particles, the measured scattering for these systems differs in the characteristic structural sample size d or wave vector, q.

In practice, elastic X-ray scattering is divided into two regimes by the magnitude of the scattering angle, small and wide angle X-rays regimes (SAXS and WAXS), respectively. The domain of the X-ray scattering intensity holds a law of reciprocity between the scattering vector $|\mathbf{q}|$ and the characteristic length, L, of the scale within objects are being studied, such that $L \sim 1/q$ [79]. Thus, by varying the interval of q, one can study an object in different length scales.

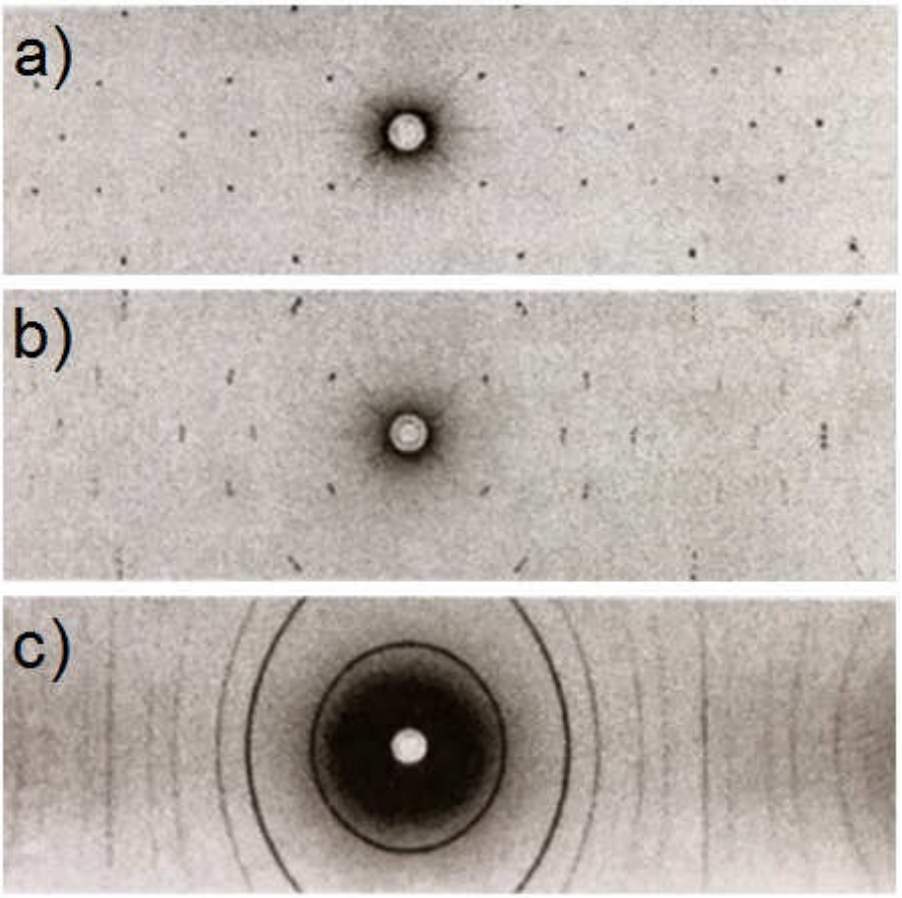

Figure 4.4: Illustration of diffraction patterns of samples with different degrees of orientations. a) Single crystal, b) crystals with an intermediated degree of alignment and c) randomly orientated crystals. Figure adapted from [11].

SAXS is employed when the system contains larger correlation distances from nano to micrometer regimes. With this technique the particles' structure is probed to measure the scattering intensities at angles below few degrees.

WAXS is used for short correlation distances regions, therefore, is a useful technique for solving the atomic positions in crystal lattices, whereas in SAXS the scattering originates from larger scale inhomogeneities in the electron density. Commonly WAXS region deals with scattering angles exceeding 10 ° and atomistic scales [79].

In the framework of this work SAXS and WAXS experiments were performed. The SAXS technique was used for studying different anisotropic scattering patterns collected at different microjet regions, whereas WAXS was used to reveal the orientation of spindle-shaped particles along shear flows by the analysis of the azimuthal width of the incomplete Debye - Scherrer rings.

Chapter 5

Sample preparation and characterization

Nanometer-sized iron oxide particles have emerged as versatile materials for different applications due to their magnetic, electronic, photonic and optical properties. Iron oxides, especially hematite, have been used since ancient times as pigments, for example to give reddish coloration to pottery. Hematite is abundant in nature [81], has low toxicity [82] and is soluble in water [83].

In this thesis, spindle-shaped hematite particles have been used to study the behavior of particles in shear flows. The synthesis of spindle-shaped hematite results in monodisperse, single-crystalline particles with a tunable aspect ratio [84]. This anisotropic sample system can be used to characterize flows, since it is known to be sensitive to shear forces via aligning to a preferred direction [12, 14, 80].

This chapter describes the synthesis and characterization of spindle-shaped hematite particles used as a microrheological probe to investigate their behavior in a microjet produced by GDVN.

5.1 Sample description

Iron (III) oxide is a versatile material with a wide range of applications in industry, medicine, biology, and environment, basically because of its polymorphic nature. Iron (III) oxide has four polymorphs, and only two of them had been found in nature as minerals, namely hematite (α-Fe_2O_3) and maghemite (γ-Fe_2O_3) while the other two (β-Fe_2O_3, ε-Fe_2O_3) can be found only as synthetic nanoparticles.

Iron oxide samples have important magnetic properties, such as spontaneous magnetization or magnetic anisotropy which are influenced by the size of the material. When iron and iron oxide particles have nanometric sizes ($<$ 100 nm) they exhibit magnetic behavior induced by surface and finite-size effects. In particular, hematite [85], maghemite [86], magnetite [86], and iron [87] show superparamagnetism, that is only present in monodomain particles below a critical size. When the nanoparticles are too small, they have only one magnetic domain and their spins thermally fluctuate inside of the nanoparticles following several orientations corresponding to the minima of the anisotropy energy. The most important characteristic of the superparamagnetic nanoparticles is a zero coercivity. It means that after the application of an external magnetic field the particles return to their fluctuant state without any remaining magnetization [7,10].

Hematite with spindle-like shape was the polymorph chosen to be investigated in the framework of this thesis since it is a well proven sample system, easy to synthesize and the most stable polymorph, therefore the most used in industrial applications.

A great interest has been devoted towards to the synthesis of hematite because it is possible to vary physical properties by the modification of particle shape and size. Hematite nanoparticles can be prepared by several techniques such as the hydrothermal approach, catalytic synthesis, flame spray pyrolysis and non-aqueous synthesis [88–90]. In this work the spindle-shaped hematite particles were prepared by forced hydrolyses of iron solutions, in a dilute homogeneous solution of ferric chloride in the presence of phosphate ions, as presented in section 5.2.

Hematite crystallizes in space group $R\bar{3}c$ with lattice parameters a = 5.04 Å and c = 13.75 Å, belonging to the trigonal-scalenohedral crystal class [12]. In the hematite structure, Fe^{3+} ions occupy two-thirds of the octahedral sites. The sharing of three edges and one face between FeO_6 octahedron is responsible for the distortion of the cation sub-lattice from the ideal packing [12, 91].

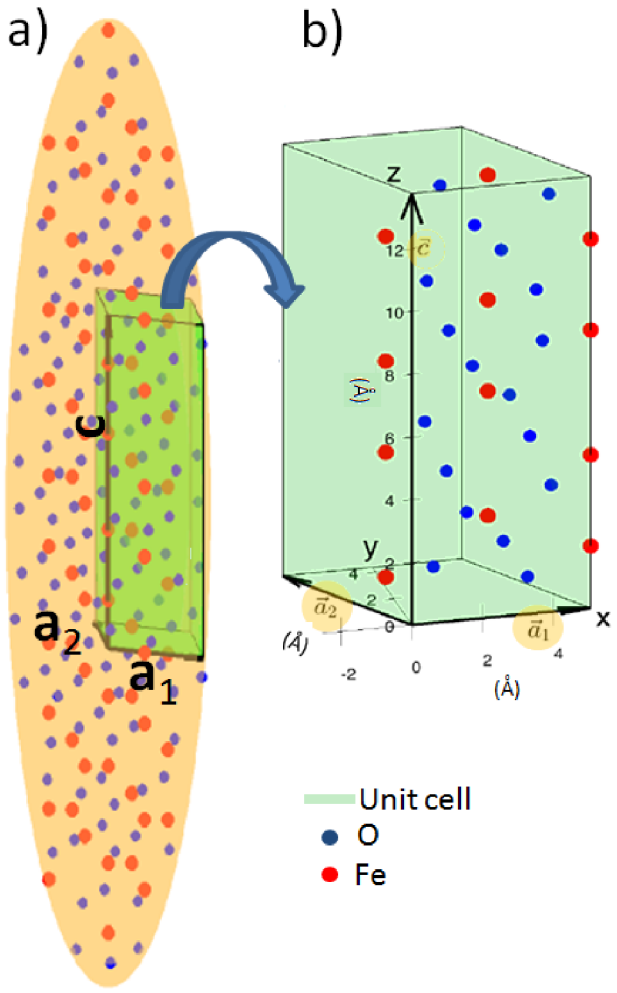

Figure 5.1: Schematic representation of the crystal structure a) of a spindle-shaped hematite with an hexagonal unit cell, being $\mathbf{a_1}$ and $\mathbf{a_2}$ = 5.04 Å and $\mathbf{c}$ = 13.75 Å. b) Hexagonal unit cell of hematite where the angle between $\mathbf{a_1}$ and $\mathbf{a_2}$ is 120 ° and the coordinates for the basis are defined as $\mathbf{a_1} = \{5.04\ 0\ 0\}$, $\mathbf{a_2} = \{-2.516\ 5.04\ 0\}$ and $\mathbf{c} = \{0\ 0\ 13.772\}$. The hematite crystallographic dataset with a space group of $R\bar{3}c$ was taken from the "American Mineralogist Crystal Structure Database", based on [12].

The hematite crystal structure is presented in Figure 5.1 where the oxygen atoms, blue dots, form octahedrons containing one iron atom each (red dots). The unit vectors $\mathbf{a}$ and $\mathbf{c}$ are parallel to the the x-axis and z-axis correspondingly. The angle between $\mathbf{a_1}$ and $\mathbf{a_2}$ is 120° while others are 90° and the coordinates from the atoms are defined as $\mathbf{a_1} = \{5.04\ 0\ 0\}$, $\mathbf{a_2} = \{-2.516\ 5.04\ 0\}$ and $\mathbf{c} = \{0\ 0\ 13.772\}$.

The magnetic state of the hematite changes with temperature, at the Morin temperature (T_{M}) and the Néel temperature (T_{N}). The magnetic transition temperatures for bulk hematite have values of $T_{\mathrm{M}} \approx 260$ K and $T_{\mathrm{N}} \approx 950$ K [92]. The Morin temperature varies with the particles size, and decreases when the particle size is below 100 nm [93]. Therefore, at high temperatures different magnetic phases are known [92]

5.2 Sample preparation

In the framework of this project, spindle-shaped hematite particles were prepared by forced hydrolysis of iron salt solutions at elevated temperatures based on the procedure of Ozaki *et al.* [94] procedure, following the chemical reaction:

$$2\,\mathrm{FeCl_3} + 3\,\mathrm{H_2O} \xrightarrow[\Delta]{\mathrm{NaH_2PO_4}} \mathrm{Fe_2O_3} + 6\,\mathrm{HCl}. \tag{5.1}$$

Aqueous solutions containing 0.020 mol/L of iron (III) cloride, $FeCl_3$ ($m(\mathrm{FeCl_3}) = 5.40$ g) and variable concentrations of sodium dihydrogen phosphate (NaH_2PO_4) were heated to the boiling point (125 °C) and kept under reflux for 48 hours. Variable concentrations of NaH_2PO_4 were used to get different particles aspect ratios (ν), varying typically from ν = 2 to ν=10. The ratio $m(\mathrm{NaH_2PO_4})$ / $m(\mathrm{FeCl_3})$ determines the aspect ratio of the resulting hematite spindles due to the adsorption selectivity of H_2PO_4, details on particle's grow will be presented in the next paragraphs.

In the course of the reaction process the turbidity increases constantly until the suspension reaches its final color (dark orange). After the growth, particles were precipitated by centrifuging at 500 rpm and the precipitate is washed three times with deionized water in order to eliminate stray ions. Subsequently, the particles are redispersed in ultra pure water for further characterization. The stability of such particles in water is acquired by the adsorption of chloride (Cl^-) anions from the solution as well as due to the negative charges carried by the iron oxide surfaces for neutral to weakly acid pH levels [91, 95].

Using this technique highly crystalline spindle-shaped nanoparticles are obtained. Further advantages of the technique are its simplicity, relatively narrow size distribution, shape control of nanoparticles, and medium yield.

The reaction time, temperature, and concentration have important effects on the size and shape of reaction products, allowing an hematite production with different sizes and shapes (rods, nanowires, nanotubes, spindles and needles [96].

An overview of hematite spindles prepared in this work is summarized in Table 5.1, where the different amounts of NaH_2PO_4 and corresponding sample aspect ratios ν are presented. The Particle

Table 5.1: Overview of the amount used of NaH_2PO_4 and the resulting particle aspect ratio, ν, for the different samples prepared in this work using 0.020 mol/L of $FeCl_3$ ($m(FeCl_3) = 5.40$ g).

Sample identification	$m(NaH_2PO_4)$ (g)	ν
H1	0.056	5.0
H2	0.068	6.0
H3	0.030	2.7
H4	0.060	5.5
H5	0.035	4.0

aspect ratio is defined as $\nu = L \,/\, D_{eq}$, where L is the particle length and D_{eq} is the equatorial diameter of the particles. The particle size was determined by the TEM images.

The direct correlation between the different concentrations of NaH_2PO_4 and the spindle-hematite aspect ratios obtained during different syntheses is shown in Figure 5.2.

The spindles-shaped particles growth along the c-axis direction depends on two factors [97]:

1) Selective adsorption: the adsorption of $H_2PO_4^-$ is favourable to planes parallel to the c-axis [80, 95]. The interdistance $d_{Fe\text{-}Fe}$ = 2.29 Å at the plans parallel to c-axis fits much better to the distance $d_{O\text{-}O}$ = 2.50 Å than the iron-iron interdistance from the plans prependicular to the c-axis ($d_{Fe\text{-}Fe}$ = 2.91 Å) [80, 91]. Due to this regio-specific adsorption spindles-shaped particles grow preferably in the less blocked direction, which is along the c-axis. [80, 91, 95].

2) Concentration of hydroxide ions in the solvent: A slow hydrolysis of the transition metals salts controls the branching of the building blocks and leads to a guided growth [97].

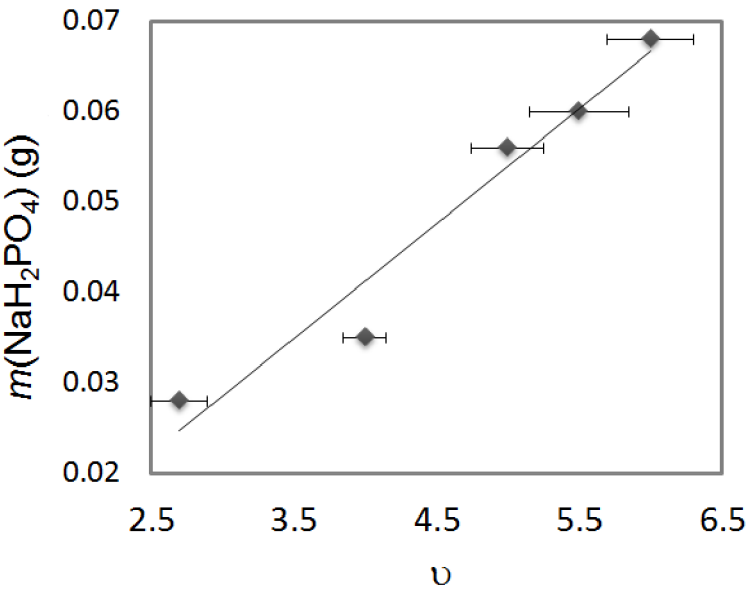

Figure 5.2: Relation between aspect ratio of spindle-hematite particles and the mass of NaH_2PO_4 used in different synthesis using 0.020 mol/L of $FeCl_3$ ($m(FeCl_3) = 5.40$ g).

Table 5.2: Overview of the position of measured and reference Bragg peaks presented in 5.3 as well as the corresponding planes.

Identification	Planes	q meas. ($Å^{-1}$)	q ref. ($Å^{-1}$)
a	(0 1 2)	1.70345	1.70445
b	(1 0 4)	2.32425	2.32568
c	(1 1 0)	2.49245	2.49279
d	(0 0 6)	2.73972	2.73925
e	(1 1 3)	2.84512	2.84512
f	(2 0 2)	3.02201	3.02253
g	(0 2 4)	3.41077	3.41290
h	(1 1 6)	3.70645	3.70671

5.3 Sample characterization

Spindle-shaped hematite particles were pre-characterized in terms of their size, shape, morphology and crystalline structure. The results using XRD, TEM, HRTEM and SAE as characterisation techniques are presented in the next sections.

5.3.1 XRD

The hematite particles were characterized by X-ray diffraction (XRD) using the basic method of packing randomly oriented powder in a flat cavity of the sample holder [1]. XRD characterization was used to determine the crystalline structure and phase composition of the samples.

The equipment used for the XRD analysis is a PANalytical XPert PRO MPD X-ray diffractometer in parallel beam geometry, using a characteristic Cu Kα radiation (λ = 1.5406 Å), with a Bragg-Brentano geometry.

The analysis was performed using X'pert Highscore plus programe to compare the experimental data to a reference structure file pattern with identified phase, using the Hematite (α-Fe_2O_3) PDF-card-Nummer: 01-087-1166.

From XRD patterns it is possible to identify the phases present in a sample and obtain information of its structural properties (cell parameters, lattice type, atomic parameters, crystallinity, particles size, strain, preferred orientation) analyzing the position, intensity and shape of the peaks [98].

The X-ray diffraction pattern of the nanoparticles is shown in Figure 5.3). From the XRD pattern it is observed that the entire diffracted peak obtained closely matched with the reference patterns, as can be checked as well in the table 5.2. Were an overview of every Bragg diffraction peaks measured and from the reference pattern are presented with the corresponding planes.

The synthesized sample can be indexed as α-Fe_2O_3 phase with an hexagonal structure with the space group $R\overline{3}$c and lattice parameters of a =5.04 Å and c =13.77 Å.

[1] These measurments were performed at the University of Hamburg by Birgit Fischer and colleagues.

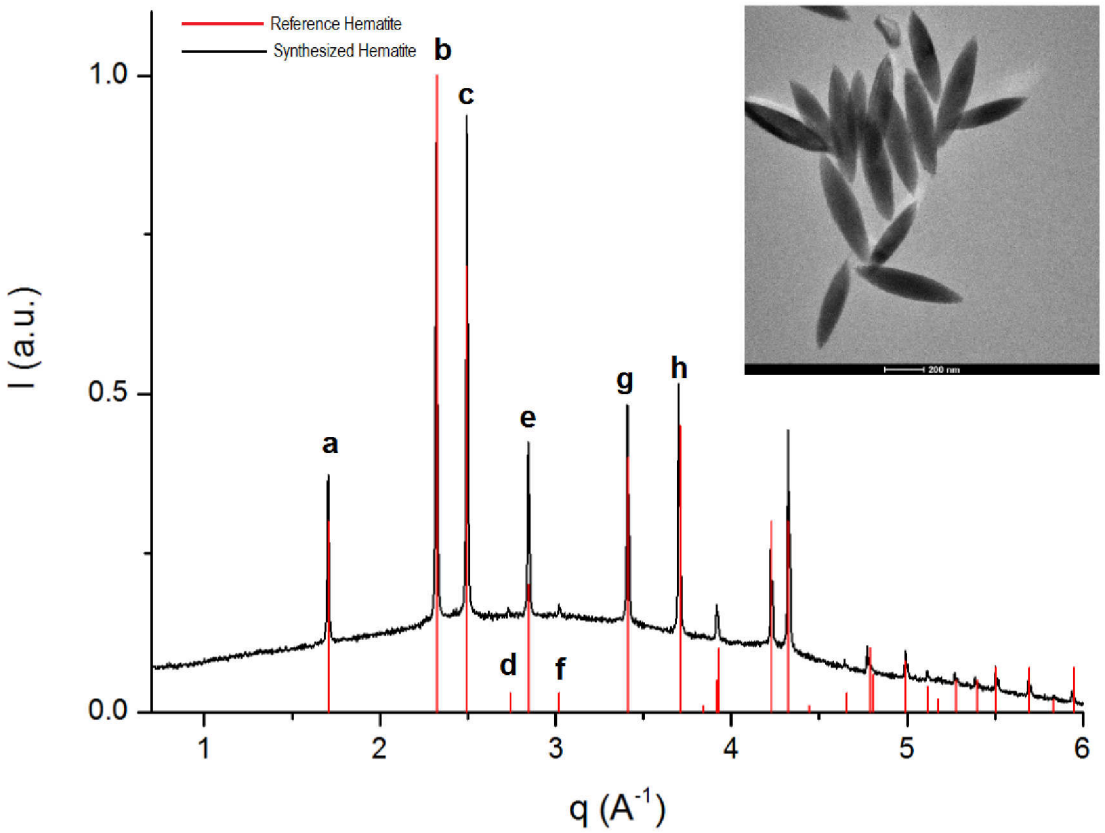

Figure 5.3: Powder diffraction pattern for sample H1 (black line) and the corresponding reference pattern (red line) [13].

5.3.2 TEM

Transmission Electron Microscopy (TEM) is a very useful technique for the visualization of the internal structure of materials by the phase contrast imaging of a thin specimen.

The morphology and the micro-structure of the Fe_2O_3 samples were characterized by TEM [2]. TEM micrographs of the samples H1, H2 and H3 are presented in Figure 5.4.

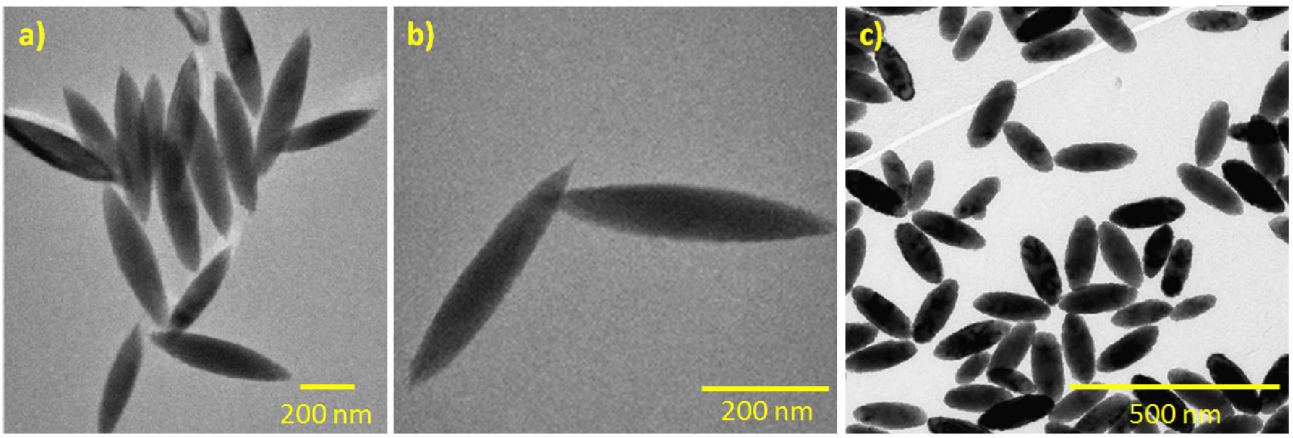

Figure 5.4: TEM images of samples a) H1 b) H2 and c) H3 with aspect ratio, $\nu = 5.0$, 6.0 and 2.7 respectively.

TEM imaging was carried out on a JEOL JEM 1011 at 100 kV. To investigate the nanoparticles a

[2]These images were taken at the University of Hamburg by Andreas Kornowski and colleagues.

drop of the diluted colloidal suspension was deposited on a carbon coated copper 400 mesh grid and dried.

The TEM results show the spindle-like shape of the nanoparticles with dimensions of: L= 500 and $D_{eq.}$ =100 nm, image a), $L = 545$ nm and $D_{eq.} = 90$ nm and image b) and $L = 249$ and $D_{eq.} = 90$ nm for image c). Thus, an aspect ratio of $\nu = 5.0$, $\nu = 6.0$ and $\nu = 2.7$, respectively, was determined and presented in Table 5.1.

5.3.3 HRTEM and SAED

In order to obtain information about the nano-particles size, their crystallinity and morphology, HRTEM (High Resolution TEM) and SAED (selected area electron diffraction) was applied [3]. HRTEM was carried out on a JEOL JEM 2200 FS at 200 kV equipped with two CEOS Cs correctors (CETCOR, CESCOR) and a Gatan 4K UltraScan 1000 camera. To investigate the nanoparticles a drop of the diluted colloidal suspension was deposited on a carbon coated copper 400 mesh grid and dried.

HRTEM and SAED images from sample H3 are presented in Figure 5.5 (Micrographs for sample H2 are presented in the Appendix C).

The HRTEM in Figure 5.5 a) shows one spindle-shaped particle randomly chosen with 2 selected areas for high resolution imaging analysis. These areas are depicted in Figure 5.5 images b) and c) where the alignment of crystal plane with d_{hkl} values of 0.229 nm and 0.252 nm correspond to the lattice distance of planes (0 0 6) and (1 1 0), respectively. These lattice distances indicate a well-defined sample crystalline structure of the nanoparticle compared to literature, see Figure 5.3.

While at first sight the rough surface of hematite particles may indicate an undefined single crystalline structure, a detailed analysis of HRTEM images of particles from different syntheses reveals that every particle exhibits this characteristic morphology.

In Figure 5.5 d) a SAED pattern is shown, confirming the single crystalline structure. The dots in the micrograph indicates the presence of a single crystalline structure, additionally the interplanar distances between them represents the same values found in both HRTEM images. This Figure allows to conclude as well that the c-axis of the particle' unit cell is oriented parallel to the long axis of the spindle because the plane (0 0 6), that corresponds to the c-axis, shows perpendicularity relatively to the plane (1 1 0), corresponding to a_1-a_2 axes, Figure 5.1.

[3] These images were taken at the University of Hamburg by Andreas Kornowski and colleagues.

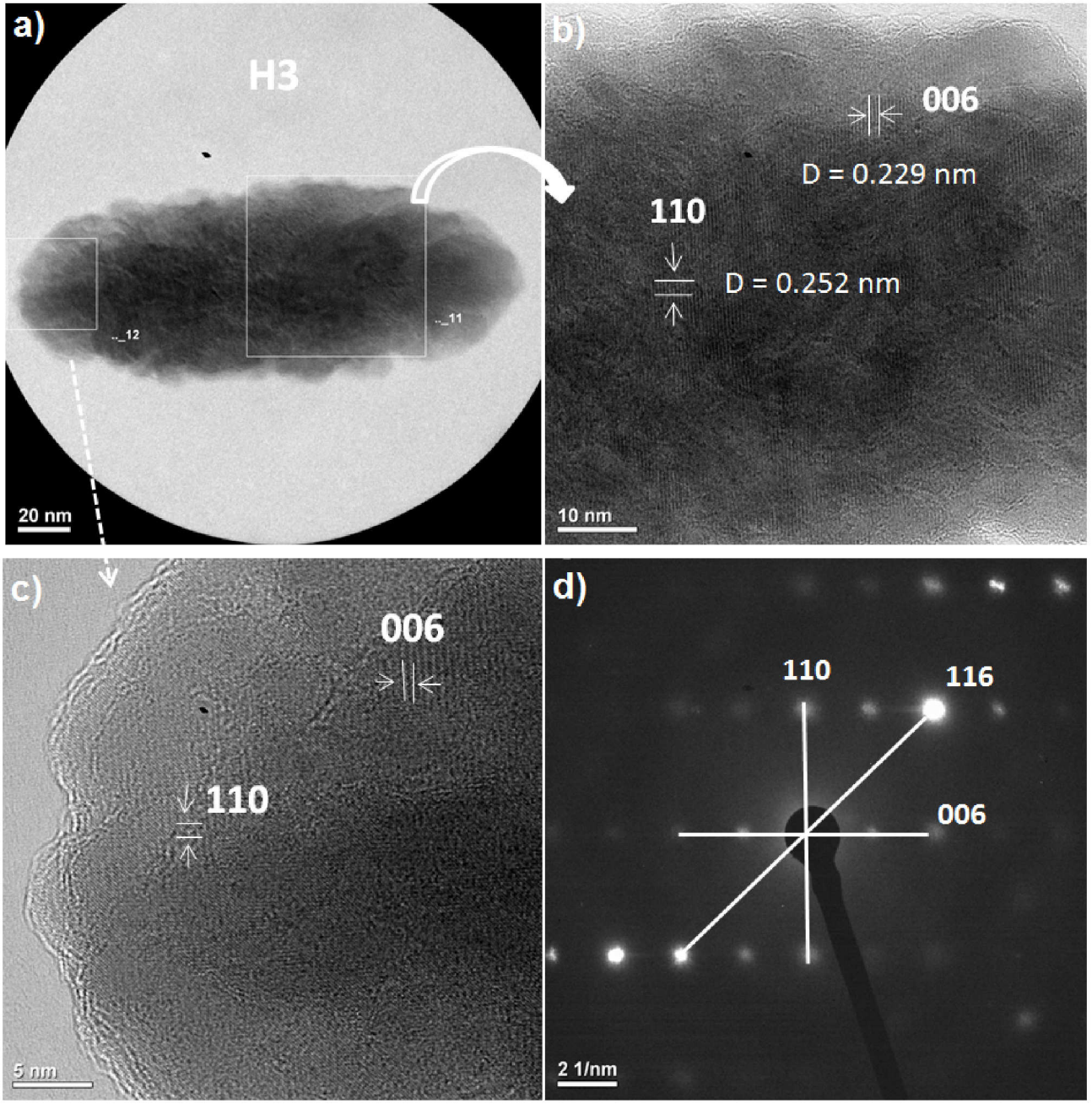

Figure 5.5: HRTEM and SAED patterns of spindle-shaped hematite particle (sample H3). a) One spindle-shaped particle randomly chosen with 2 selected areas for high resolution imaging analysis. Patterns b) and c) show the high resolution TEM micrographs from the areas depicted in a), showing the plans (0 0 6) and (1 1 0). d) The SAED pattern shows diffraction from (1 1 0), (0 0 6) and (1 1 6) planes.

Chapter 6

Experimental details

Liquid jets have become important sample injection devices following the demand of experiments at modern synchrotron and X-ray free electron light sources. The key advantage of using a steady stream injection system is that the sample is permanently refreshed, which allows for usage of thin samples avoiding sample damage. Thus, these injection devices are powerful tools for a variety of research purposes. Different sample environments are currently used for X-ray scattering experiments with liquid jets, which are specially installed at dedicated beamlines.

In this chapter a in-house built liquid jet setup is presented showing the modifications implemented to the setup in the framework of this thesis. The GDVN production and their common issues are presented as well as the beamline specifications and the experimental parameters used during the X-ray experiments.

6.1 Liquid jet setup

For a liquid jet system based on the GDVN environment a vacuum chamber was built, as shown in Figure 6.1 (see. [14, 15] for more details). The sample chamber comprises various parts, such as vacuum pumps, microscopes for in situ observation and diagnostics of the liquid jet, as well as a nozzle holder with multiple diagnostics tools [14].

Despite the liquid jet setup has proven to be valuable for X-rays measurements [14], some upgrades were performed to maximize the stability of some parts of the setup, such as holders, sample delivery systems and the jet characterization mechanisms.

In the framework of this thesis several improvements to the liquid jet setup were implemented, such as:

- **Holders** - New holders were created to increase the stability and decrease the time between measurements. Nozzles, diagnostics and magnetic holders were developed.

- **High speed camera** - A high speed camera was implemented to reach higher frames rate and high magnification to track the jet and droplets formation.

• **Injection devices** - A new injection device system was implemented to increase the stability of the jet formation.

First, new holders for nozzles, diagnostics and magnets were developed, which are more stable avoiding the vibrations observed before allowing as well more precise movements (Figure 6.2 a)). These holders replaced the previous ones which compromised the jet stability. For that reason, three types of holders were designed independently for diagnostic, nozzles and magnets. Before only two holders were available from where the different parts (diagnostics and nozzles) had to be changed in between the measurements.

The diagnostic holder contains a diode a knife edge and a ruler, see Figure 6.2 c) and d). The intensity of the direct X-ray beam is measured using the diode (Hamamatsu S3590-09), scanning the beam upstream the sample. Thus, intensity measurements can be performed without breaking the vacuum. Furthermore, the knife edge is mounted to measure the beam size at the jet position and a reference scale which can be calibrated to measure the jet dimensions. A fluorescent screen (YAG, Yttrium-Aluminium-Garnet) which is necessary to define the beam position is installed in all different types of the new holders (Figure 6.2 e)). Having all the diagnostics devices in independent holders makes the process of alignment and characterization of the beam and the jet faster and more accurate, since now only the complete holder needs to be changed.

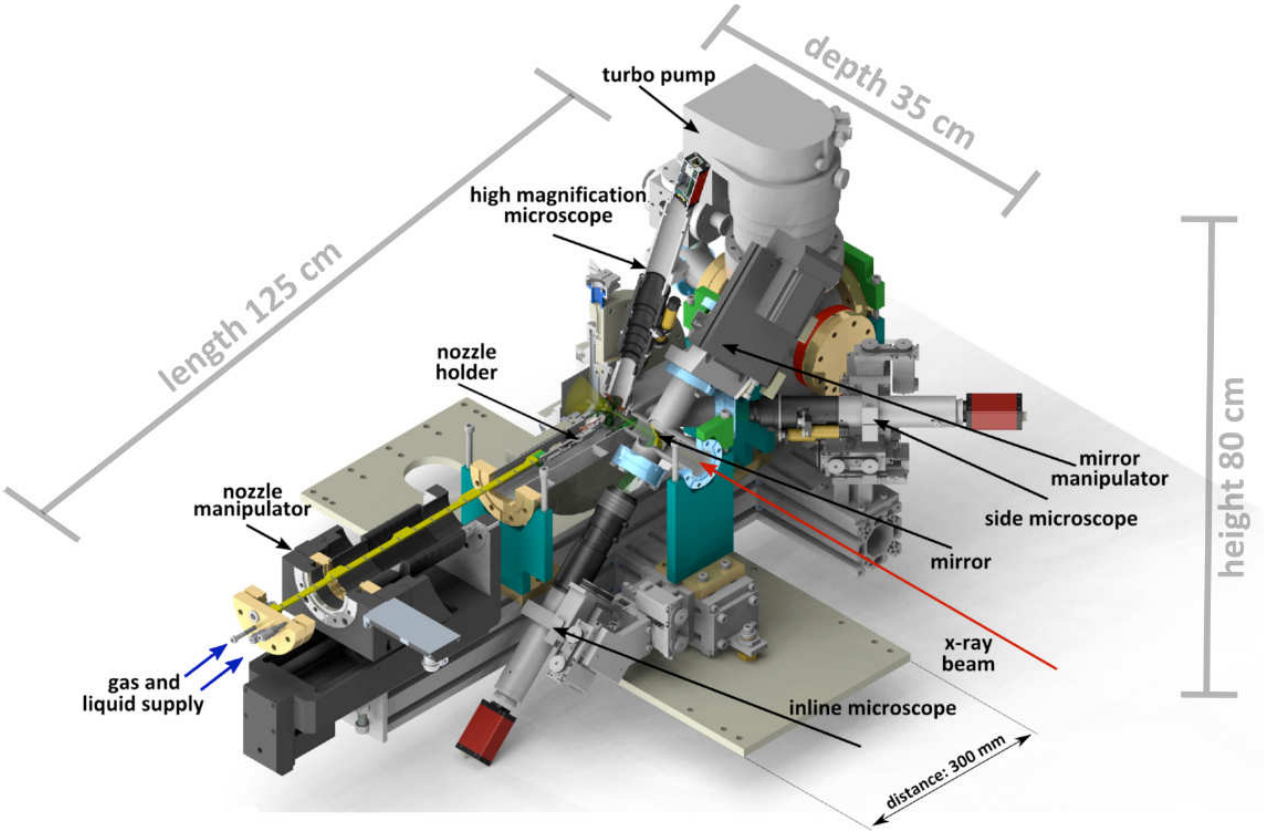

Figure 6.1: Liquid jet setup overview [14, 15]

The nozzles holder consists of two independent nozzles mounted together. Both have an independent pipes system what makes the nozzle change process faster and more stable since for that, the

vacuum doesn't need to be broken, it is only necessary to change the pipes' connections from outside de setup.

For the sample characterization, a holder with magnets was prepared, Figure 6.2 f), having this independent holder for sample characterization makes the time in between the measurements faster.

Second, a high speed camera (Phantom Vision Research V7.11) was implemented to the characterization and diagnostic chamber (Figure 6.3). It is a megapixel camera capable of taking 1400000 pictures-per-second allowing for exposures times below to 1 μs.

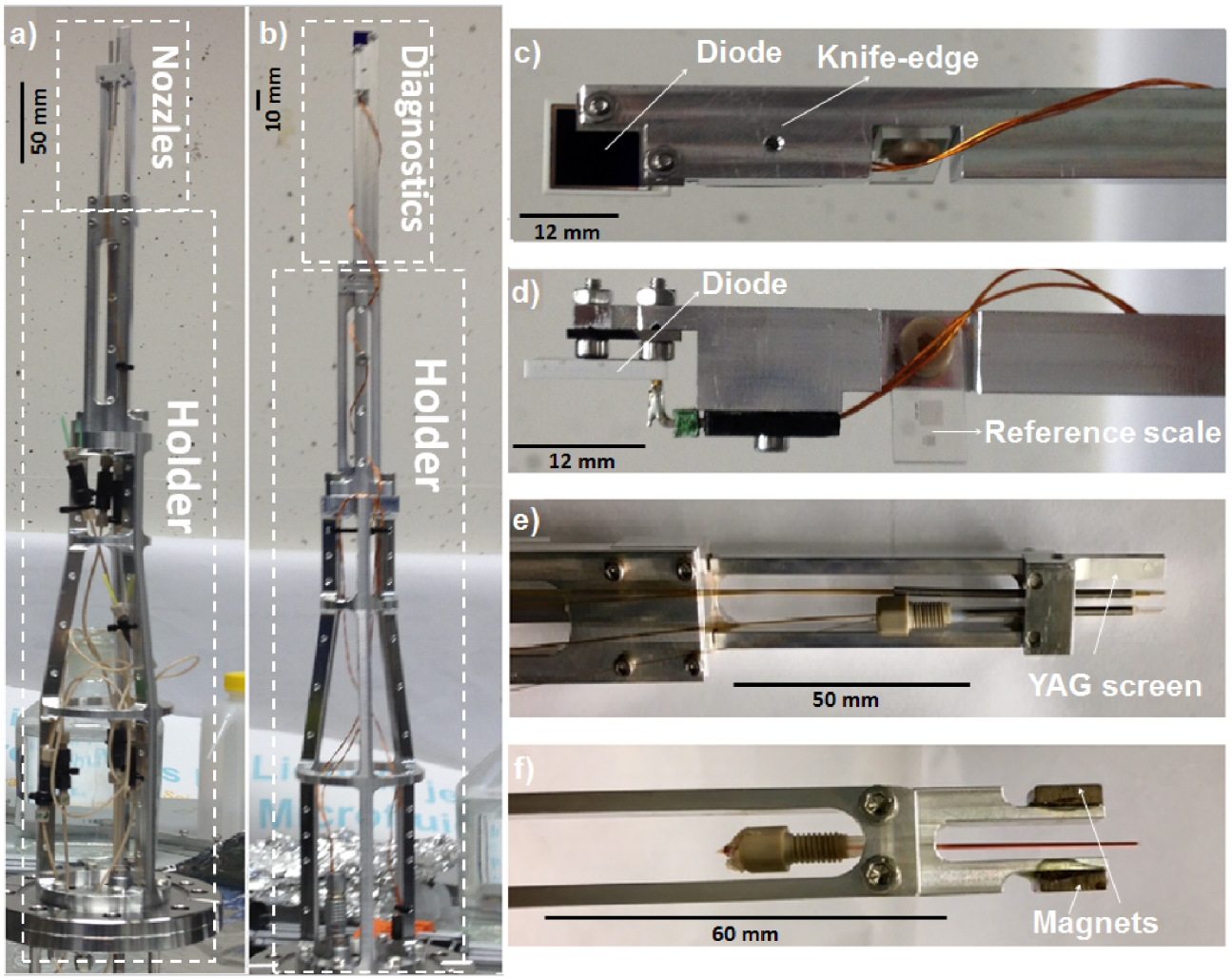

Figure 6.2: The photographs of the holders from nozzles, diagnostics and magnets. a) Holder with two different nozzles, b) holder with diagnostics parts. c)-d) Diagnostic devices of the holder presented in more detail. The diode, the knife-edge and the scale are visible. e) Holder showing two nozzles and the YAG screen. f) Hematite capillary in between the magnets in the characterization holder.

The high speed camera replaced a low magnification microscope, with a magnification factor up to 10 $\times$ and a focal length of 0.1 mm which did not allow to measure precisely the jet dimensions. The use of the high speed camera in the experimental chamber is possible as well, allowing to follow $in\ situ$, the jet and droplets formations as well as all jets details in a μm range, during the experiments. The high resolution, 1280 $\times$ 800, of hight speed camera enables precise control of the jet instabilities and droplet formation. To be able to follow the droplet formation in a continuous mode and being

able to monitor the shape alterations during the break-up regime in a μm range scale is of utmost importance since the break-up region is always a undefined zone of characterization.

Third, a new liquid injection device system was installed. It consists of a syringe pump (Mid Pressure Syringe Pump neMESYS 1000N) (Figure 6.3). This syringe pump is used instead of the nitrogen gas, used to press the liquid through the nozzle tube as described by Steinke $et\ al.$ [14, 15]. This system proved to be a very noisy system and unstable, compromising the jet stability. The high consumption of gas was as well a drawback.

The syringe pump system allows for dosing liquids with high accuracy down to the nano-liter range without any vibrations, thereby ensuring smooth delivery of liquids. Moreover, the control software is intuitive, making the syringe pump a user friendly system. The Middle Pressure module allows for high pressure applications, using rugged stainless steel syringes. The drive can apply pressure levels of up to 200 bar, therefore viscous liquids are accessible. Different volumes of the stainless steel syringes are available for this middle pressure device varying from 3 to 50 ml .

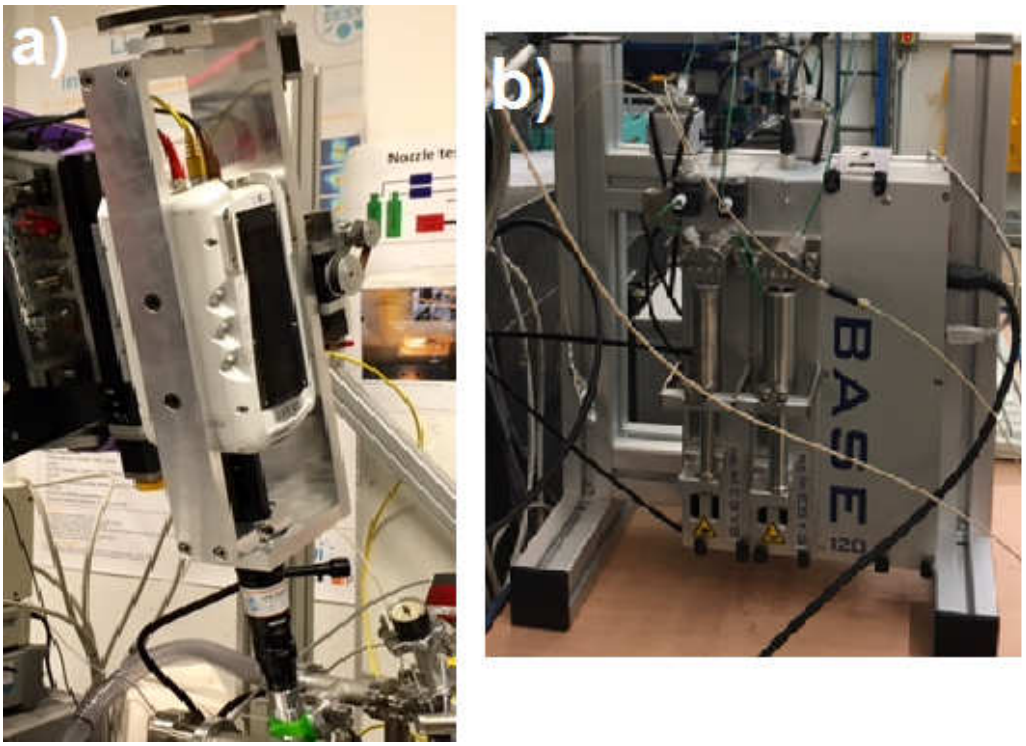

Figure 6.3: a) Phantom Vision Research (V-7.11) high speed camera. b) Module with two Mid Pressure Syringe Pump neMESYS 1000N, middle pressure.

The in-house built liquid jet setup is dedicated to small and wide angle X-ray scattering (SAXS and WAXS) experiments [14].

In the framework of this thesis three WAXS and one SAXS experiments were performed to study the behavior of hematite dispersions and water under shear flows. The results will be presented in chapter 7 and 8, respectively.

6.2 Gas dynamic virtual nozzles

6.2.1 Glass GDVN fabrication

The GDVN principle is based on a two-phase flow system which uses a pressured-gas sheet for the generation of liquid jets. These nozzles are known to be clogging-free, their design prevents the confinement effects and small volumes of sample can be used [99]. The conical shape of the nozzle plays a major role in the low flow rates achieved. It has been demonstrated that one way to have the minimum flow rates in stable jets is controlled by adjusting the nozzle geometry [7].

The gas dynamical virtual nozzles preparation are based in the work of Deponte $et\ al.$ [45], where the glass plenum is shaped and two microtubes prepared and assembled afterwards, to form the glass GDVN. The details of the preparation are described in the next paragraph and in the Figure 6.4:

Glass plenum construction The glass plenum is prepared by melting a glass capillary, using the "Melting machine" (Figure 6.5 a)). The desired cone-shape is acquired by polishing the glass over the flame.

Micro tubes preparation The liquid micro tube is polished in two different angles α_1 = 14 $^\circ$ and second the α_2 = 43 $^\circ$ as described by Deponte $et\ al.$ [45]. The result is the formation of two different angular phases as presented in Figure 6.4 b), for that, the grinding machine was used, Figure (6.5 a)), The second micro tube, which guides the gas to the nozzle tip, does not need previous preparation will be only assembled together with the glass plenum and the liquid micro tube.

After the preparation of the different parts, they have to be assembled. First, the glass plenum has to be glued into the metal tube. Then the polished micro tube has to fit to the conical shape of the glass plenum, and the micro tube tip sticks into the entrance of the glass plenum, as presented in Figure 6.4 b). In this way, a small gap is left in between the micro tube tip and the glass tip which has to be polished, until it became flat, using a silicone coated abrasive wheel. The micro tube for the gas supply has to end in the metal tube and subsequently both tubes are glued to one end of the metal tube. The final result in shown in Figure 6.4 c).

To prepare the GDVN different instruments were used as presented in Figure 6.5 a). The grinding machine is used to prepare the liquid micro tube and to have a glass flat tip, the melting machine to produce the conical shape in the glass plenum and a microscope for a check-up different parts of the nozzles during their fabrication and assembly. In Figure 6.5 b) a test chamber is shown, where the new nozzles are tested and jet characterization is performed beforehand.

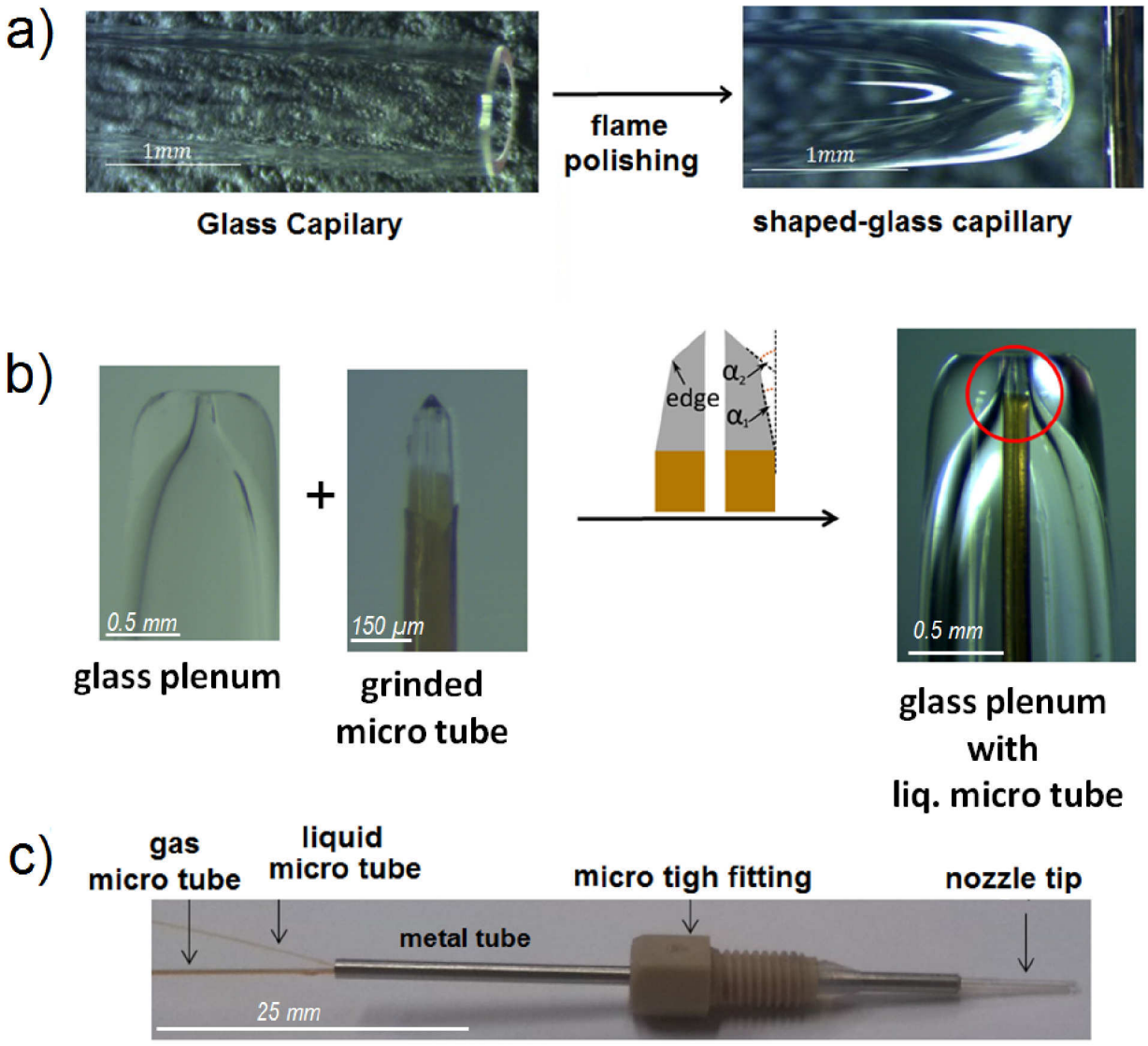

Figure 6.4: Scheme presenting the different steps for GDVN nozzle preparation. a) Glass plenum construction. b) Liquid micro tube preparation. c) Assembling.

Common glass GDVN issues and solutions

Despite all advantages in the GDVN production related to their design, there are still problems that can occur during their use:

1. Clogging - This devices can still clog easily if used with high viscosity or concentrated dispersions. A preliminary filtration of the sample is mandatory to avoid aggregates. Additionally, by running water through the nozzle between measurements the formation of agglomerates in the microtubes can be avoided.

2. Cooling - The nozzle operation in vaccum creates a fast cooling of the liquid, due to the intense evaporation. The system looses energy and the temperature goes down. Thus ice formation at the nozzle tip is a problem both for the nozzle performance and for sensitive detectors due to the strong diffraction from ice. In case of ice formation that eventually will clog the nozzle,

the liquid pressure should be immediately switched off and the gas pressure should be turned to maximum, in order to clean the microtubes.

3. Sample volume - Despite all efforts to reduce the sample consumption, injection systems based on GDVN technique are still using considerable amounts of sample (minimum 5 ml, for our setup). New designs and nozzles improvements are required to overcome this issue.

4. Production - Custom made glass GDVN have a low reproducibility, longer times of fabrication are needed and the "human error" is difficult to avoid. Therefore, with the manufacture process of 3D printing materials, the nozzle production became easier, faster and more reproducible. Despite some drawbacks, such as the limited resolution of 3D printers, the overall dimension limitations, and design restrictions imposed by the printing process, these nozzles are one of the most stable solution to overcome the "hand fabrication" glass GDVN.

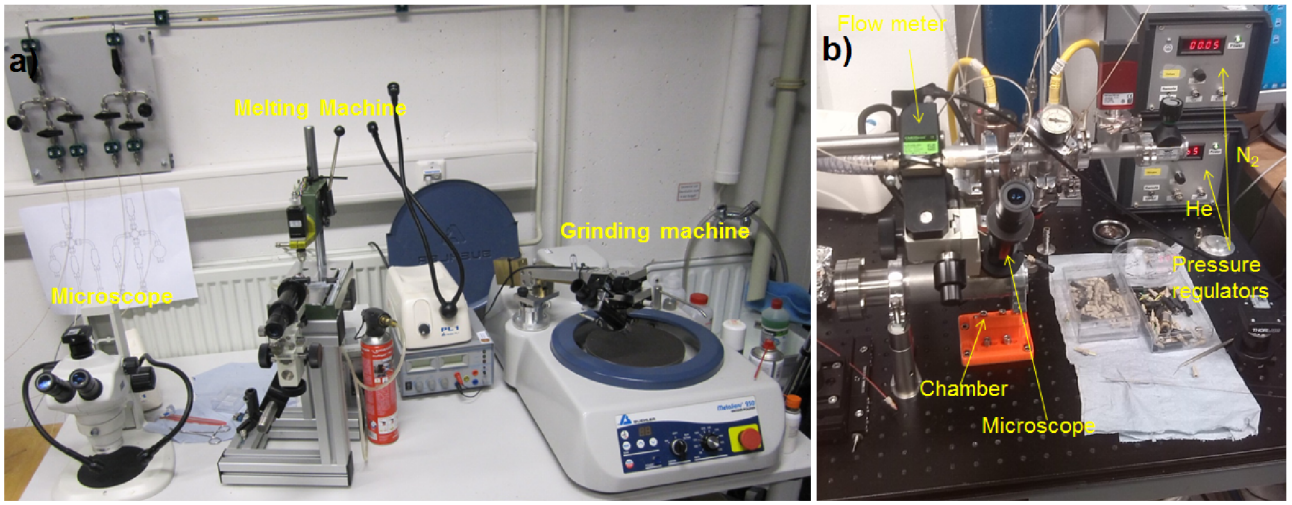

Figure 6.5: Photographs of a) the nozzles preparation table and b) nozzle setup characterization.

6.3 P10 Beamline

The experiments reported in this thesis were carried out at beamline P10 at PETRA III at DESY (a short overview of all experiments is shown in Appendix B). The P10 beamline is dedicated to coherent scattering techniques such as coherent diffraction imaging (CDI) and X-ray photon correlation spectroscopy (XPCS). It is located in a low beta section and takes advantage of the extreme brightness available at the PETRA III storage ring. Currently, the PETRA III synchrotron operates at 100 mA at 6.0 GeV [16]. The layout of the beamline is presented in Figure 6.6. Beamline P10 is equipped with a 5 m long U29 undulator as X-ray source and with a Si (111) double crystal monochromator. The source size is $\sigma_h \times \sigma_v = 39.5 \times 6.5\ \mu\text{m}^2$ ($h \times v$). Beamline components installed in the optics hutch (OH), experimental hutch 1 and experimental hutch 2 (EH1 and EH2, respectively) are depicted in Figure 6.6, where the principal components are highlighted. For more details about beamline P10 consult ref. [16].

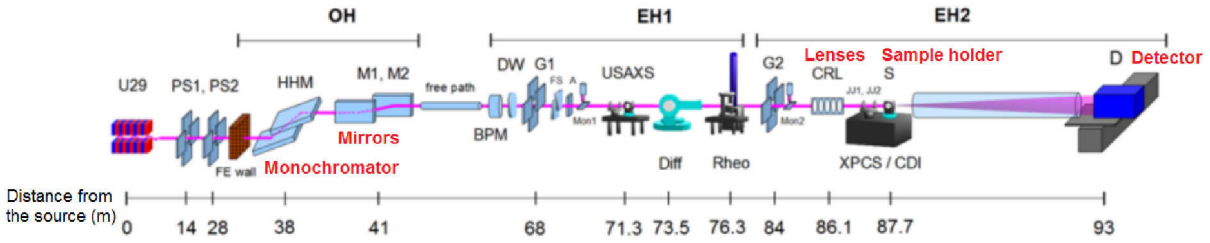

Figure 6.6: Schematic layout of the P10 beamline where the principal components are highlighted, namely the monochromator, mirrors and CRL lenses. [16].

Although it is not crucial to use a coherent beam in the liquids jet experiments of this thesis, the small dimensions of the focused beam as well as the available space in the hutch to set up the liquid jet environment makes the P10 beamline a good option. The Liquid jet setup was implemented in the experimental hutch 2 EH2, mounted on the diffractometer sample table (Figure 6.7).

Two experimental set-ups have been used, as referred above. In the WAXS beamtimes, Figure 6.7 a), the detector was positioned close to the exit flange while in the SAXS beamtime, Figure 6.7 b) a flight path is visible which separates the sample from the detector. In both experiments the beam was focused using compound refractive lenses [100] and the Pilatus 300K detector was used.

The Wide-angle X-ray scattering (WAXS) experiment involved an investigation of hematite spindle-shaped water suspensions in liquid jets using various jet sizes and different particle aspect ratios. The sample to detector distance was 110 mm, which gave access to momentum transfer values between $q_{\min} = 0.8$ Å^{-1} and $q_{\max} = 3.5$ Å^{-1}. A focused X-ray beam of dimensions 4.2 μm $\times$ 2.2 μm ($h \times v$) was achieved at an energy of 13 keV. An overview of the liquid jet setup is presented in Figure 6.7 a), and the beamtime parameters are summarized in table 6.1.

Table 6.1: Experimental parameters from small and wide angle X-ray scattering experiments.

Experimental parameters	WAXS experiment	SAXS experiment
Detector	Pilatus 300 K	Pilatus 300 K
Distance sample/detector (cm)	11	500
q range (Å^{-1})	0 .8 - 3.5	3 $\times 10^{-3}$ - 0.05
Beam dimensions (h $\times$ v) (μm^2)	4.2 $\times$ 2.2	3 $\times$ 2.5
Energy (keV)	13	7.05
Samples	Water, H2, H3	Water, H1

The small angle X-ray scattering study was performed on liquid microjets and microdroplets. To record the SAXS patterns the Pilatus 300k detector was placed at 5000 mm jet-to-detector distance with access to wave vector transfers between $q_{\min} = 3\times10^{-3}$ Å^{-1} and $q_{\max} = 0.05$ Å^{-1} at the X-ray energy of $E_{\text{x-ray}} = 7.05$ keV. The beam size was focused to 3 μm $\times$ 2.5 μm ($h \times v$). In Figure 6.7 b) and c) the liquid jet setup in the EH2 is presented and the experiment details are summarized up in the table 6.1.

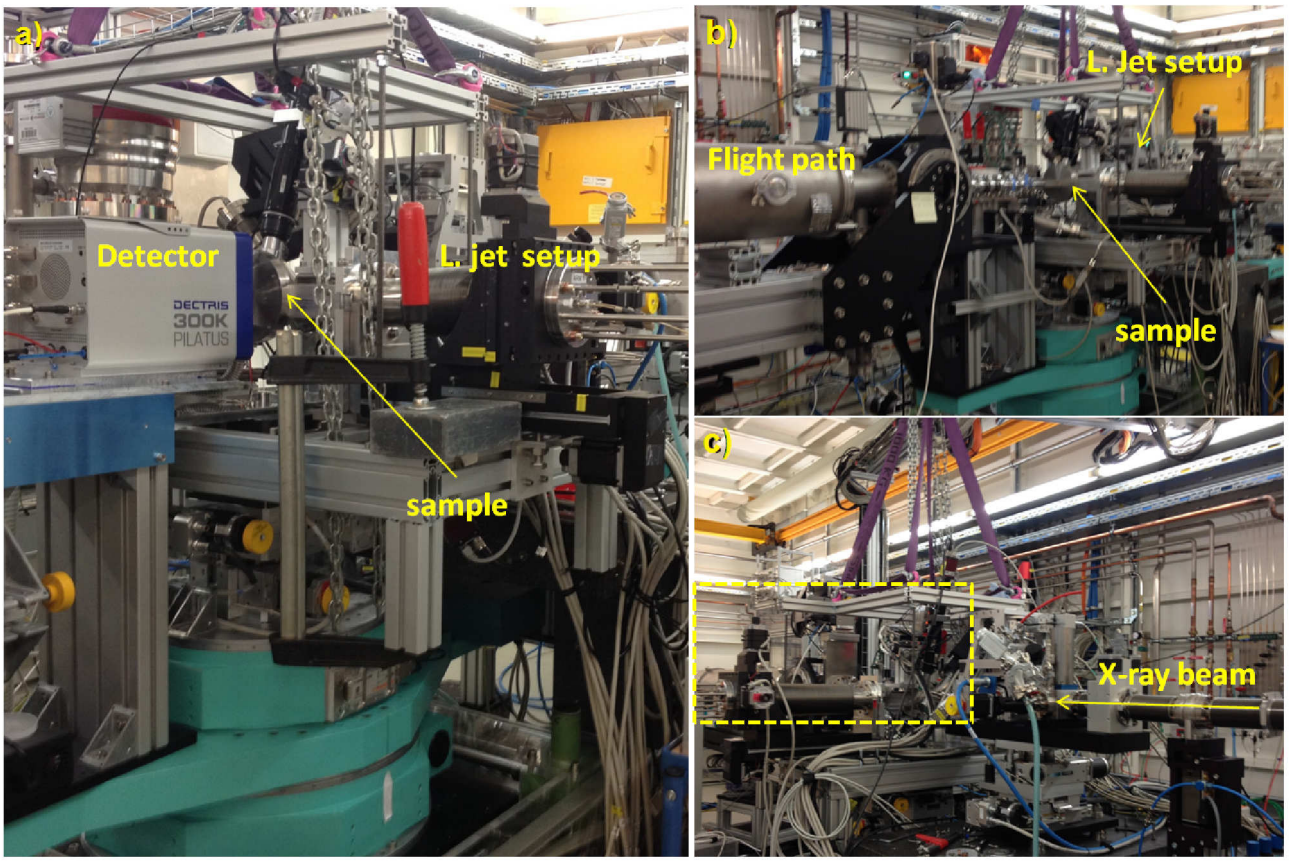

Figure 6.7: Liquid jet setup at P10. a) WAXS and b) SAXS configurations. c) The general overview of beamline P10, EH2, with the liquid jet instrument set-up.

Chapter 7

Elongated particles in shear flow - WAXS study

Macroscopic properties of particles in flow have been studied for decades but the connection of these phenomena with the microscopic structure in flows is mainly limited to theoretical studies. Thus, an experimental study reporting on the physics of flows as well as on the behavior of spindle-shaped particles under shear is highly important.

In this chapter, a structural relaxation study of water dispersions of hematite spindles is presented covering the regime from sheared to unsheared flow regions produced by a GDVN. The orientation of spindle-shaped particles in the flow is determined by a WAXS study using particles with different aspect ratios and molar fractions.

7.1 Microjets and measurements descriptions

The jets were formed with a GDVN using a capillary micro tube (Polymicro GmbH, inner diameter d_i = 20 - 50 μm and outer diameter, d_o = 150 μm) as a guide to the liquid flow. For the gas a second capillary was used (d_i = 100 μm and d_o = 375 μm). These focused liquid jets were stable working at a pressure of p = 10^{-3} mbar inside the vacuum chamber.

The jet characterization was done *in-situ* using the high magnification microscope and reference scales from the diagnostic holder described in chapter 6 and in ref. [14]. Figure 7.1 shows an image of the horizontal jet orientation and the initial part of the droplets regime taken during the experiment using the stroboscopic microscope. The axis directions, jet_y and jet_z, as well as the flow direction and the nozzle exit are shown as well. Jets with 2 - 10 μm diameter and break up lengths of approximately 100 - 450 μm were produced by the GDVN. The observed droplet diameters after the break up point, varied between 10 and 35 μm.

The difference between jet and droplets diameter is in accordance to Rayleigh estimation, see equation 2.16, and in agreement with experimental work by Lin and coworkers [40, 48], as shown in chapter 2.3.1. The ratio between droplets and jet diameters also follows our results obtained during the jet characterization studies, presented in chapter 2.3.1.

A flow rate of approximately Q $\sim$ 20μl/min was set in the syringe pump to press the liquid through the tube. Thus, an average jet velocity in the tube can be estimated as $V_{\text{jet.}} = Q/A_{\text{b}} \sim 0.17$ m/s, where A_{b} is the cross-sectional area of the tube which diameter is 50 μm.

Using 25 μm as the jet radius inside the tube, corresponding to the radius of the pipe, the calculated shear rate is of $\dot{\gamma} = 2.7\times\ 10^4\ \text{s}^{-1}$. For the shear rate determination, the equation that describes Newtonian flows behavior in a pipe was used [101]: $\dot{\gamma} = (8.V_{\text{jet}})/d_{\text{jet}}$.

Assuming Browning motion in a dilute dispersion the rotational diffusion, D_r, of the spindles-shaped particles can be calculated by modifying equation 3.7. For anisotropic particles one obtains [102**?**]:

$$D_{\text{r}} = \frac{3k_BT(2\ln(2\nu) - 1)}{16\pi\eta a^3}, \tag{7.1}$$

where a and ν are the half length and the particle aspect ratio, respectively. The rotational diffusion coefficient was calculated for sample H2 (a =272 nm and $\nu = 6$) using equation 7.1 resulting in Dr $\approx$ 50 rad^2/s, which is in good agreement with simulated data reported by C. Passow [103].

Afterwards the Péclet number in the pipe Pe can be determined by Pe $= \dot{\gamma}/D_r$, resulting in Pe = 135 which indicates an high impact of the shear in this colloidal dispersion (see Péclet number description, chapter 2). This rheological behaviour of spindle shaped particles was studied by Gunes *et al.*, concluding that high Péclet numbers (Pe>70) suggest a particle alignment in the flow direction [72].

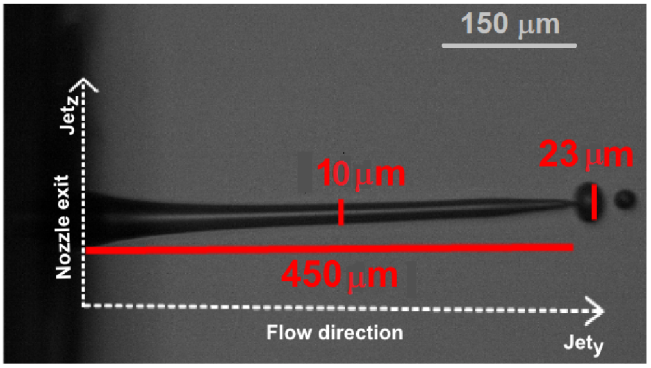

Figure 7.1: Microscope image taken with the stroboscopic microscope. Dark part on the left side of the figure is the nozzle with a inner tube diameter of 50 μm. Jet formed by sample H2 with a jet length L_{jet} = 450 μm jet diameter d_{jet} = 10 μm and at the initial part of the break up with droplets diameters $d_{\text{drop.}}$ = 23 μm. The nozzle exit and flow direction are sketched as well.

The X-ray scattering measurements in liquid jets were performed along the jet at distances between 50 μm and 1000 μm downstream the nozzle exit. Note that measurements started only at 50 μm downstream the tip to avoid the shadow from nozzle tip interfering with the data. Across the jet, WAXS patterns were recorded in steps of 1 μm with an exposure time, t_e = 1 s, and approximately 20 frames were taken at each spot. Every diffraction pattern taken across and along the jet was corrected by background subtraction using a WAXS pattern without the jet.

7.2 Sample characterization in magnetic field

As discussed in section 5.1 , hematite particles can be aligned under an external magnetic field. Wide angle X-ray scattering was used to characterize hematite samples in a glass capillary under an applied magnetic field. This procedure allows for static measurements of aligned (in B-field) and randomly (without B-field) oriented particles and will be used to understand the particle's behavior in the liquid jet.

The behaviour of spindle-shaped hematite particles using an external magnetic field was intensively studied in the literature, details in chapter 5. Thus, it is known that under a magnetic flux density of B = 120 mT spindle-shaped particles, with aspect ratio's between $1 < \nu < 5$, are oriented perpendicular to the field direction [104].

The analysis presented in this section reports an experimental study on WAXS patterns collected in a static environment under an external magnetic field using different hematite samples. This study is complemented with a model study on the spindle-shaped particles behavior under a magnetic field.

Experimental data analysis

For a structural characterization of hematite crystals, static measurements using WAXS were performed. This technique specifically refers to the analysis of Bragg peaks at high angles, which implies that they are caused by sub-nanometer-sized structures.

The hematite suspensions were measured in glass capillaries under an external magnetic field of $B \approxeq 150$ mT, since it was shown to be enough to orient the particles perpendicularly to the magnetic field [104].

Before the structural information of the samples can be extracted, corrections had to be applied to the raw data:

1. Every pattern was corrected for background scattering by subtracting a pattern taken without sample.

2. The linear polarization reduces the scattering at high angles, thus a correction to the horizontally polarized beam was introduced by dividing the intensity of each pixel by:

$$\alpha_{pol} = C_{horz}[1 - \sin^2\phi \sin^2\theta] + C_{vert}[1 - \cos^2\phi \sin^2\theta], \tag{7.2}$$

where C_{horz} is the fraction of horizontal polarization (in this case 100 $\%$), and C_{vert} = 1 - C_{horz} is the fraction of vertical polarization (in this case 0 $\%$), ϕ is the azimuthal angle of the pixel (respective to the positive vertical axis) and θ is the scattering angle of the pixel. For more details see the work of Sellberg $et\ al.$ [105].

1. The use of large angles and short sample - detector distance means that Edwald sphere curvature effects will be present in the recorded scattering patterns. The scattered intensities, recorded

on a plane detector, represent the projection of the Ewald sphere and are offset radially by a distance in q-space [106, 107]. The offset was calculated as $\lambda^2 q^3/2$, where the wave vector q is $q = \sqrt{(q_x^2 + q_y^2)}$ in a plane detector.

2. Finally, bad pixels were masked out.

To calibrate the sample-detector distance, the tabulated q values [13] of intense Bragg diffractions from the hematite crystal structure were used.

In Figure 7.2 a schematic picture describing the static measurement is shown. The sample is located in the glass capillary under the magnetic field holder. $\vec{B}$ represents the magnetic field vector direction which generates a magnetic field of 150 mT, $\vec{K_i}$ represents the beam direction and $\vec{q}$ the wave vector transfer with coordinates q_x and q_y.

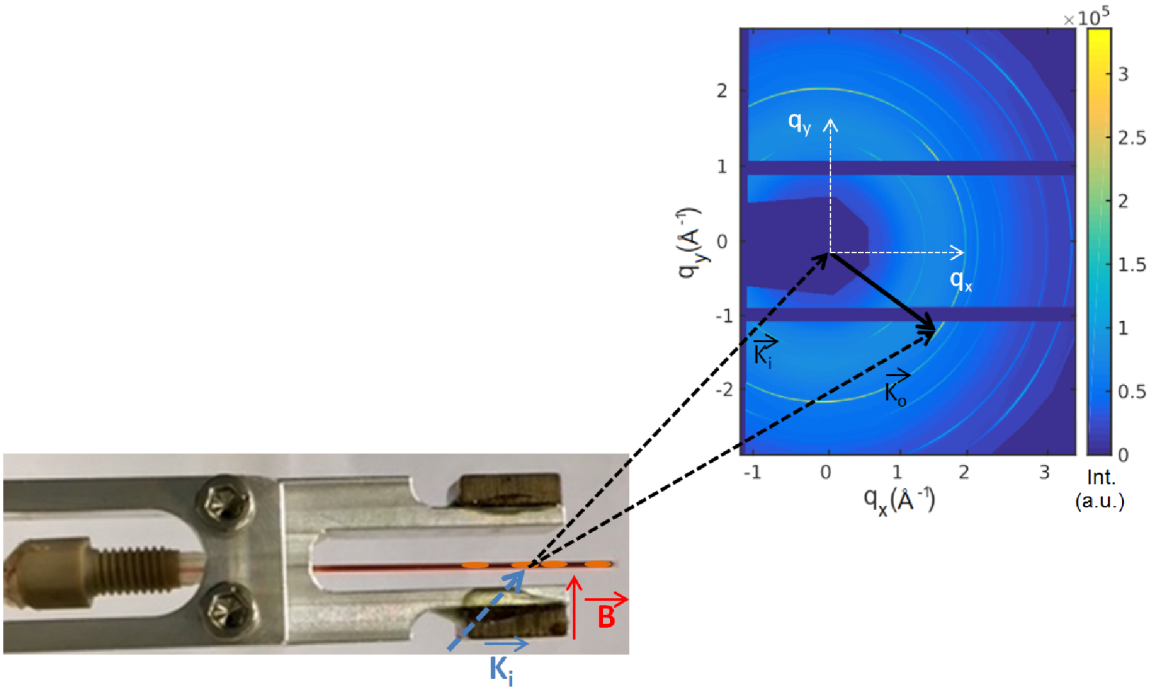

Figure 7.2: Sketch of the static measurement of the hematite sample under a magnetic field. The sample capillary is placed between the magnets which generate a magnetic field of $B \approx 150$ mT. $\vec{K_i}$ represents the incident beam direction. On the right side, the scattering pattern collected by the detector is shown.

In Figure 7.2 the detector image shows the characteristic Bragg diffractions from hematite particles, as indicated by discontinues rings showing an alignment of hematite spindles due to the presence of the magnetic field.

For the characterization of sample H2, 100 patterns were recorded with an exposure time of t_e = 1s each. After corrections as explained above, all patterns were averaged (see Figure 7.3).

In Figure 7.3 a) a hematite scattering pattern measured without magnetic field is shown. The pattern is isotropic which is characteristic for randomly oriented spindles. For comparison, Figure 7.3 b) shows a scattering pattern from hematite spindles measured under an applied magnetic field. As it can be seen from Figure 7.3 b) incomplete Debye-Scherrer rings are visible which indicates alignment of hematite spindles (see chapter 4) with the long axis orientated perpendicular to the magnetic field

direction, due to the position of the reflections, as it is known from literature (see [80] and section 5.1).

The Bragg diffractions identified as a-h in Figure 7.3 b) correspond to the diffractions equally named in table 5.2. These Bragg diffractions are assigned to the characteristics diffraction reflections from the hematite spindles.

In the framework of this thesis two the most intense Bragg diffractions denoted as b and c will be analysed in more detail:

- b belongs to the reflection (1 0 4), $q_{104} = 2.324$ Å, with four characteristics reflections, two in the positive q_x and two more in the negative q_x (not visible).
- c belongs to the reflection (1 1 0), $q_{110} = 2.493$ Å, with two characteristics reflections, one at the positive q_y and the other one at negative q_y.

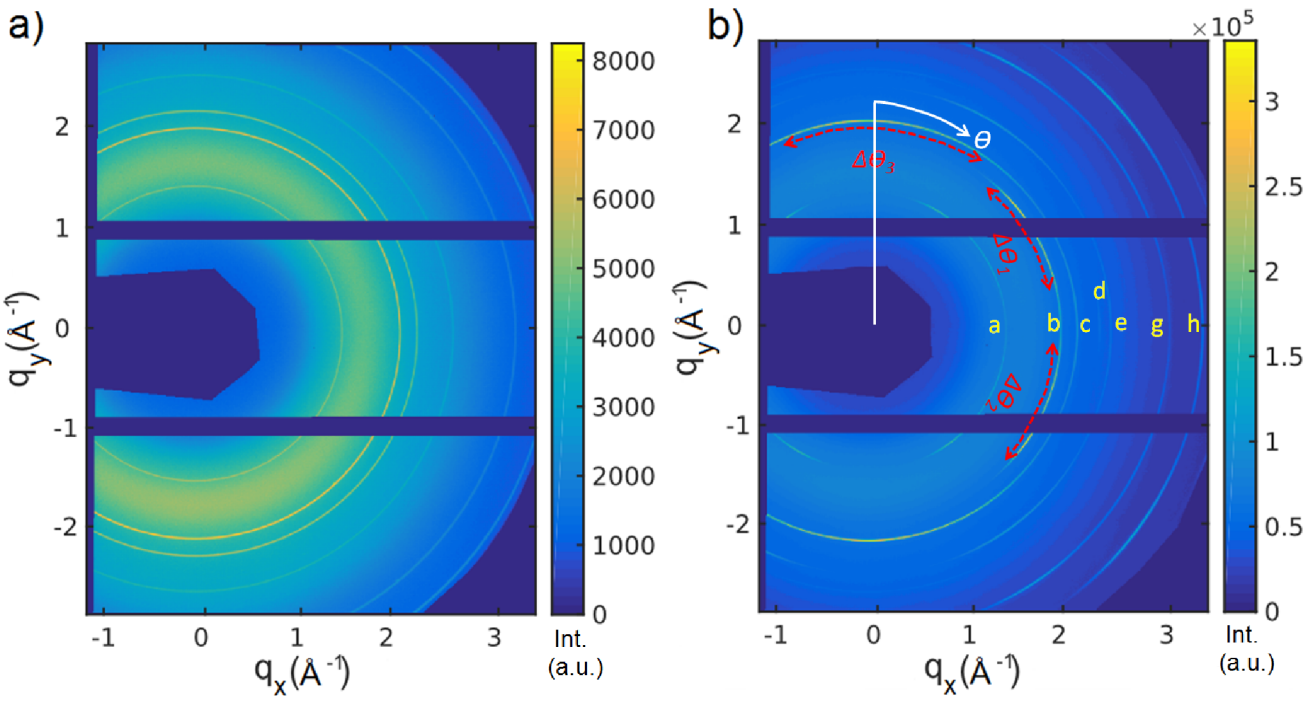

Figure 7.3: Diffractograms of hematite sample H2 averaged over 100 patterns, measured a) without magnetic field and b) under an external magnetic field of $\vec{B} \approx 150$ mT. Bragg diffractions referred to as a-h correspond to the planes obtained from XRD pattern shown in the table 5.2. The red dashed lines are mark the reflections for planes (1 0 4) (θ_1 and θ_2) and plane (1 1 0) (θ_3).

Note that in Figure 7.3 b) a small and weak Bragg diffraction denominated as d is present and not in Figure 7.3 a) where particles are randomly orientated. This is the (0 0 6) reflection which is parallel to the particle major axis. The presence of this reflection indicates that particles has a preferable orientation at this position since is the only way to fit the Bragg condition.

In Figure 7.4 a) radial integration of the two-dimensional pattern presented in Figure 7.3 b) is shown as a function of the intensity $vs.$ wave vector q. The red line represents the signal from sample H2 and dashed black line the water background signal with its maximum structure factor at around

$q = 2$ Å^{-1}. The well defined Bragg peaks in Figure 7.4 a) observed in the hematite scattering pattern corresponds to the reflections identified in Figure 7.3 b) (a-h).

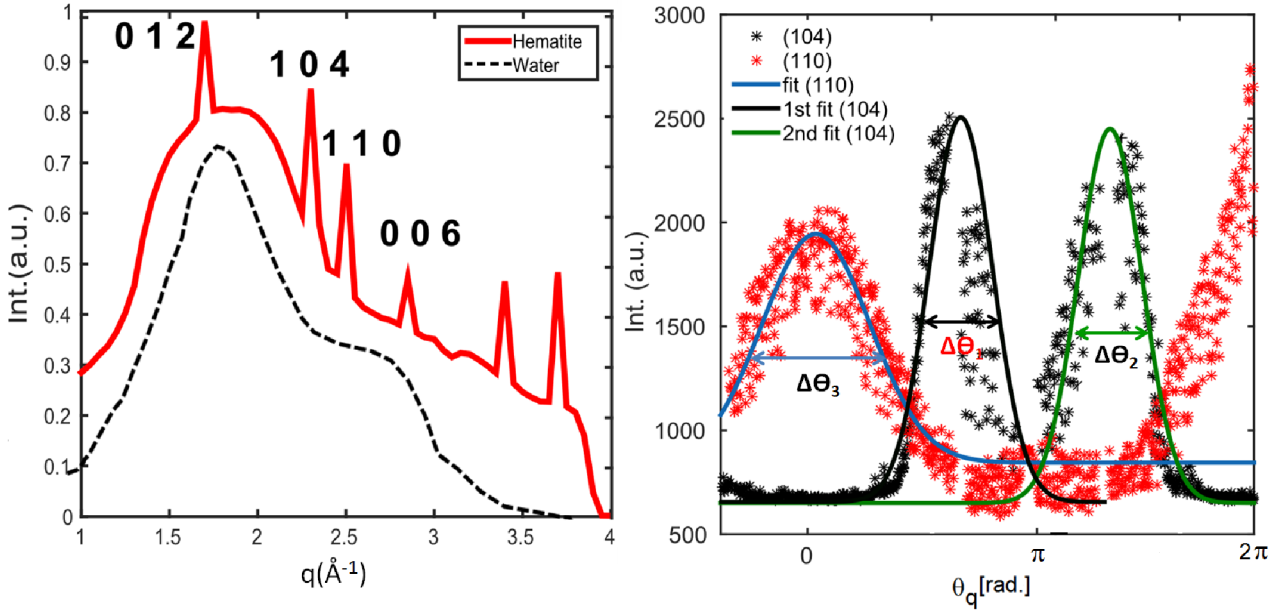

Figure 7.4: a) Azimuthal integration $I_{(q)}$ of the diffractogram shown in Figure 7.3 b). Red line represents the hematite signal and additionally a water signal is shown as the background contribution (black dashed line). b) Azimuthal cut of the (1 0 4) reflection at $q = 2.32$ Å^{-1} (black stars) and of the (1 1 0) reflection at $q = 2.49$ Å^{-1} (red stars) with the corresponding fits obtained using a Gaussian function. The azimuthal widths, $\Delta\theta_1$, $\Delta\theta_2$ and $\Delta\theta_3$, of the Bragg diffractions correspond to the reflections widths labelled in Figure 7.3.

An azimuthal cut $I(\theta)$ of the reflections (1 0 4) and (1 1 0) is shown in Figure 7.4 b). The azimuthal widths $\Delta\theta_q$ of the Bragg peaks were extracted by fitting the incomplete Debye-Scherrer rings data with a Gaussian function by:

$$f(\theta_q) = A \cdot \exp([\theta_q - \mu]^2/\sigma_s^2) + d, \tag{7.3}$$

where A is the amplitude, θ_q is the azimuthal width, μ is the azimuthal location, σ_s is the standard deviation and d a constant used for the baseline. Note that the baseline correction used was the same for all data, since this step can affect the width of diffraction peaks.

The determination of the azimuthal widths $\Delta\theta_q$ of the Bragg diffractions gives an indication of the particles' degree of alignment. As explained in section 4.4, broader $\Delta\theta_q$ corresponds to a lower degree of particles' orientation. The full width at half maximum (FWHM) W of Bragg diffractions are related to $\Delta\theta_q = \mathrm{W} = 2\sqrt{2\ln(2)} \cdot \sigma_s$.

Figure 7.4 b) shows the azimuthal cut resulting in an average of $\mathrm{W}_{(104)} = 24.9° \pm 1.2°$ and for $\mathrm{W}_{(110)} = 30.2° \pm 1.9°$.

Besides the known alignment of hematite spindles with their long axis perpendicular to the field direction the particles also rotate around the short axis. These particles' rotations are expected to result in azimuthally broader Bragg peaks, however from the data available is not possible to quantify

the degree of orientation of the particles. Thus, a model study was performed to quantify the particles' alignment in the magnetic filed.

Model study

The first step to model the WAXS signal [1] of the orientation of spindle-shaped hematite particles under a magnetic field is to generate the hematite unit cell using the unit cell parameters described in section 5.1. The structure factor of a unit cell and the atomic form factor for all atoms in the unit cell were calculated using equation 4.9.

To obtain a computed scattering pattern for spindles-shaped hematite particles with a perfect alignment under a magnetic field, some assumptions were taken into account:

1. The c-axis of the unit cell is oriented parallel to the particles major axis, as observed by the TEM images, thus, perpendicular to the beam direction.

2. Particles orient with c-axis perpendicular to the magnetic field direction.

3. Rotations around the small axes are allowed, supposing that all directions have equal probability.

4. For a perfect particle alignment is assumed that particles' c-axis do not suffer deviations, $\omega = 0°$, although, as in the experimental observations, particle rotations around small axis are allowed.

5. Particles' c-axis rotates 360° at each ω deviation.

The geometry from the simulated experiment of spindle hematite particles under a magnetic field is shown in Figure 7.5. As it is visible from Figure, in this model the imposed particles rotations are:

- 360° around c-axis, at each c-axis deviation.
- 360° in the plane Oz (indicate by green arrow).
- deviations in the plan Oxy were imposed to $0° < \omega < 20°$.

For a particle perfect alignment, perpendicular to the magnetic field direction, the calculated pattern is shown in Figure 7.6. In this situation, as explained above, the particle rotation around the small-axis is imposed similar to the experimental data as well as the rotation of 360° around c-axis. As visible in Figure 7.6 the Bragg reflections are represented by dots instead of the discontinues rings indicating that: 1) particles are single crystals. 2) particles c-axis is perpendicular to the magnetic field. The observed number of dots and their positions are characteristic for the different reflections of hematite samples.

However, the experimental Bragg reflections are characterized by discontinuous rings instead of the spots, thus an additional deviation of c-axis has to be assumed, labelled as ω in Figure 7.5, to be

[1] Simulations were performed by D. Sheyfer.

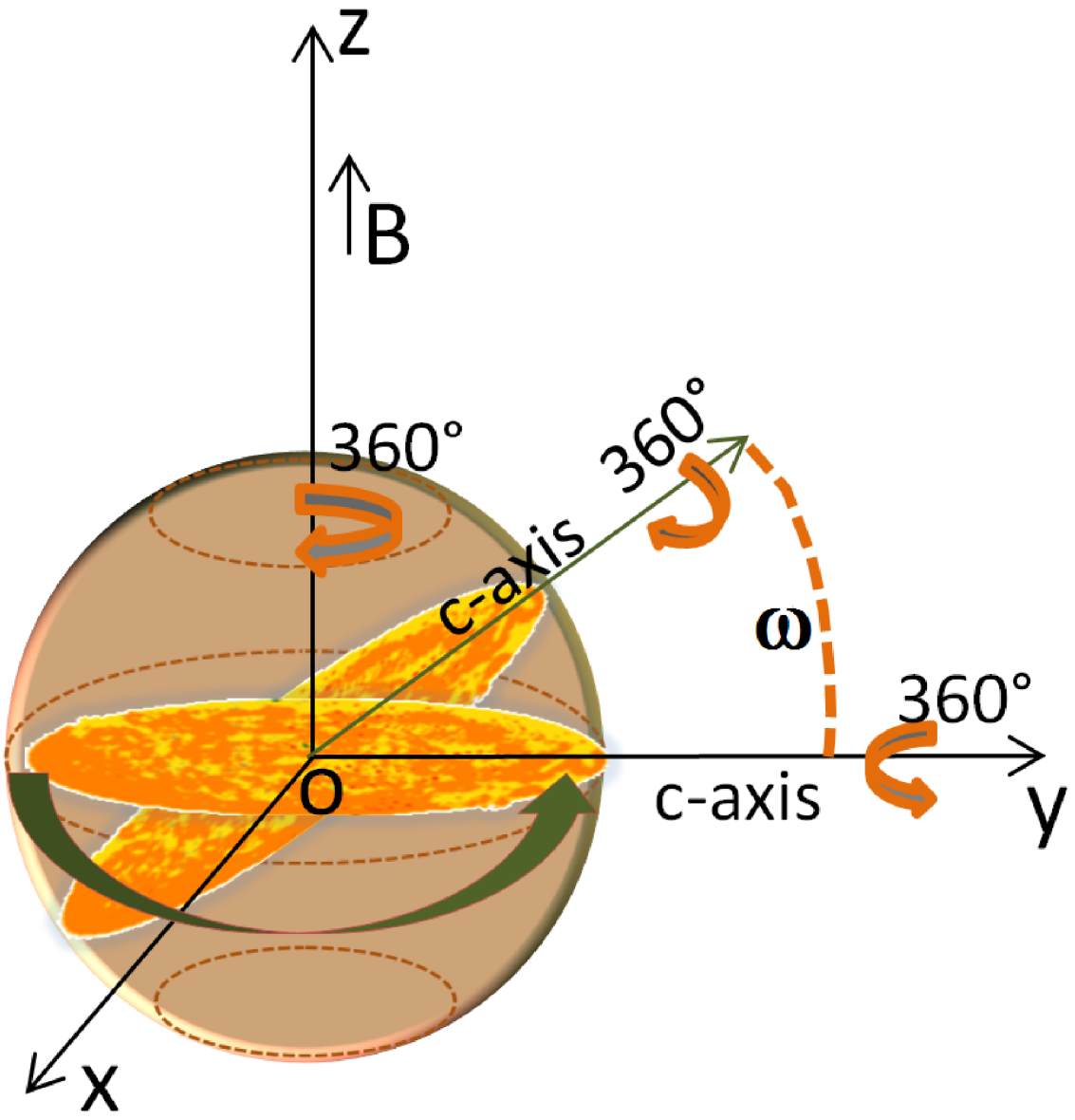

Figure 7.5: Geometry of the simulated experiment.

able to model the experimental data and understand the spindle behavior under an external magnetic field.

WAXS patterns with different c-axis deviations $0° < \omega < 20°$ were calculated, resulting in discontinues rings as Bragg reflections similar to the experimental data. The analysis of the WAXS patterns was performed similar to the experimental data. The calculated Bragg diffractions will be analysed in terms of the FWHM (W) of diffraction peaks and the peak position. The W of the peaks was extracted by fitting the data with a Gaussian model and averaged afterwards. The most intense reflections (1 0 4) and (1 1 0) will be analysed in more detail, as described in the experimental data analysis. C-axis deviation were imposed in the model as $0° < \omega < 20°$. The $I(\theta)$ for (1 0 4) and

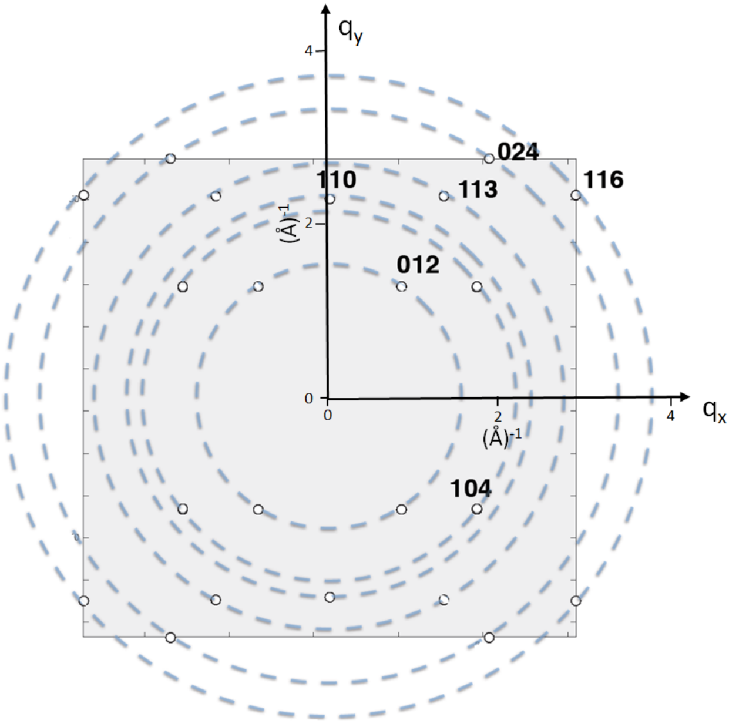

Figure 7.6: Simulated WAXS scattering pattern for a spindle-shaped hematite particle perfectly oriented. Particles' c-axis is assumed perpendicular to the external magnetic field, particles rotations around small axis are allowed as well as c-axis rotations of 360°. The number of dots (Bragg diffractions) and their positions are characteristic of hematite samples.

(1 1 0) Bragg reflections are depicted in Figure 7.7 with a $\omega = 12.5°$. The angular widths $\Delta\theta_1$, $\Delta\theta_2$ and $\Delta\theta_3$ of the Bragg diffractions corresponds to the diffraction amplitudes of the discontinues rings as shown for the experimental data analysis. The averaged W, extracted from the Gaussian fit, were $W_{sim,104} = 21.2° \pm 1.4°$ for (1 0 4) and $W_{sim,110} = 34.1° \pm 1.5°$ for (1 1 0).

The W of (1 0 4) and (1 1 0) reflections as a function of c-axis deviations $0° < \omega < 20°$ is shown in Figure 7.7 b). The calculated data presents a linear correlation between the W and ω. The increases of the c-axis deviations results in larger angular widths for both plans (1 0 4) and (1 1 0). From the modelled data analysis it can be extrapolated that $W_{sim,104} = 2.05\ \omega$, for (1 0 4) and $W_{sim,110} = 2\ \omega + 11$, for (1 1 0) for spindles-shaped hematite particles under a magnetic field. The FWHM (W) of both reflections (1 0 4) and (1 1 0) shows similar dependence of ω, $W \approx 2\ \omega$, indicating that both are sensitive to the particles alignment.

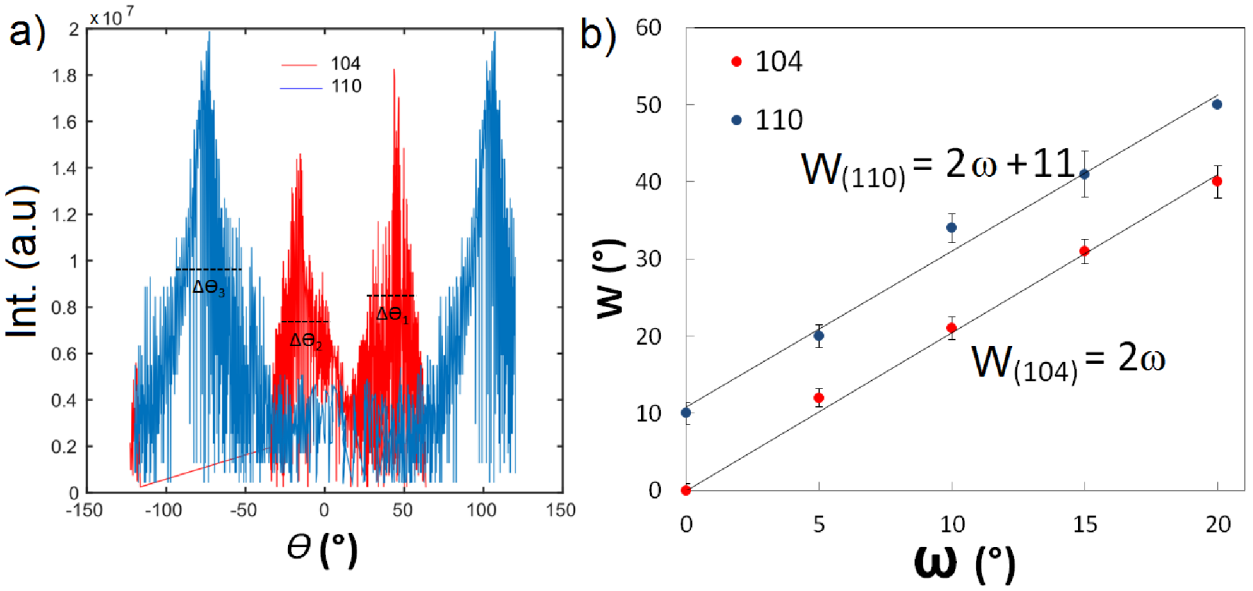

Figure 7.7: Azimuthal cut for (1 0 4) and (1 1 0) reflections. The angular widths, $\Delta\theta_1$, $\Delta\theta_2$ and $\Delta\theta_3$, of the Bragg diffractions correspond to the amplitudes of the diffractions. b) W as a function of imposed c-axis deviations, $0° < \omega < 20°$ for the two reflections (1 0 4) and (1 1 0). Simulated data was linearly fitted resulting in $W_{104} = 2.0\ \omega$ and $W_{110} = 2\ \omega + 11$. The detector properties were modelled with the same geometry as experimental data.

As visible in the Figure 7.7 b) for a particle perfect alignment $\omega = 0$, for reflection (1 0 4) the minimum FWHM obtained is a delta peak δ ("spots"), as observed in Figure 7.6, however, for (1 1 0) reflection the minimum is already W = 11°, indicating the presence of a c-axis deviation of 5.5° at $\omega = 0$.

Employing this calculated equations to the experimental data, it can be concluded that spindle-shaped hematite particles, with an aspect ratio ν = 6.0 under a magnetic field of B =150 mT, rotates not only around the small-axis direction and 360° around the c-axis, but also their particles' c-axis shows an orientation distribution. These c-axis deviations will result in a spindle orientation degree of 12.5°, since the obtained experimental FWHM is $W_{104} = 25°$.

Nack *et al.* [95] studied the nematic order parameter S_2 [108] of spindle-shaped hematite particles with aspect ratio $\nu = 4$ as a function of the flux density of an external magnetic field by SAXS . For a flux density of B = 150 mT the resulting order parameter is expected to be $S_2 \approx -0.4$. Note that $S_2 = -0.5$ indicates that particles are completely aligned perpendicular to the external field. Assuming an equal distribution of the orientation degree of the particle the $S_2 = -0.4$ result in a c-axis deviation around 11°. Thus, this c-axis deviation presented in literature is in line to the one obtained in this work 12.5°. The difference observed can be related to the difference in the particle aspect ratio.

7.3 Spindle shaped particles in Flow

The alignment of anisotropic hematite particles in a flow produced by GDVN will be discussed within this section. The flow direction of the jet is parallel to Jet_y axis, the nozzle tip is located at Jet_y= 0 μm

and the jet centre is at Jet_z= 0 μm.

Two samples of hematite spindles dispersed in water, H2 and H3, were studied in continuos microjets formed by different nozzle diameters and flow rates. The jet diameter was controlled by the nozzle size, the liquid pressure in the nozzle and the gas pressure used to collimate the jet.

Since spindle-shaped hematite particles used in this study were prove to be single crystalline (see chapter 5) is it possible to study their orientation behavior in the microjet by analysing Bragg reflections from the particles crystalline structure.

WAXS patterns at different distances along and perpendicular to the liquid jet flow direction were collected within 2 μm steps across the jet and downstream the nozzle tip allowing to build a map of the particles rheological behavior.

WAXS pattern were corrected for background as well as the polarization as explained in section 7.2.

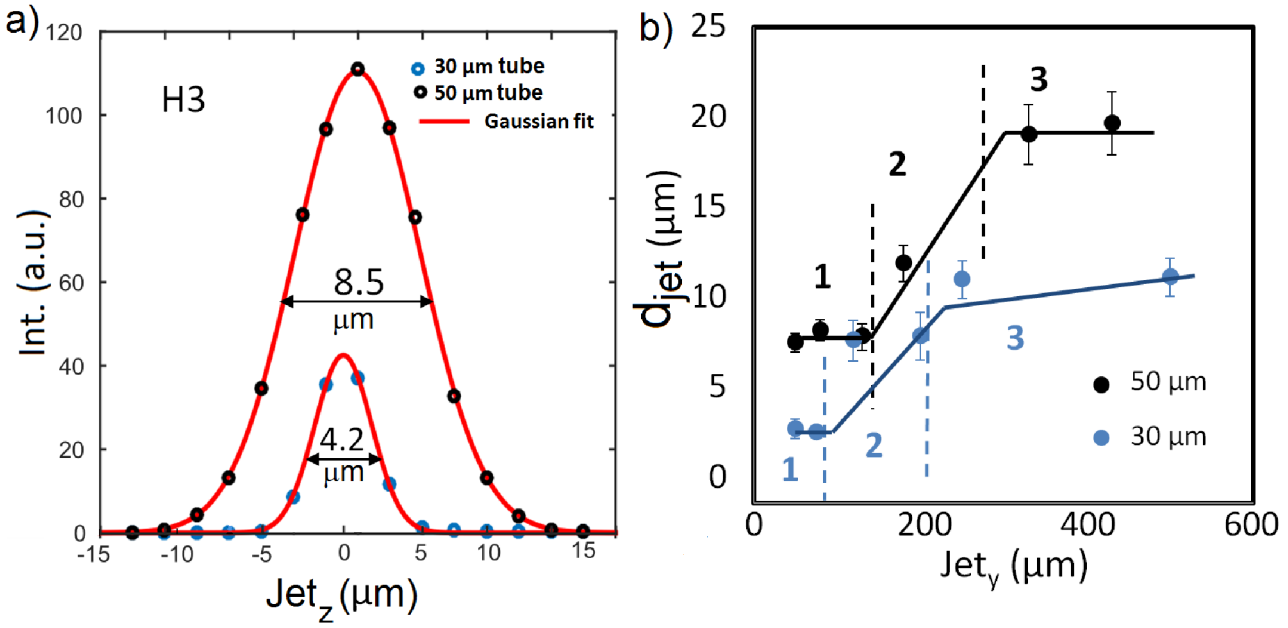

Figure 7.8: a) Sum of total measured scattering intensity across the jet 50 μm downstream the nozzle tip using different micro tube inner diameters during nozzle construction (30 and 50 μm). Experimental data from sample H3 is represented by dots (blue and black) while the red lines are Gaussian fits. The jet diameters obtained from the fits are d_{jet} = 4.17 μm and d_{jet} = 8.54 μm for 30 and 50 μm tubes, respectively. b) Jet diameter as a function of the distance from nozzle tip for the two different inner micro-tube sizes. The numbers (1,2,3) represent the different jet regimes, jet , break-up and droplets regime, respectively, which are limited by the vertical dashed lines.

The jet dimensions can be tuned using different nozzles outlets. The jet diameter d_{jet} was estimated along the jet using nozzles with different outlet diameters and, consequently, different flow rates. Using an outlet diameter of 50 μm allowed for tuning the flow rate to be Q = 40 μl/min while for 30 μm inner-tube-diameter, a flow rate of Q = 20 μl/min was achieved. However, it is known that the nozzle inner-tube diameter has the largest influence on the jet diameter, length and velocity [109]. Since different nozzle outlet diameters leads to different flow rates, both (flow rates and nozzle diameters) will be the parameters taken into account during further analysis together with sample aspect

ratio.

Figure 7.8 a) shows the total scattering intensity (averaged over the pixels) collected across the jet taken at a distance of 50 μm from the nozzle tip. The experimental data points were fitted by a Gaussian function (red line), where the FWHM of the peak is assumed to be proportional to the jet diameter. The obtained jet diameter were, d_{jet} = 4.2 μm $\pm$ 0.8 μm and d_{jet} = 8.5 μm $\pm$ 1.0 μm for 30 μm and 50 μm nozzle diameters, respectively. The estimated values of jet diameter are in a good agreement with jet dimensions (d_{jet} = 3.8 μm and d_{jet} = 8.0 μm for 30 μm and 50 μm nozzle diameters, respectively) observed *in situ* using microscopes and diagnostic devices from the setup, see Figure 7.1.

Figure 7.8 b) shows d_{jet} as a function of different distances from the nozzle tip. It was calculated after deconvolution with the vertical beam shape (2.2 μm) for the two different nozzles diameters. At Jet_y = 120 μm for 30 μm and Jet_y= 180 μm for 50 μm inner-tube-diameter, respectively, the slope changes significantly, suggesting a change in the geometry of the liquid jet, as represented in Figure 7.8 b) with number 1 (jet regime). At this Jet_y distance, the liquid jet breaks up into droplets. The break-up regime is marked in Figure 7.8 b) with number 2 varying between Jet_y = [120 μm - 250 μm] and Jet_y = [180 μm - 330 μm] for 30 μm and 50 μm micro-tube diameters, respectively. After the break-up regime, a different slope in the curve is observed, referred as number 3, indicating the transition to droplets regime, Jet_y = 250 μm and Jet_y = 330 μm, for 30 μm and 50 μm nozzle outlet diameter, respectively. These three regimes were characterized not only using the extracted values from the peak fits but also from the snapshots taken *in situ* during measurements. The different regimes identified in Figure 7.8 b) are presented as well in Figure 7.9 recorded using high magnification microscopes.

As visible in the microscope figures and by the calculated jet diameter downstream the nozzle, the jet regime is characterized by a stable jet at the beginning of the curve corresponding as well to the jet length. The intermediate break-up regime is an unstable region, as observed in Figure 7.9 2) due to the presence of the instabilities which propagates along the jet which favouring the droplets formation. Afterwards the jet diameter reached a maximum and stable value representing the droplets regime.

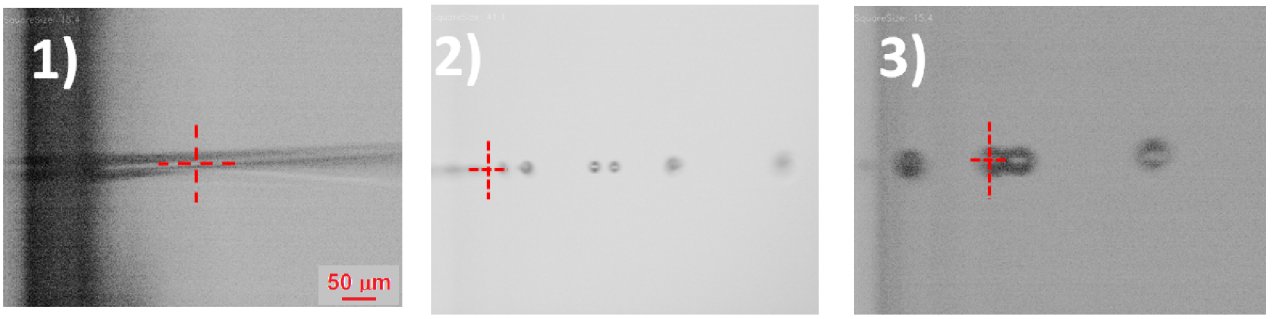

Figure 7.9: Images taken with high magnification microscope *insitu* during the experiment. The numbers 1, 2 and 3 refer to the corresponding regions depicted in Figure 7.8 b). The red cross represents the beam position.

To study the alignment of spindle-shaped hematite particles in a microjet flow the observed Bragg

diffractions along and across the jet will be analysed. To describe the orientation of a single spindle particle the polar angle ω is used as the angle between the spindle major axis and the flow direction, see Figure 7.10. The flow direction in the experiment is defined along the Jet_y direction perpendicular to the beam direction, as shown in Figure 7.10.

As described in the literature anisotropic particles typically align with their long axis parallel to the flow direction. Therefore, perfect alignment of spindles in the flow would result in a $\omega = 0$, with particles major axis parallel to the flow direction (Figure 7.10).

Due to the well known hematite crystalline structure (chapter 5) and the well defined distances between the hematite layers the analysis of particles' orientation via the Bragg diffractions is possible. The azimuthal width $\Delta\theta_q$ of the Bragg diffractions indicates, as referred in section 4.4, an orientation distribution function of the particles within the jet, while the relative position of the peaks, given by the peak azimuthal location μ, reflects the particles' alignment with c-axis parallel to the flow direction. Therefore, the probability of probing spindles with a certain orientation will be analysed in terms of variations of ω .

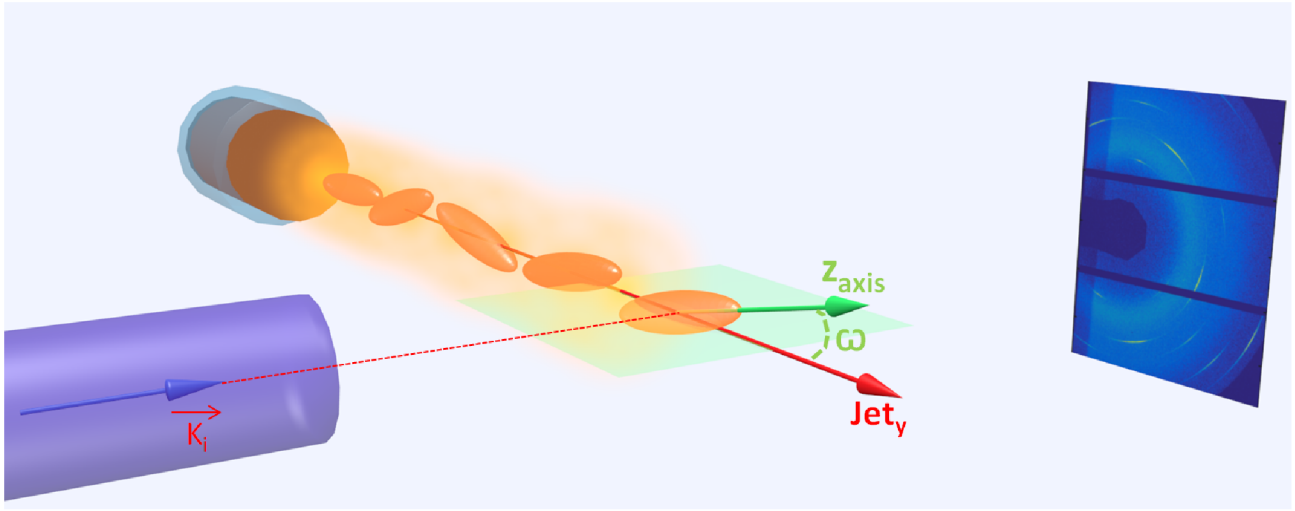

Figure 7.10: Definition of the particle orientation using angle ω.

In the next sections, the analysis of flow alignment of the two different samples, H2 and H3, will be presented.The two most intense Bragg peaks of each sample, which correspond to the reflections (1 0 4) and (1 1 0) will be analysed in terms of the peak positions, μ, and widths, $\Delta\theta_q$. Afterwards a comparison with a computational study and with the reference data taken from static measurements will be shown to understand how the flow rate and particles aspect ratio influence the alignment of anisotropic particles in flow.

Sample H3

Figure 7.11 a) and b) show diffraction patterns measured at 75 μm (jet regime) and 300 μm (droplets regime) away from the nozzle tip, respectively, both at the centre of the microjet, ($Jet_z = 0$). This microjet was formed by a GDVN with 30 μm diameter and Q = 20 μl / min.

In the jet regime (Figure 7.11 a)) the azimuthal location of the Bragg reflections on the detector can

be allocated to the different Miller indices which are characteristics for the hematite crystal structure. The presence of incomplete Debye-Scherrer rings indicate that the crystalline structure of hematite particles have a preferred orientation at this position of the liquid microjet.

The modelled data showed that a spindle orientation with the long axis parallel to the flow direction leads to four reflection peaks at q_{104}. However, in the experimental diffraction pattern shown in Figure 7.11 a), only one broad peak is obtained instead of the two expected ones at the positive q_{x}. This broad peak can be understood as an overlapping of the two expected reflections for (1 0 4) since the modelled data shows that this two reflections distances around 60°, which is comparable with the azimuthal width obtained for the reflection $\Delta\theta_1$. The reflections at the negative q_{x} are not visible due to the limited q range obtained in the experiment. For q_{110} from the two expected reflections only one is completely visible since the second reflection is partially covered by the detector.

In the scattering pattern taken at the droplet regime, $\mathrm{Jet_y} \geq 300$ μm (Figure 7.11 b), complete Debye-Scherrer rings are obtained for both reflections (1 0 4) and (1 1 0), indicating that particles do not show a preferred orientation in the droplet regime.

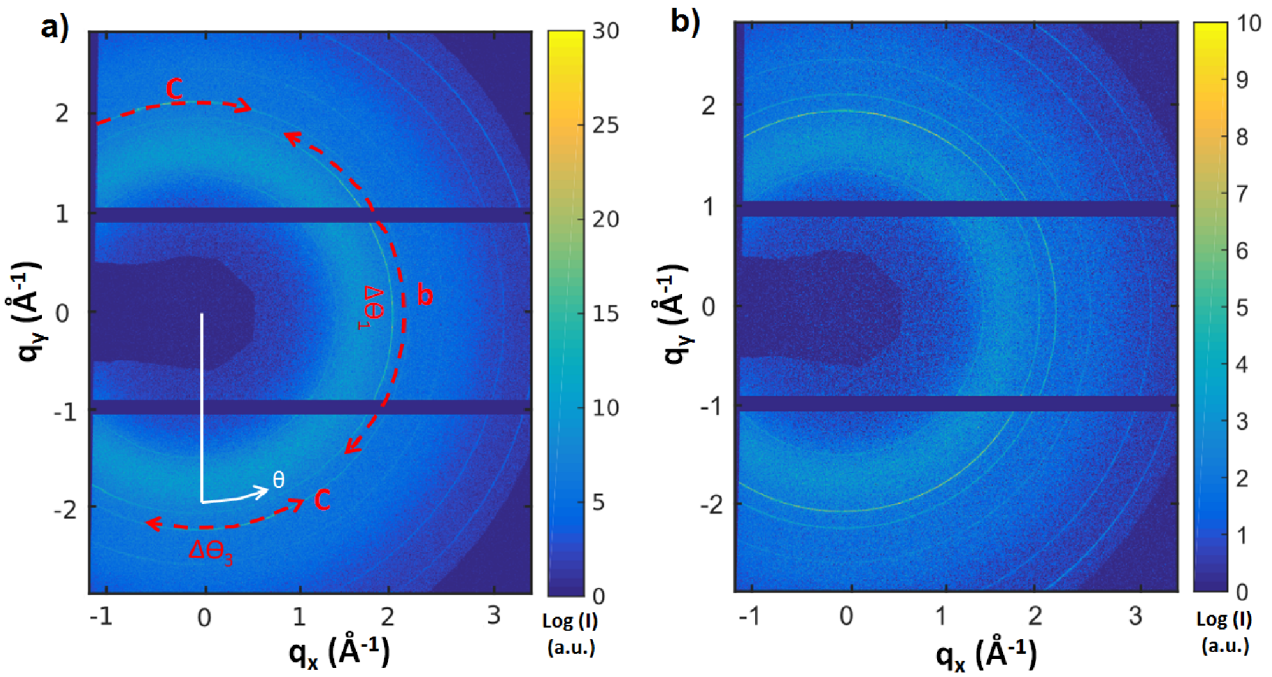

Figure 7.11: Diffractograms of H3 ($\nu = 2.7$) hematite spindles in a flow resulting from the average of 100 patterns measured at a) $\mathrm{Jet_y}$ = 75 μm and $\mathrm{Jet_z}$ = 0, jet regime. b and c represents the reflections (1 0 4) and (1 1 0) respectively. The red dashed lines mark the azimuthal width of each plane (θ_1, θ_3). b) $\mathrm{Jet_y}$ = 300 μm and $\mathrm{Jet_z}$ = 0 μm, droplets regime.

The azimuthal widths $\Delta\theta_1$ and $\Delta\theta_3$ and azimuthal positions μ of the Bragg peaks shown in Figure 7.11 a) were extracted for the (1 0 4) and (1 1 0) reflections. The data were fitted by Gaussian functions using equation 7.3 and shown in Figure 7.12 a). $\Delta\theta_1$ shows the overlapping of the two expected reflections for (1 0 4). Although two Gaussian functions were used to fit the overlapped peaks differing only 60° between them but result was not conclusive, see Figure 7.12. Thus, the fit of only one broad diffraction is presented.

The $\Delta\theta_1$ and $\Delta\theta_3$ of the reflections (1 0 4) and (1 1 0), respectively, taken at the droplets regime from Figure 7.11 b) are shown in Figure 7.12 b). It is difficult to obtain a fit of the resulting data (full rings) indicating that at this distance from the nozzle tip the orientation of the particles is random.

The W of the (1 0 4) Bragg diffractions are shown in Figure 7.13 as a function of Jet_y for the two nozzle diameters. The azimuthal widths extracted from the Bragg diffractions at $q = 2.32$ Å^{-1} (1 0 4) along the jet are similar, thus independent of the nozzle diameter (Figure 7.13). The jet regime, (1) is represented by stable values of the W which increases to a maximum in the droplets regime (3), an intermediate region is defined as the break-up regime (2). The same behavior is observed for both nozzle diameters.

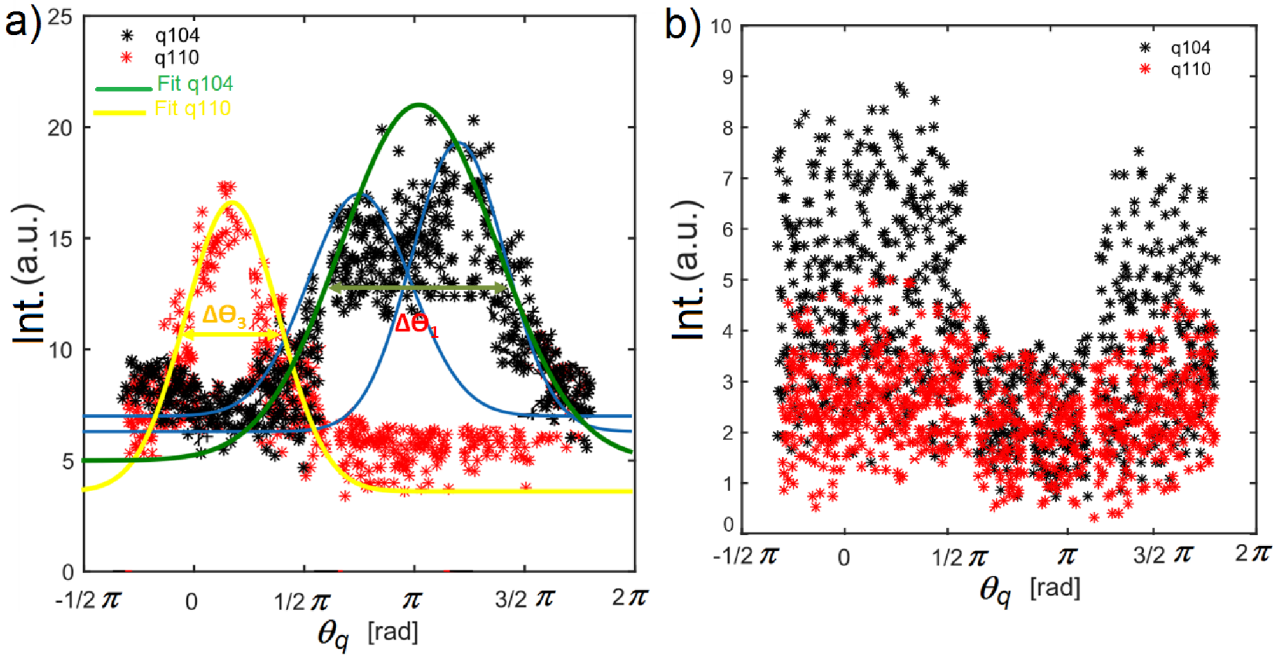

Figure 7.12: a) $I(\theta)$ shown in Figure 7.11 a) from b and c Bragg reflections corresponding to (1 0 4) (black stars) and (1 1 0) (red stars), respectively, with the respective Gaussian fit. b) $I(\theta)$ of the diffractogram showed in Figure 7.11 b) at $\text{Jet}_\text{y} = 300$ μm, break-up regime for the reflections (1 0 4) (black stars) and for (1 1 0) (red stars).

Due to the peak overlapping the differences expected are less pronounced. Therefore the reflection (110) will be analysed in more detail.

Tables 7.1 and 7.2 shows the results of the fits (μ and W) for 30 μm and 50 μm nozzle diameter, respectively. These results are given for the two reflections (1 0 4) and (1 1 0) as a function of the distance to the nozzle tip Jet_y however only (1 1 0) will be analysed in more detail due to the overlap of two reflections observed for (1 0 4).

The data shows that W_{110} in the jet regime is constant as a function of the nozzle tip increasing in the break up regime. This behavior indicates that particles are more aligned in the jet regime than in the break-up regime. After the break-up it is impossible to fit the angular dependence of the rings indicating that particles are randomly oriented.

Increasing the nozzle diameter to $d_{nozzle} = 50$ μm the behaviour of W_{110} is the same when compared to a nozzle diameter of $d_{nozzle} = 30$ μm. However, higher values are obtained indicating lower

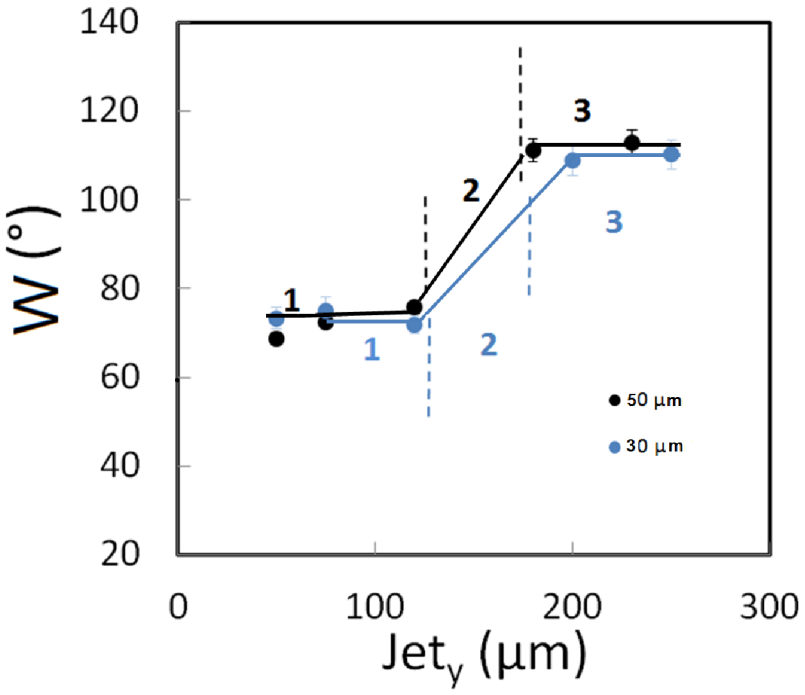

Figure 7.13: FWHM of the Bragg reflection q_{104} as a function of distance from the nozzle tip (Jet$_y$) for the two flow rates (20 μl/min and 40 μl/min). The different jet regimes are marked with numbers 1, 2 and 3 representing the jet, break-up and droplets regime, respectively.

degree of particles orientation. This is explained by the change of nozzle diameter and consequently different flow rates. At the same time, different flow properties are present, such as lower shear rates. The shear rate ratio in the microtube for the two nozzle diameters can be calculated as:

$$\kappa = \dot{\gamma}_1/\dot{\gamma}_2 = (8V_{pipe1}/d_{pipe1})/(8V_{pipe2}/d_{pipe2}) \tag{7.4}$$
$$= (V_{pipe1}/d_{pipe1})/(V_{pipe2}/d_{pipe2}) = \frac{V_{pipe1} \cdot d_{pipe2}}{V_{pipe2} \cdot d_{pipe1}}.$$

Therein V_{pipe1} =0.47 m/s the jet velocity in the pipe with a diameter 30 μm flowing at Q = 20 μl/min and V_{pipe2} =0.34 m /s the jet velocity in the pipe with diameter 50 μm flowing at Q = 40 μl/min. This results in a shear ratio of $\kappa = 2.30$. Note that this values represents the shear ratio in the microtube and not at the nozzle tip, where the jet collimation occurs. The shear at this nozzle position is difficult to determine even by simulation studies since the GDVN are "hand-made" produced (see section 6.2.1), since the jet collimation is always different for each nozzle.

Thus the increase of nozzle diameter leads to lower shear rates and consequently a decrease of particles alignment along the jet regime as observed from the difference of W$_{110}$ at $d_{\mathrm{nozzle}} = 30$ μm and W$_{110}$ at $d_{\mathrm{nozzle}} = 50$ μm.

The azimuthal peak position, which is given by the get geometry, shows a stable range along the jet regime varying its position in the break-up regime, where the jet changes its geometry.

As an intermediate conclusion, sample H3 ($\nu = 2.7$) shows alignment along the jet which decreases as a function of the nozzle tip. In the droplets regime, no particle orientation was observed.

Table 7.1: Results of Gaussian fits as a function of Jet_y, a flow rate of, Q = 20 μl / min. The * mark the overlapped peaks.

(a) q = 2.32 Å^{-1} (q_{104})

Jet_y (μm)	μ (°)	W (°)
50	108.2 ± 1	44.3 ± 2
75	106.9 ± 0.5	75.1 *± 3
120	107.7 ± 0.3	74.8 *± 2
200	104.5 ± 1	109.1 ± 4

(b) q = 2.49 Å^{-1} (q_{110})

Jet_y (μm)	μ (°)	W (°)
50	12.2 ± 0.5	39.0 ± 0.5
75	15.3 ± 1	39.3 ± 1
120	24.1 ± 1	39.4 ± 1
200	21.1 ± 1	67.7 ± 1

Table 7.2: Results of Gaussian fits as a function of Jet_y, using a 50 μm nozzle diameter and a flow rate of, Q = 40 μl / min.

(a) q = 2.32 Å^{-1} (q_{104})

Jet_y (μm)	μ (°)	W (°)
50	94.9 ± 1	68.7 ± 1
75	94.9 ± 1	72.6 ± 1
120	93.2 ± 1	75.8 ± 1
200	25.6 ± 2	111.1 ± 3

(b) q = 2.49 Å^{-1} (q_{110})

Jet_y (μm)	μ (°)	W (°)
50	7.3 ± 1	44.0 ± 1
75	7.1 ± 1	43.6 ± 1
120	8.2 ± 1	44.7 ± 2
200	30.7 ± 3	64.0 ± 5

The degree of orientation is higher for low nozzles diameters which results in higher jet velocities and higher shear rates. High values of shear rate leads to small diffraction widths (W) and consequently higher degree of particle alignment.

To quantify this degree of particle orientation a model study will be presented at the end of the chapter.

Sample H2

In this section an analogue analysis is presented for hematite sample H2 with a different aspect ratio, $\nu = 6$. As in the section above, the total scattering intensity is studied as a function of jet_y at $\text{jet}_\text{z} = 0$ for two different flow rates of Q = 25 μl/min and Q = 50 μl/min using the same nozzle diameter ($d_{\text{nozzle}} = 50$ μm) see Figure 7.14.

As for sample H3 (Figure 7.8) the jet diameter is stable in the jet regime (1), approximately $\text{d}_\text{jet} = 4$ μm and $\text{d}_\text{jet} = 6$ μm for Q = 25 μl/min and Q = 50 μl/min respectively. After an increase of the jet diameter at the jet break-up (2), the jet reach their maximum indicating a change for the jet geometry to the droplets regime (3). The droplets diameter obtained follows the predicted droplet diameter from the literature for Rayleigh nozzles, see equation 2.16.

Figure 7.15 a) shows the intense Bragg reflections from the hematite crystal structure at $q = 2.32$ Å^{-1} (q_{104}) (b) and at $q = 2.49$ Å^{-1} (q_{110}) (c) in the jet regime. The presence of the reflection (0 0 6) indicates a preferable orientation of the particles at $\text{Jet}_\text{y} = 75$ μm.

Similar to sample H3, at $\text{Jet}_\text{y} = 350$ μm, complete Debye Scherrer rings are visible representing the break-up regime, as visible from Figure 7.16 taken with high magnification microscopes during the measurement. The azimuthal widths of the scattering profiles were extracted for q_{104} and q_{110} in

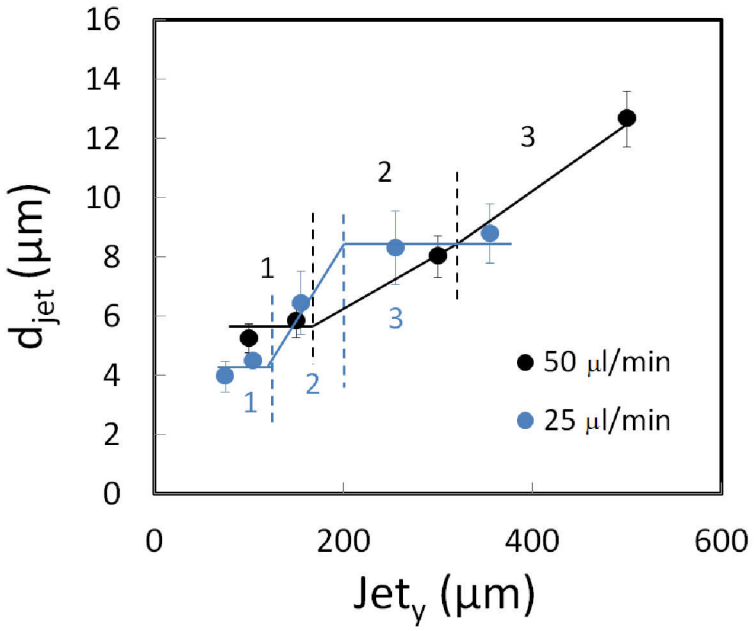

Figure 7.14: Jet diameter from sample H2 ($\nu = 6$) as a function of the distance from nozzle tip after deconvolution with the vertical beam shape, for two different flow rates of 25 μl/min and 50 μl/min, respectively and using a nozzle diameter of $d_{nozzle} = 50$ μm. The numbers 1, 2 and 3 represents the jet, break-up and droplets regimes, respectively.

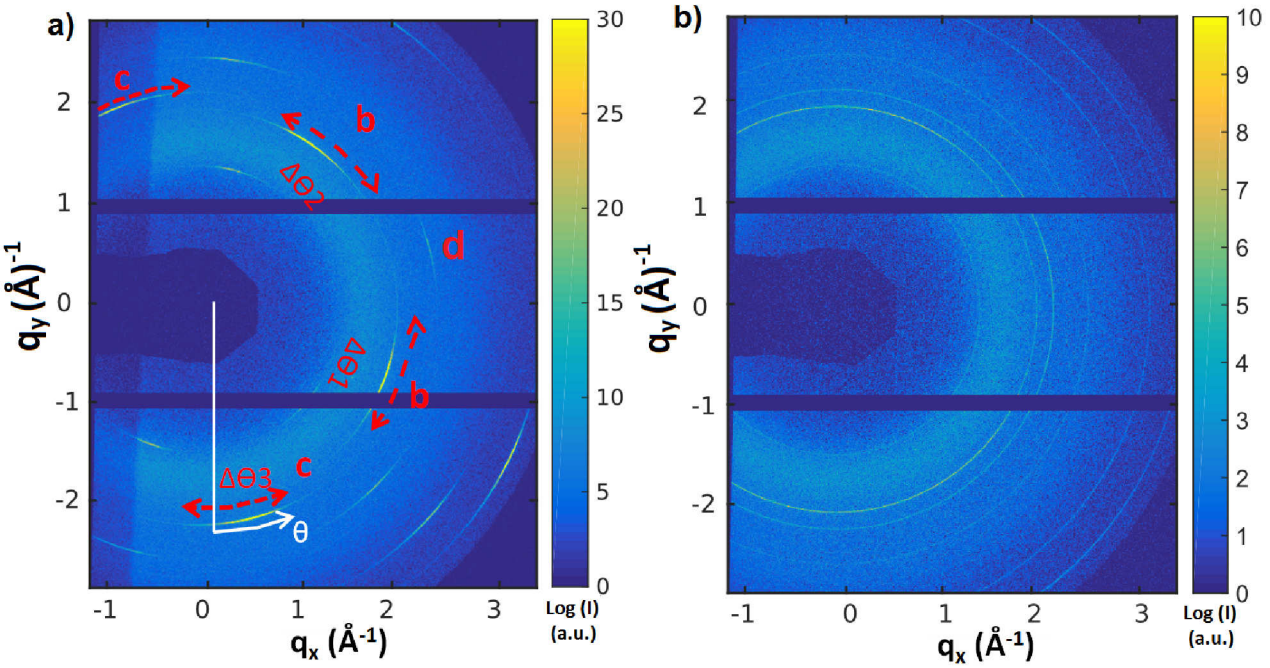

Figure 7.15: Diffractograms of sample H2 ($\nu = 6$) resulting from the average of 100 patterns measured at a) $Jet_y = 75$ μm and $Jet_z = 0$ μm, jet regime. b, c and d represents the reflections (1 0 4) (1 1 0) and (0 0 6), respectively. The red dashed lines mark the azimuthal width of each plane (θ_1, θ_3). b) Jet_y = 350 μm and Jet_z = 0 μm, break-up regime, produced by a nozzle with 50 μm diameter and Q = 25 μl/min.

the jet and droplets regimes, Figure 7.17 a) and b).

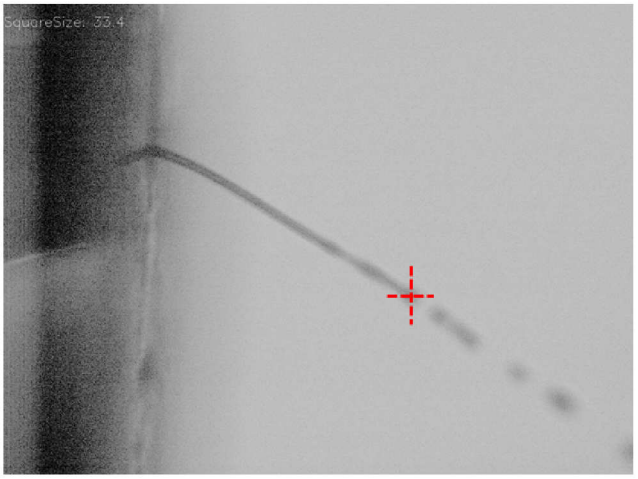

Figure 7.16: High magnification microscope image taken during the experiment. The red cross represents the beam position at $\text{Jet}_\text{y} = 350$ μm.

In the jet regime, $\text{Jet}_\text{y} = 75$ μm, Figure 7.17 a) the Bragg reflections are narrower when compared with the azimuthal widths extracted from sample H3. This indicates that sample H2 presents a high degree of particles alignment along the jet regime.

Since this jet was tilted, a study across the jet geometry was performed, to analyse the effect of an inclined jet on the azimuthal peaks widths and the reflections' positions. The azimuthal width and the

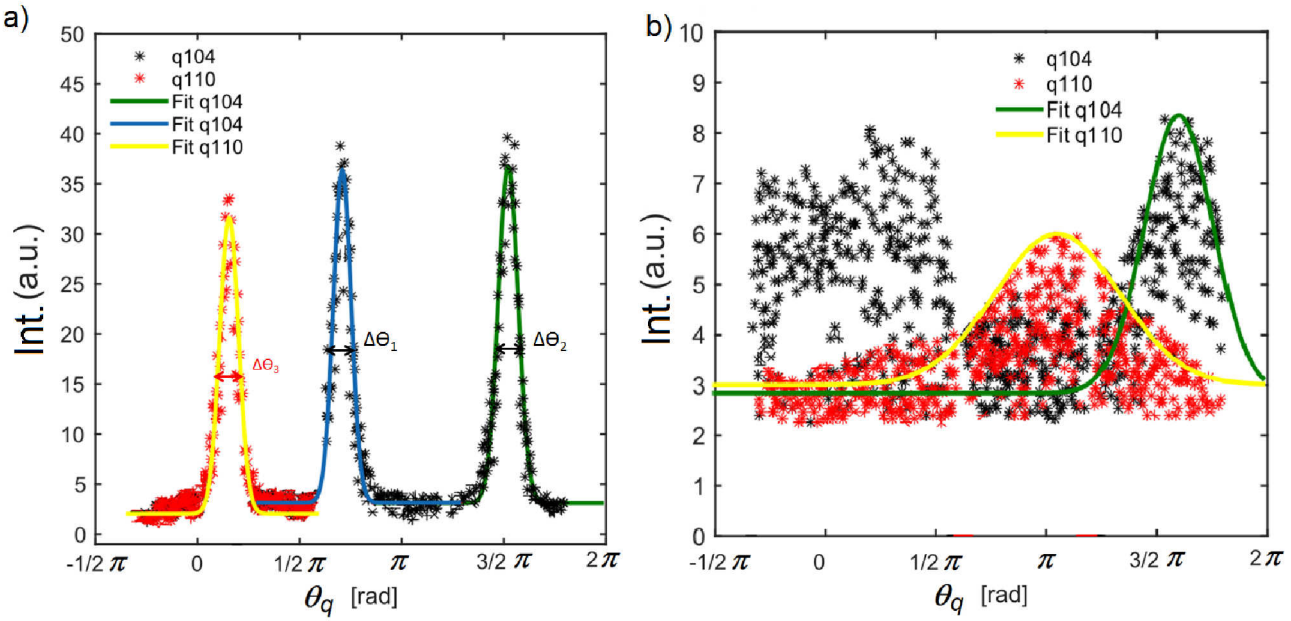

Figure 7.17: a) Azimuthal cut, $\text{Jet}_\text{y} = 75$ μm, of the diffractogram shown in Figure 7.15 a) of (1 0 4) and (1 1 0) Bragg reflections with the respective Gaussian fit. b) I_θ of the diffractogram at $\text{Jet}_y = 350$ μm shown in Figure 7.15 b).

peak position were extracted across the jet at 80 μm downstream the nozzle tip. The peak position μ and the averaged values of the azimuthal width of the Bragg diffractions (1 0 4) and (1 1 0) are shown in Figure 7.18.

The peak position presents the same behavior for both (1 0 4) and (1 1 0) reflections with a small decrease close to the jet centre which indicates the higher inclination of the jet the transition to the bottom edge of the jet. Note that the peak position at this distance from the nozzle tip and at the jet centre is different from the one presented in table 7.3 a) because Figure 7.18 a) refers to the position of first reflection.

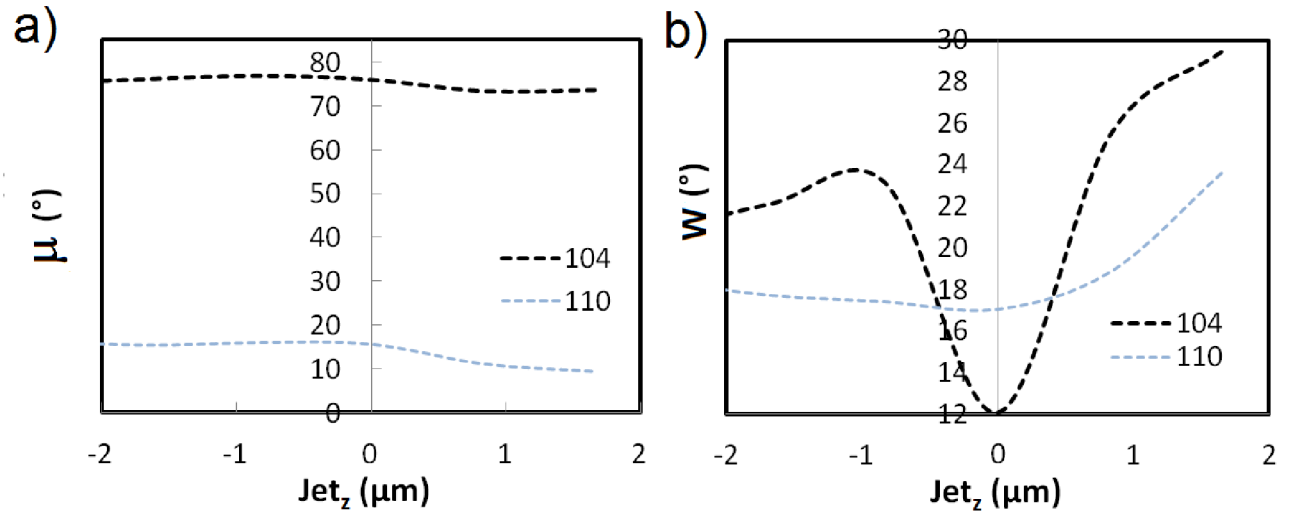

Figure 7.18: a) Relative peak position and b) FWHM of planes (1 0 4) and (1 1 0) taken across the jet -2 < Jet$_z$ < 2 μm at 80 μm downstream the nozzle tip using a Q = 25 μl / min.

The average of the peak widths across the jet differs between the two reflections studied. Reflection (1 0 4) presents a mirrored behavior, where at Jet$_z$ = 0 μm a minimum value of W indicates a higher degree of orientation at the centre of the jet rather at the edges. Note that at Jet$_z$ > 0 μm W increases more compared to Jet$_z$ < 0 μm. This is because of the jet inclination, positive Jet$_z$ represents the bottom edge of the jet. The behavior of the azimuthal widths of the (1 1 0) reflection across the jet is relatively constant until the jet centre increasing after that until the jet edge. The expected mirrored behaviour is replaced by an increasing behaviour, due to the jet inclination since its more pronounced at Jet$_z$ > 0 μm. Thus, a jet inclination leads to a different flow behavior across the jet. At Jet$_z$ < 0 μm lower values of W indicates a higher degree of particles orientation while in the other jet edge the particles' alignment decreases.

At larger distances from the nozzle tip (Jet$_y$ $\geq$ 350 μm) the diffraction maxima become complete, indicating the droplets regime, Figure 7.17 b). Complete Debye Scherrer rings are present at this distance from the nozzle tip (Figure 7.15 b)), corroborates with the jet region defined. The same results were obtained from sample H3 at droplets regime.

W is shown in Figure 7.19 for the reflection (1 0 4) for the two different flow rates Q = 25 μl/min and Q = 50 μl/min. The stable values along the jet regime increase towards a plateau, indicating a new state of the jet, which is the droplets formation. The difference observed in the jet regime (1) is explained by the increase of the flow rates suggesting a different flow behaviour and consequently lower degree of particles orientation when the flow rate increases.

The angular widths as a function of Jet$_y$ for H2 sample (Figure 7.19) shows smaller W when compared to sample H3 (Figure 7.13). This indicates a narrower distribution of orientation for more

elongated particles at the jet central axis. A more detailed analysis is presented below.

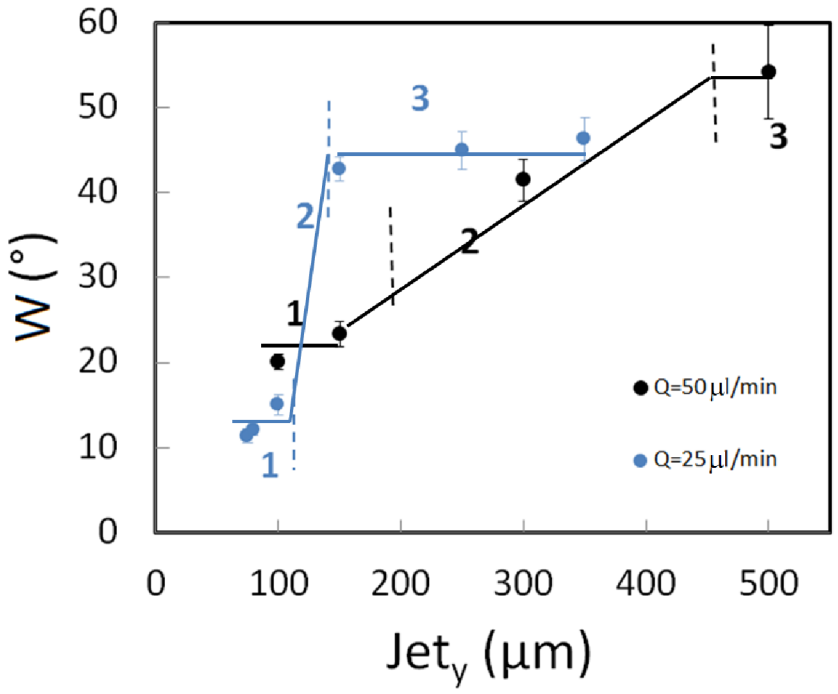

Figure 7.19: Gaussian fitted azimuthal width FWHM of the Bragg reflection q_{104} as a function of distance from the nozzle tip (Jet$_y$) for two different flow rates, Q = 25 μl/min and Q = 50 μl/min.

W of the Bragg reflections is shown as well in the table 7.3 for both (1 0 4) and (1 1 0) reflections where a similar behavior is observed for sample H3, i.e. an increase of W as a function of the nozzle tip distance.

Comparing both samples at low flow rates (table 7.3 and table 7.1) it is visible that the degree of alignment of sample H2 is higher compared with sample H3 since $W_{H3(110)} > W_{H2(110)}$. The calculated speed of sample H3 is similar to the one calculated for sample H2 in the microtube ($V_{jetH2} = 0.43$ m/s $\approx V_{jetH3} = 0.47$ m/s), thus the shear rates in microtube are in the same magnitude. Therefore, differences of spindle alignmnet are attributed to the different aspect ratio.

The peak position shows constant values, within the error bars, for both reflections in the jet region, varying in the break-up regime due to the change in jet geometry. This leads as well to a higher increase of the peak azimuthal width, since the droplets formation favour the rotation of particles decreasing the degree of alignment.

The fit results for peak position and azimuthal width of the peak using higher flow rate (Q = 50 μl/min) of sample H2 are as well shown in table 7.4 for both crystallines planes (1 0 4) and (1 1 0). The behaviour of the azimuthal width of the peak for both reflections follows the trend observed for sample H3 and for sample H2 at low flow rates, i.e. it increases along the jet, being more pronounced at the break-up regime. The peak position follows the same behavior observed in sample H3, with a change of the position when the break-up regime starts for Jet$_y > 150$ μm.

The differences between the two different flow rates in sample H2 can be compared taken into account the jet speed in the microtubes since the diameter of the microtube used was the same for

Table 7.3: Results of Gaussian fits as a function of Jet_y, using a 50 μm nozzle diameter and a flow rate of, Q = 25 μl/min at a $Jet_z = 0$ μm.

(a) $q = 2.32$ Å^{-1} (q_{104})

Jet_y (μm)	μ (°)	W (°)
75	147.7 ± 1	11.34 ± 0.8
80	148.3 ± 1	12.08 ± 0.6
100	148.3 ± 1	14.98 ± 1.2
150	160.1 ± 1	42.74 ± 1.4

(b) $q = 2.49$ Å^{-1} (q_{110})

Jet_y (μm)	μ (°)	W (°)
75	11.3 ± 0.2	16.7 ± 0.2
80	14.6 ± 0.2	17.1 ± 0.4
100	15.3 ± 0.6	19.9 ± 1
150	18.1 ± 3.0	34.4 ± 4

Table 7.4: Results of Gaussian fits as a function of Jet_y, using a flow rate of Q = 50 μl/min for (1 0 4) and (1 1 0) miller indices at a $Jet_z = 0$ μm.

(a) $q = 2.32$ Å^{-1} (q_{104})

Jet_y (μm)	μ(°)	W (°)
100	151.0 ± 0.5	20.1 ± 1
150	150.2 ± 1	23.4 ± 2
300	149.2 ± 2	41.4 ± 3

(b) $q = 2.49$ Å^{-1} (q_{110})

Jet_y (μm)	μ(°)	W (°)
100	11.3 ± 0.4	17.6 ± 0.6
150	11.6 ± 0.5	18.6 ± 1
300	10.9 ± 1.5	40.3 ± 2

both measurements. Flow speeds of in $V_{pipe1} = 0.21$ m/s and $V_{pipe2} = 0.43$ m/s for Q = 25 μl/min and Q = 50 μl/min are obtained.

Higher jet velocities lead to higher shear rates and thus lower values of W which indicates higher degree of particles alignment, as observed with sample H3. However the observed increase in jet speed in the tube for particles with high flow rates is reflected to lower degree of particles alignment (1 0 4). The reflection (1 1 0) seems not to be influenced by this change. Unfortunately, both studied sample systems can be hardly compared, even only qualitatively, since the jet dimensions in both flow rates are completely different. Additionally, the data was measured at different distances along the jet, what can change the flow behavior.

In conclusion, it is observed that particles with higher aspect ratio leads to a more pronounced alignment indicated by the lower widths of the peaks obtained along the jet. When the flow rate or nozzle diameter increases different flow properties are achieved. In these cases, the jet speed and the shear rate ratio on the microtube can be determined. Higher jet speeds on the microtube lead to higher shear rates which results in a higher degree or particle orientation.

The quantification of the degree of particle orientation in flow will be analysed by a computational study, modelling the scattering patterns as a function of the behaviour of spindle shaped particles' along the flow. In the next section a model study similar to the one presented for the static measurements will be discussed.

Since orientation of the particles along the jet was detected, the reduction of alignment in the jet can be studied by the comparison of the particles rotational coefficient to the particles rotational diffusion, to understand if the behaviour of the spindles along the jet is dominated by flow or by diffusion.

Assuming only Brownian diffusion in a dilute dispersion of anisotropic particles, the particles diffusional rotation can be calculated using equation 7.1 as $D_r \approx 50$ rad^2/s for sample H2.

Additionally, the particles rotational coefficient can be extracted by:

$$\sigma^2 = 2D \cdot t + c \tag{7.5}$$

whit the offset

$$c = -2D\tau_0 \tag{7.6}$$

where σ^2 is the width of the peaks extracted from the Gaussian fit, D is the particles rotation coefficient, t the time calculated via $V_{jet} = dr/dt$, with dr the distance measured from the nozzle tip and c is a correction for the t axis expressing the effective nozzle exit. D was obtained by the slope of a linear correlation between σ^2 and t, as presented in Figure 7.20, which results in a value of D $= 6 \times 10^4$ rad$^2/s$ and $\tau_0 = 4$ μs. From $\tau_0 = 4$ μs one can obtain the effective nozzle exit R_0 using

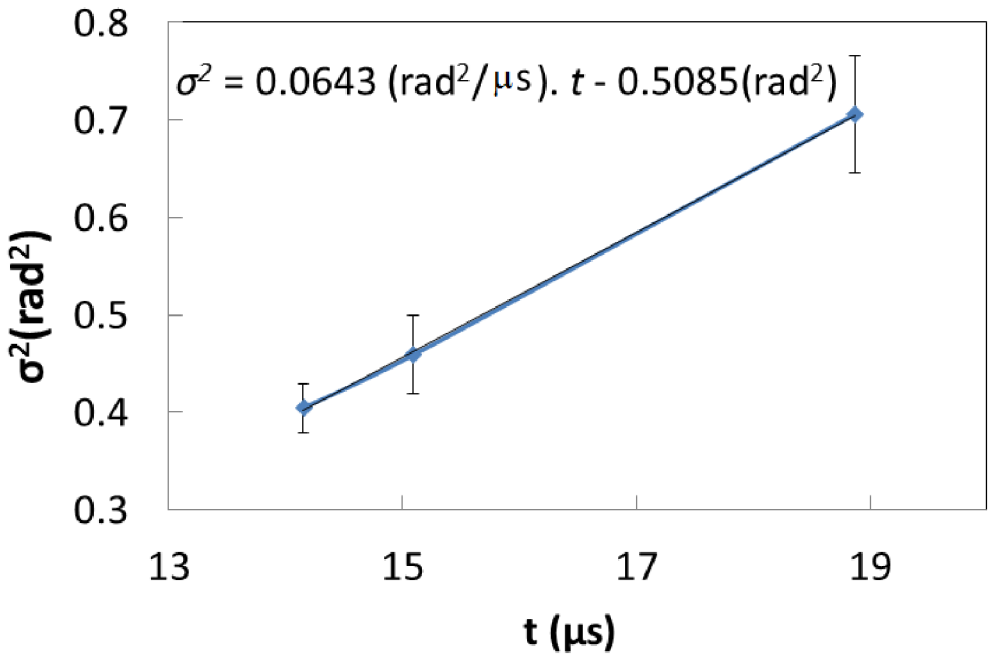

Figure 7.20: Rotational coefficient calculation of Spindle-shaped particles, sample H2, travelling with a flow rate of Q = 25 μl/min and in a jet diameter of 10 μm.

the $V_{jet} = 5$ m/s a value of $R_0 = 20$ μm is found ($R_0 = V_{jet} \cdot \tau_0$). At this point the particles are still perfectly aligned by the focusing gas which exits the nozzle tip. Thus, one can conclude that with this particle system and flow rate until 20 μm downstream the nozzle tip the shear magnitude is still high and after that shear cessation sets in.

Comparing these rotation coefficients, the mean-square angular deviation is about 3 orders of magnitude larger than the rotation of single particles assuming classical Brownian motion. This indicates that the loss of alignment is higher than expected for thermal rotational diffusion and the particles alignment in the jet is still dominated by the flow and shear cessation.

Model study

A computational study of the spindle-shaped hematite particles' behavior in the flow will be shown in this section to model the particles' orientation degree observed in experimental data. WAXS scattering patterns will be modelled and the analysis will follows the experimental analysis steps.

The geometry of the modelled experiment is presented in Figure 7.21. To compute the spindle-shaped particle behavior in the jet it was assumed that particles has a preferable orientation with c-axis parallel to the flow direction and particle c-axis can still rotate 360°. Note that particles under an external magnetic field could still rotate around the small-axis, but this movement is not allowed in the jet. As observed for particles under an external magnetic field, possible c-axis deviations ω are assumed as well in the jet, to be able to model the experimental data. These possible c-axis deviations are depicted in the Figure by the grey coordinated net. Assuming perfect alignment in the flow with the c-axis perpendicular to the flow direction, the resulting scattering pattern, shown in Figure 7.6, does not follow the experimental data. Therefore, additional deviations of c-axis were studied, as in the static measurements, in order to be able to model the experimental data.

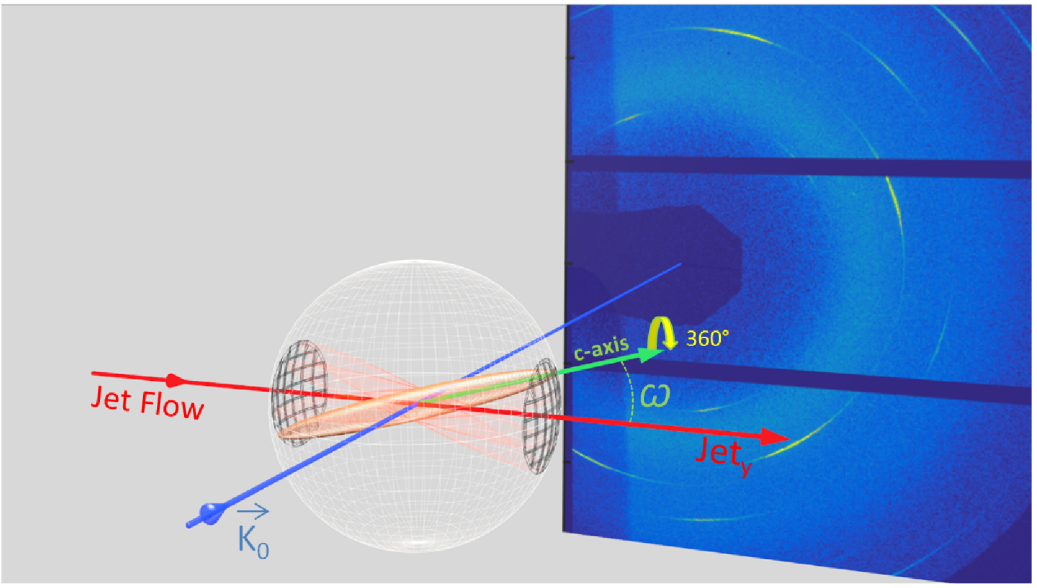

Figure 7.21: Geometry of the simulated experiment in WAXS geometry of spindle hematite particles oriented by the flow. The simulated deviations of the c-axis are shown by the grey coordinated net, where the maximum deviation was set to $\omega = 20°$ and the minimum $\omega = 0°$.

WAXS patterns were modelled assuming different c-axis deviations $0° < \omega < 20°$. The resulting simulated WAXS patterns were analysed via the W for (1 0 4) and (1 1 0) reflections as a function of the c-axis deviation angles, ω, similar to experimental data. Contrary to the experimental data, which was fitted by a Gaussian model to extract the FWHM, in the simulation study was assumed that every different positions acquired along the jet has equal probability. Thus, the model data is interpolated and the FWHM (W) is measured at the half hight of the each reflection, and averaged afterwards. An example of the azimuthal cut, I_θ is shown in Figure 7.22 a) with $\omega = 12.5\ °$.

The obtained W as a function of the c-axis deviation ω are shown in Figure 7.22 b) for (1 0 4) and (1 1 0) reflections.

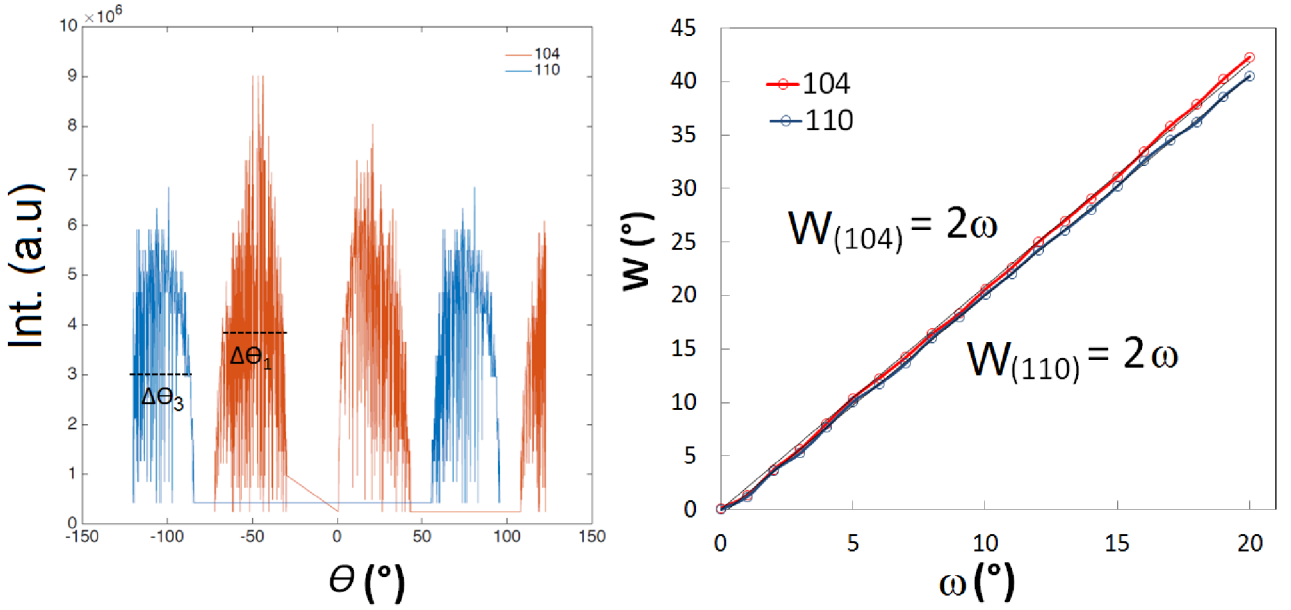

Figure 7.22: Azimuthal cut of the planes (1 0 4) and (1 1 0) assuming a c-axis deviation of ω = 12.5 °. b) Computed azimuthal widths for the two planes in analyses (1 0 4) (1 10) as a function of imposed c-axis deviations, 0 < ω <20. Modelled data for the two reflections was linearly fitted resulting for both reflections W= 2.0 ω.

Figure 7.22 b) shows a linear correlation between W calculated and the imposed c-axis rotation for the planes (1 0 4) and (1 1 0). Higher c-axis deviations lead to larger angular widths. The calculated W for both reflections show similar behaviour, allowing both to be fitted with the same linear trendline, which can be described by W = 2.0 ω. This expression, based on the model data, can be employed to quantify the degree of particle orientation obtained experimentally. Thus, particles with higher aspect ratio (sample H2, ν = 6) flowing at Q = 25 μl/min shows a degree of rotation from 5° to 7.5° along the jet regime from 75 μm to 100 μm downstream the nozzle tip. These degree of orientation increases with the increase of flow rate to Q = 50 μl/min from 10° to 12° when measured from 100 μm to 150 μm from the nozzle tip. Analysing the behavior of the particles with smaller aspect ratio (sample H3, ν = 2.7), the orientation degree of particles increases when compared to sample H2, as discussed above. These particles shows a c-axis deviation of about 22° at 50 μm from the nozzle tip when flowing at Q = 25 μl/min which increases to 35° at a Q = 40 μl/min.

7.4 Discussion and conclusion

WAXS patterns show a pronounced alignment of dispersed single-crystalline hematite particles in the flow direction. Their orientation profile was analysed from the nozzle to the droplets regime. Furthermore, it was determined how the aspect ratio and the flow rates influence the behaviour of particles along the jet.

It is commonly assumed that anisotropic particles align parallel to the flow direction [74, 110, 111]. The data presented in this chapter for spindle-shaped hematite particles shows as well this expected behavior as extracted from the Debye Scherrer rings. The hematite particle's alignment with

their long axis parallel to the flow direction results from the mechanism of jet collimation [112].

The jet formation mechanism is illustrated in detail in Figure 7.23 by using a GDVN and assuming an incompressible Newtonian fluid. Furthermore the different regimes produced of the GDVN are shown and described in the following :

1. Poiseuille flow - A laminar flow is assumed in the microtube. The calculated shear rates are around $\dot{\gamma} = 10^4\ \mathrm{s}^{-1} - 10^5\ \mathrm{s}^{-1}$ supporting an orientation of the particles parallel the flow direction [74, 111].

2. Compressional flow - A compressional flow is created due to the viscous shear forces from a gas flow which surrounds the liquid jet [112]. Thus, high shear rates are therefore expected [112, 113].

   Due to the jet collimation filaments were created in the liquid jet and the incompressible liquid is stretched out along the central flow axis, causing particle alignment in the direction of the central axis of the flow [112]. Because of the high shear rate the speed of the jet which exits the nozzle will be faster further away from the central axis and the extended filaments within such a velocity profile will experience a torque which results in an alignment of the particles along the flow direction [74, 112].

3. Extensional flow - Extensional flow is characterized by the initial alignment of the particles along the central axis of the jet [74, 112]. Upon exiting the nozzle tip the liquid will be stretched due to the shear cessation downstream of the nozzle tip [110, 112].

The experimental data shows that particles' c-axis deviates from a perfect alignment (c-axis parallel to the flow direction) in the flow. This behavior was quantified by modelling the experimental data along the jet. For particles with an aspect ratio of $\nu = 6$ and flowing with Q = 25 μl/min, the degree of orientation varies from $\omega = 5°$ to $\omega = 7.5°$.

Experimental data collected downstream the nozzle tip show that alignment of particles gets slightly reduced along the jet (Figure 7.19) and no orientation was detected in the droplets regime (Figure 7.17 b). This can be explained by shear cessation.

The experimental data furthermore show that the degree of orientation is higher close to the central axis of the jet and closer to the nozzle tip and depends on the particle aspect ratio and used flow rates. Spindle-shaped particles with high aspect ratio lead to a more pronounced particle orientation in the centre of the jet, rather than at the jet edges (Figure 7.18). The particles' orientation across the jet can be explained based on the high magnitudes of the flow velocity and the shear rates at the nozzle exit in the central axis of the jet as shown in literature [74, 112], thus, above and below the jet centre particles are less orientated.

The reduction of alignment was studied, for sample H2, $\nu = 6$, by comparing the rotation of the particles with a coefficient $\mathrm{D} = 6 \times 10^4\ \mathrm{rad}^2/s$) with classical Brownian rotational diffusion ($\mathrm{D}_r = 50\ \mathrm{rad}^2/s$).

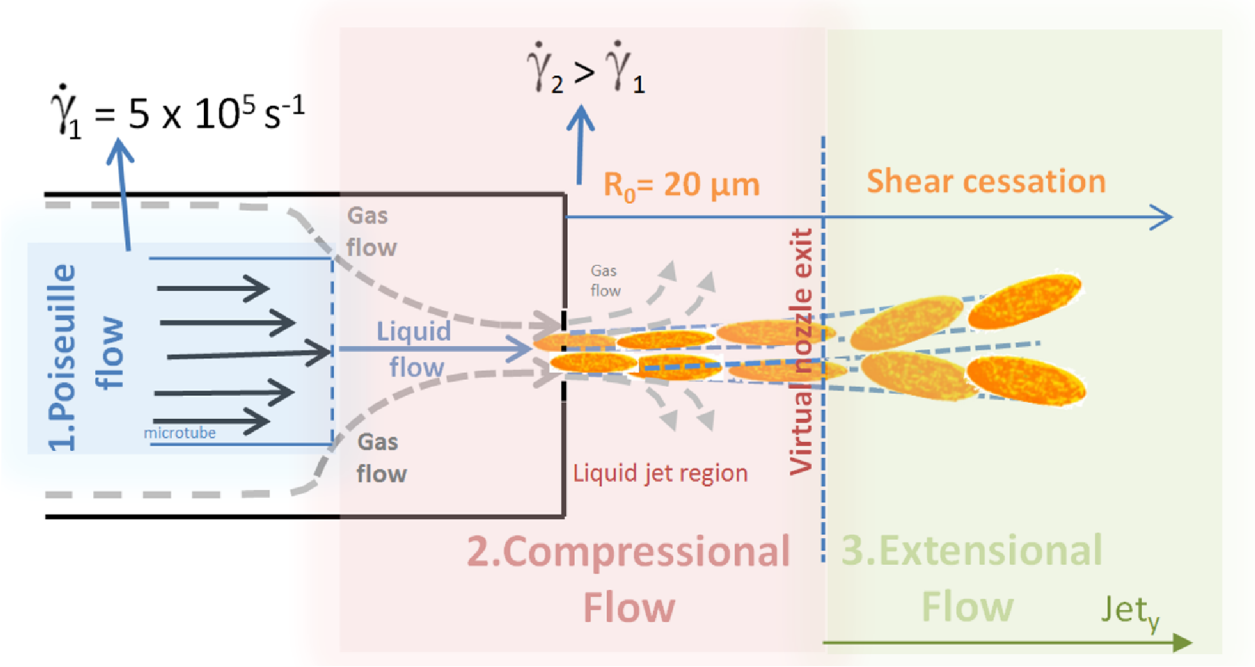

Figure 7.23: Sketch of a liquid microjet formed by a GDVN technique. Illustration of the different kinds of flows from the inside of the nozzle, 1 - Poiseuille and 2 - Compressional flow, and after jet collimation, 3 - Extensional flow and the respective shear rates behaviour. The obtained decrease of spindle-shaped particle's orientation along the jet is illustrated as well.

These two values differ by 3 orders of magnitude and it can thus be concluded that the particles behaviour is dominated by the flow and the decrease of shear along the jet and not by rotational diffusion. For the jet parameters in study ($V_{jet} = 5$ m/s and particles aspect ratio $\nu = 6$), the loss of alignment is observed only after $R_0 = 20$ μm from the nozzle tip and is higher than expected for thermal rotational diffusion. This suggests a shear cessation after this position in the jet and the most probable scenario is that the shear forces at the nozzle tip decreases orders of magnitude as shown in Figure 7.23 and predicted by simulation studies [99, 113].

This study gives a detailed characterization on the spindle-shaped particles' degree of alignment within a micro-jet and micro-droplets regime in a GDVN produced flow. Special attention is given to the question on how the particle aspect ratio and flow rates favours the spindle orientation. Furthermore, the time scale for a spindle-shaped particle rotation due to the extensional flow is extrapolated, characterized by the jet velocity and shear cessation in a microjet produced by GDVN.

Different studies of anisotropic particles' behavior within shear flows were published [15, 74, 101, 110, 112, 114]. This study shows for the first time a detailed analyses of spindle-shaped particles' behavior using samples with different and small aspect ratios and concentrations. For the first time the behavior of single particles in microjets is presented using a WAXS analyses, as well as a detailed characterization of particles rotation under shear flow produced by a GDVN.

Chapter 8

Small-angle X-ray scattering study on liquid microjets and microdroplets

The continuous injection using a GDVN has many important aspects due to the unique characteristics of these devices, such as: i) permanently refreshed sample, ii) no confinement effects, iii) sample delivered in a stable and controllable way and iv) it allows studies on supercooled liquids. However, some characteristics of these collimated jets are not understood so far, as for example the impact of jet geometries on SAXS using small beam dimensions.

SAXS studies using Rayleigh jets showed contribution from the jet shape, in particular from the jet edges, to the SAXS patterns [115]. This phenomenon was theoretically explained for static measurements [116] and reported, afterwards, for experimental studies using larger jets.

In this chapter, a detailed SAXS study is presented, mapping the different regions of a GDVN microjet of pure water and an hematite dispersion using a micro-focused beam. Experimental data is supported by a simulation study presenting the influence of the jet geometries on microjets characterization.

8.1 Microjets and measurements description

The jet was formed using a GDVN, described in chapter 1 as well as in [31]. As a guide for the liquid flow, a capillary micro tube (Polymicro GmbH, inner diameter $d_{\mathrm{i}} = 20$ μm and outer diameter, $d_{\mathrm{o}} = 150$ μm) was used. For the focusing gas, a second capillary ($d_{\mathrm{i}} = 100$ μm and $d_{\mathrm{o}} = 375$ μm) was added to the nozzle. These gas focused liquid jets were running at a pressure of p = 10^{-3} mbar inside the vacuum chamber.

A jet pre-characterization was done *in-situ* using the microscopes from the setup and the diagnostics holder, more details can be found in ref. [14]. Figure 8.1 a) shows the image of the running jet with the droplet regime taken during the experiment using the high magnification microscope with an exposure time of $t_{\mathrm{exp}} = 200$ ns. A jet length of 80 μm - 100 μm and diameter of 4 μm were measured, see Figure 8.1 a). Droplet diameters after the break up point varied between 8 μ and 12 μ (Figure 8.1 a). The difference between jet and droplet diameter is in accordance to Rayleigh's estimation

(equation 2.16), and to previous experimental work [40, 48].

The jet flow rate was about Q ≈ 7.5 μl/min corresponding to an average jet speed of $V_{\text{jet}} = 10.0$ ms^{-1}, this implies approximately of 1-5 $\times 10^5$ droplets/s, passing through the X-ray beam after the break-up.

As samples, Milli-Q water and sample H1 (Figure 8.1 b), a dispersion of spindle-shaped hematite particles (0.1 Vol.%) in water were used; for more details in sample characterization see chapter 5.

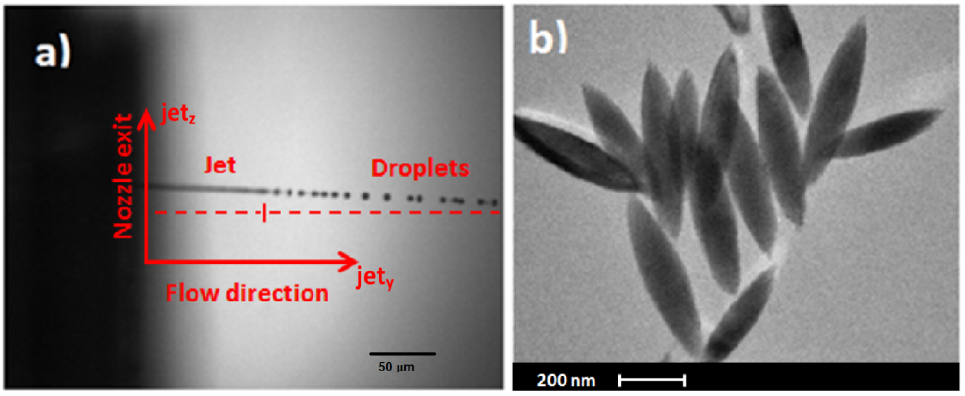

Figure 8.1: a) Microscope image of jet and droplets regime taken during the experiment. b) Transmission electron microscopy image of spindle-shaped hematite particles, sample H1, with an aspect ratio of 1:5.

SAXS patterns were measured at distances between 25 μm and 1000 μm from the nozzle exit, covering jet, break-up and droplet regimes. At every distance downstream the nozzle exit, different positions with intervals of 1 μm were collected perpendicular to the liquid flow direction. The single frame exposure time was t_e = 1 s and approximately 100 frames were taken at each spot. The two dimensional diffraction patterns taken along and across the jet were background subtracted using a SAXS pattern without jet running.

8.2 Sample characterization

In order to perform a qualitative SAXS study on liquid microjets and microdroplets, samples were previously characterized in a static environment which will be described in the next section.

8.2.1 Experimental analysis

Within this section, water and spindle-shaped hematite particles dispersed in water (sample H1) were characterized by measuring the particle orientation in a static environment using glass capillaries, without a magnetic field and under a magnetic field of $B \approxeq 150$ mT. As it is presented in chapter 5, the magnetic field plays an important role in the hematite samples orientation, since the particles orient with the c-axis perpendicular to a magnetic field.

The scheme of the static measurement under magnetic field is presented in Figure 7.2, where the capillary containing spindle-hematite particles is located between the magnets perpendicular to the beam direction. The SAXS detector is located 5 m away from the sample system.

For the characterization of the particles, a total of 100 SAXS patterns with exposure time t_{exp} = 0.5 s each were recorded. Every pattern was corrected by subtracting the background scattering from water measured in a capillary. Afterwards, all patterns were averaged, see the 2D scattering pattern in Figure 8.2 a) without a magnetic field and b) under a magnetic field of B ≈ 150 mT.

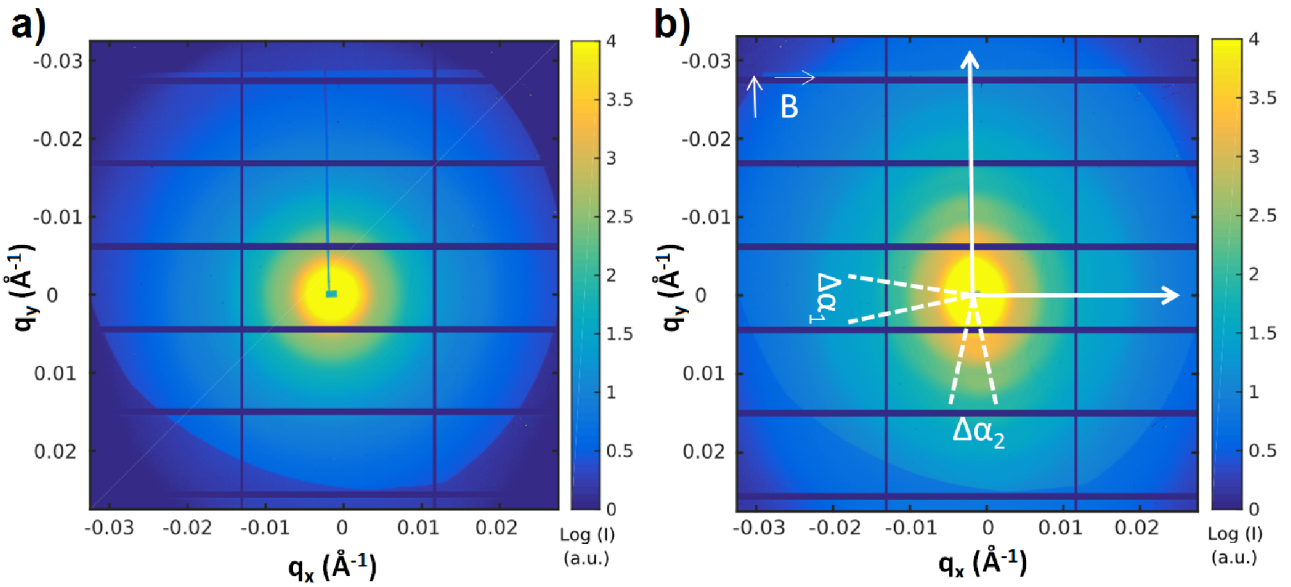

Figure 8.2: Averaged SAXS patterns of hematite particles (sample H1). a) Without magnetic field and b) under a magnetic field of B ≈ 150 mT which direction is depicted. Depicted $\Delta\alpha_1$ and $\Delta\alpha_2$ represent the range of the azimuthal integration along the small and long axis of the particle, respectively.

In Figure 8.2 a) an isotropic scattering pattern is visible indicating that spindle-hematite particles are randomly oriented, as shown in section 4.4.2. Figure 8.2 b) shows an anisotropic scattering diffraction pattern representing the orientation of the spindle-shaped particles under an external magnetic field. Since the minor axis of the spindle shaped particles is known [80] to align parallel to the field direction as explained in section 5.1.

In Figure 8.3 an azimuthal integration with $\Delta\alpha$ =17° around $\Delta\alpha_1$ perpendicular to the particle elongation direction (along particles' major axis) and along $\Delta\alpha_2$ in the direction of the elongation of the 2D scattering pattern (across particle short axis) is presented. The SAXS profiles along particles' short axis (blue symbols) and the particles' long axis (red symbols) show similar structures and the fall off behavior follows the same power law $I \propto q^{-4}$. However, the form factor taken along the short axis of the particle has weaker intensity when compared to the SAXS curve obtained from integration around $\Delta\alpha_1$, indicating a difference between the two directions. This is the result of the orientational averaging process. This observation indicates that the intensity contribution along one particle is different between the sectors, which shows differences between parallel and perpendicular orientations relatively to the external field.

The scattering data can be described by a form factor fit considering an ensemble of spindle-particles under an external magnetic field, underlying both, size and orientation distribution. Considering a polydisperse sample, the Schulz-Flory distribution was used to modulate the size of the particles' minor-axis, using eq. 4.13. The fit range was $q = 0.005$ Å^{-1} to $q = 0.04$ Å^{-1}.

Figure 8.3 shows fits (black solid lines) of the experimental data (hematite sample H1) along particles' short-axis (blue symbols, θ_q = π / 2) and along particles' major axis (red symbols, θ_q = π) for azimuthal averages of widths $\Delta\alpha = 17\ ^\circ$. The results obtained for the form factor fit yields to a polydispersity of p = 11.9 % $\pm$ 1.3 %, R_1 = 51.0 nm $\pm$ 0.3 nm and an aspect ratio of ν = 5.0 $\pm$ 0.2. Using the parameters which results from the fitting of the short axis of the particle the scattering signal along the particle major axis was fitted as well. These curves present a good agreement of the model with the data.

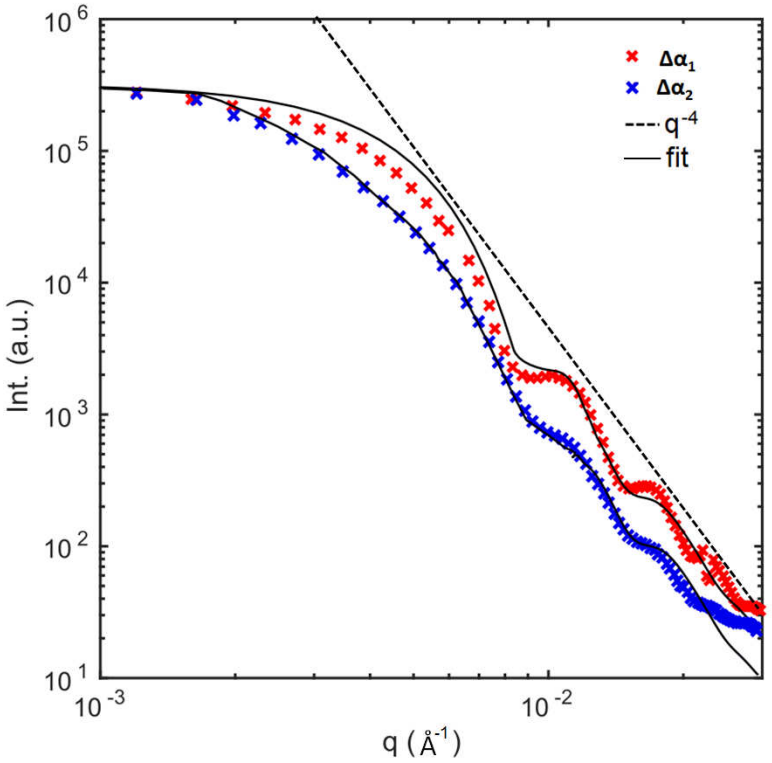

Figure 8.3: Integrated I(q) of the SAXS pattern along $\Delta\alpha_1$ and $\Delta\alpha_2$ directions with $\Delta\alpha = 17^\circ$ in log-log scale, for spindles aligned perpendicular to the magnetic field direction. The black solid lines represent a least-square fit, employing a form factor model of the Schulz-Flory distribution for $\Delta\alpha_1$ and $\Delta\alpha_2$, respectively.

These results are in qualitative agreement with earlier studies [15]. Additionally, the particles' aspect ratio extracted from the fit shows the same result of the one obtained from TEM images, see section 5.3.2.

8.3 SAXS on liquids microjets and microdroplets

Along this section, the impact of the geometries of a microjet and microdroplets on SAXS analysis is shown using a micro beam and two different samples systems, water and sample H1.

Water scattering patterns were measured at different spots within the jet (75 μm from nozzle tip), break-up (100 μm) and droplets regime (1000 μm). Figure 8.4 shows the measurement spots labelled in sub panel a and shown in the same figure in panels b - f. A closer look on the scattering patterns reveals different anisotropic signals in every position along and across the jet.

In the jet region (patterns b-d) a streak oriented perpendicular to the flow direction is observed. Pattern e is characterized by an anisotropic spherical scattering signal together with the streak. This anisotropic signal illustrates the break-up jet region where the droplets are being formed. In the droplets regime, pattern f, a anisotropic scattering pattern can be observed.

Similar patterns were observed for larger jets (d_{jet} = 100 μm - 450 μm) formed by Rayleigh nozzles. This was explained by scattering from jet surfaces [107, 115, 117]. Unlike to what has been observed in those studies, the streak is always present (in this study) when scanning across and along the jet, due to the similar dimensions of the jet and beam. The jet thickness was calculated based

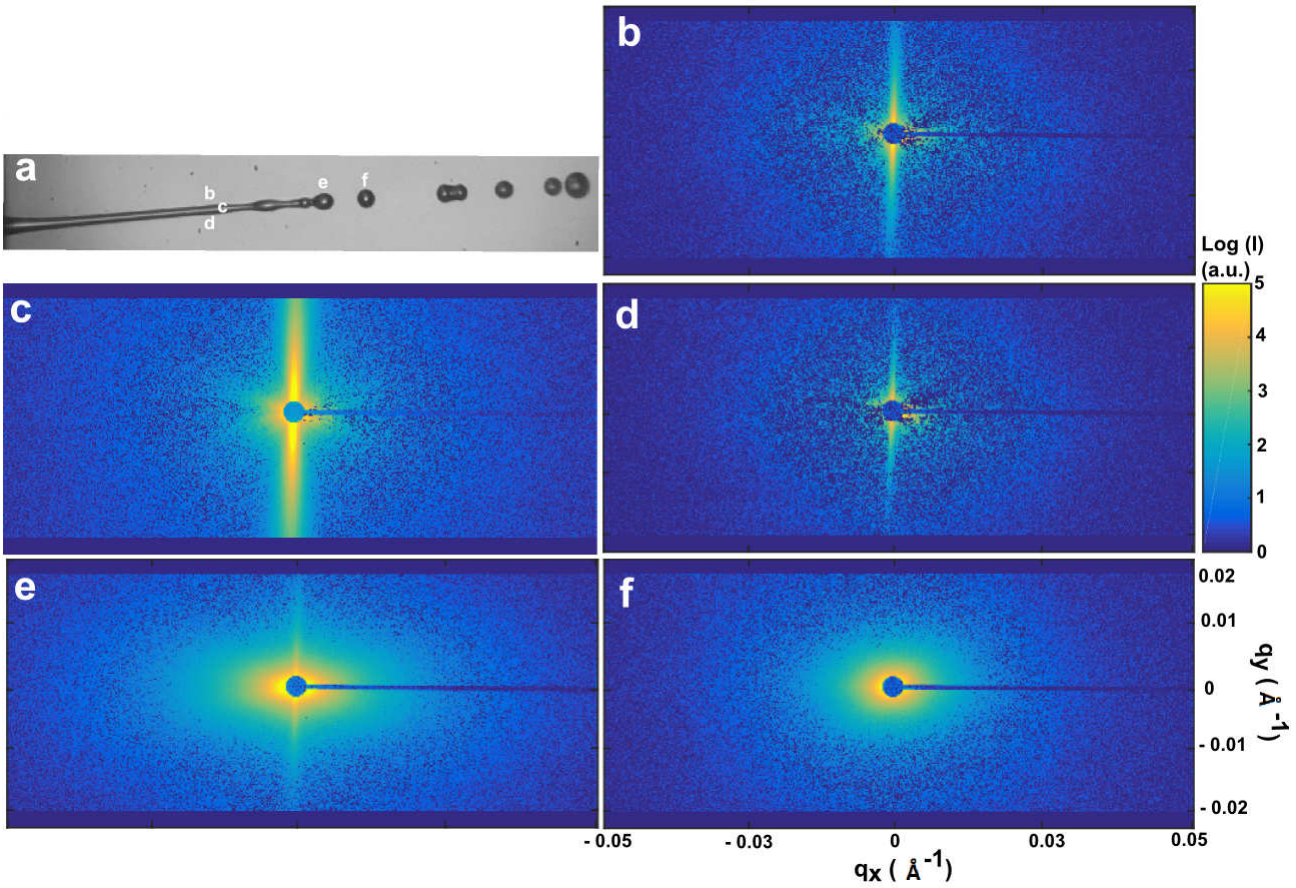

Figure 8.4: a) Water liquid jet scattering patterns taken with high the speed camera showing the different measured regions shown in b - f. SAXS patterns taken along and across the jet at different distances from the nozzle tip. Jet regime (b-d), measured at 75 μm from the nozzle tip, with figures b and d at the jet edges and c at the center of the jet. Break-up regime (e) and droplets regime (f) both measured at the jet center. Every pattern presents the same colorbar as well as q_x and $q_{\curvearrowright}$ label.

on the summed scattering intensity on the detector. The intensity collected across the water jet at 40 μm downstream the nozzle tip was modelled by a Gaussian function, see 8.5 a). The full width at half maximum (FWHM) was used to determine the edges of the liquid jet, thus the jet diameter d_{jet} is proportional to the FWHM of the Gaussian fit. The jet thickness is given after deconvolution with the vertical beam shape. In this way a jet diameter of d_{jet} = 4.0 μm is obtained in excellent agreement to the jet size measured using microscopes images during the experiment. In Figure 8.5 b) the so-obtained jet thickness is given as a function of increasing distance from the nozzle tip (Jet_y

direction).

In the same Figure, the three jet regimes are identified as jet (1), break-up (2) and droplets regime (3). In region 1 a constant value of jet diameter of d_{jet} = 4.0 μm is found until approximately 80 μm downstream the nozzle tip, corresponding to the jet length. Region 2 reflects the break-up regime for 80 μm $<$ Jet_y $<$ 120 μm. Afterwards, for Jet_y $>$ 120 μm, droplets are formed and d_{jet} reaches the maximum values of 10 μm. Different scattering patterns are found along and across the jet and droplets regime. The integrated intensity as a function of the wave vector q was analysed along the

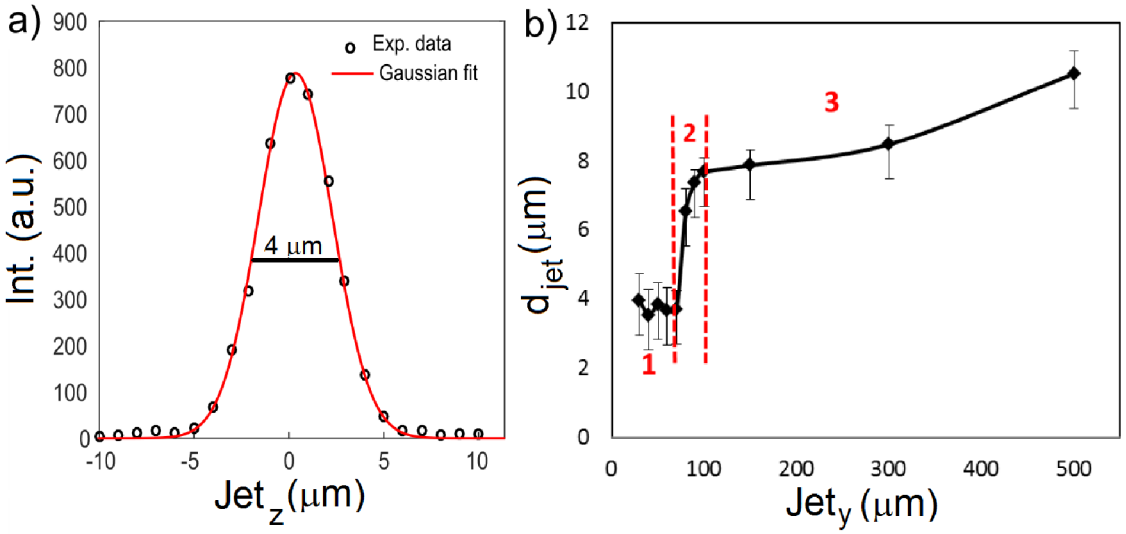

Figure 8.5: a) Summed scattering intensity measured across the jet at 40 μm downstream the nozzle tip together with a Gaussian fit. b) Jet diameter as function of the distance from nozzle tip. Solid line is a guide to eye. The dashed lines are limiting the break-up regime. Numbers 1, 2 and 3 represent the liquid jet, break-up and droplets regime, respectively.

streak and perpendicular to it, as will be shown below. The intensity decay I(q) was analysed in terms of a power law ($I \propto q^{-\beta}$) where the slope of the curves indicates the contribution of the total scattering intensity acquired across the jet.

Exponents β taken across the jet (along the streak) and in the droplets regime (droplets central axis) at 50 and 500 μm, respectively, downstream the nozzle exit are shown in Figure 8.6. The q-dependency changed from around $\beta_{jet} = 3.2$ in the jet regime to $\beta_{drop} = 3.9$ for the droplets regime. Remarkably, along the jet and droplets, β does not change significantly. From the data it is visible that a change of exponent values from $\beta_{jet} = 3.2$ to $\beta_{drop} = 3.9$ follows a change in the jet geometry from jet regime to droplets regime. This can be explained taken into account a simple model which describes the signal from different geometries, such as the signal from a cylinder (jet) and a spherical geometry (droplets regime) .

The equations for the diffraction signal from the jet geometry were developed for the first time by Hentschel *et al.* [116], and later in 2007, Plomp *et al.* show an equivalent approximated solution as

[118]:

$$I_r(\theta) = \frac{I_0 R_c}{2\varepsilon} \propto \frac{1}{[1 + (\theta/2\varepsilon)^2]^{3/2}}, \tag{8.1}$$

where ε is the refractive index decrement, I_0 is the intensity per unit length, and R_c the radius of the cylinder. The equation in only valid for scattering angles, $\theta < 2\delta$, being $\delta = \sqrt{2}\varepsilon$. Thus the behavior for $\theta < 2\delta$ and the asymptotic behavior for higher scattering angles, can be approximated to [115]:

$$I_r(q) \propto 1/q^3. \tag{8.2}$$

Considering droplets as spheres, equation 8.1 can be expanded to the isotropic case, yielding [115]:

$$I_r(\theta) = j_0 R^2 \frac{1}{2\varepsilon} \propto \frac{1}{[1 + (\theta/2\varepsilon)^2]^2}, \tag{8.3}$$

where j_0 is the photon flux density and R the droplets radius. Thus the asymptotic behavior for large scattering angles can be approximated to [115]:

$$I_r(q) \propto 1/q^4. \tag{8.4}$$

Hereupon for a cylindrical geometry, such as a liquid jet, an exponent of $\beta_{\text{jet}} = 3$ is expected, contrasting with $\beta_{\text{drop}} = 4$ for spheres [115, 116, 119].

However, small deviations from experimental exponents of q-dependencies in the jet regime and theory prediction are observed. This can be caused by the intrinsic instabilities that propagate along the jet surface until the break-up. These fluctuations are known as capillary waves [1, 48], and will be modelled along the jet to explain the presence of small deviations to the theoretical data.

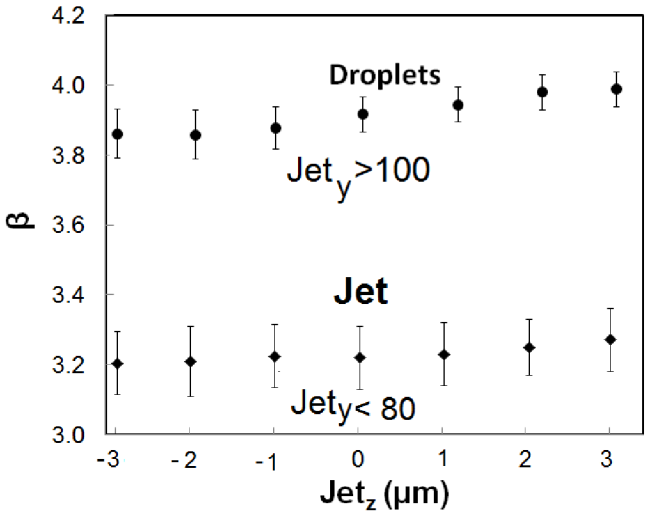

Figure 8.6: Exponents of q-dependencies from data collected across the jet, from jet (diamond) and droplets (sphere) regimes at 50 μm and 500 μm downstream the nozzle exit.

In order to model the experimental scattering signals acquired along the jet and the contribution

of the fluctuations to that signal, a model study was performed (a sketch of the steps of the code is presented in Appendix D). In the model, diffraction patterns along and across a microjet and micro-droplets were simulated assuming the jet as cylindrical shaped and droplets as spheres geometries with $d_{jet} = 4$ μm and $d_{drop} = 8$ μm diameter, respectively, see Figure 8.7 a) and c). In Figure 8.7 b) a calculated jet with modelled fluctuations along the jet surfaces is shown in order to understand how the presence of these intrinsic instabilities contributes to deviations in experimental results.

Simulated data were convoluted by a 2D Gaussian beam (3×3 μm^2) and the scattering patterns were collected within scans of 1 μm steps similar to the experimental procedure. The scattering before

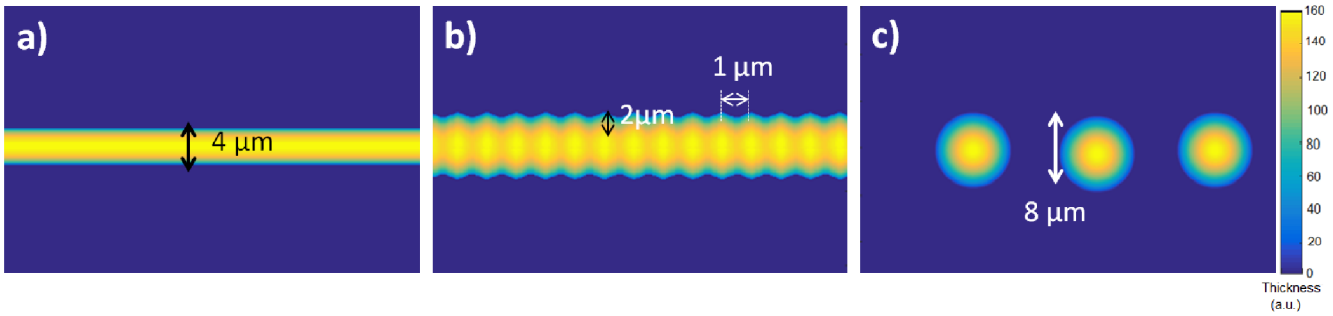

Figure 8.7: Schematic of modelled diffraction patterns from a) jet regime b) break-up regime and c) droplets regime. The cylindrical jet shape was modelled with a diameter $d_{jet} = 4\mu$m, fluctuations were simulated along the jet with wave amplitude $A = 2\mu$m, and period, $t = 1\mu$m. The droplets were simulated as sphere geometries with diameter $d_{drop} = 8\mu$m.

the break-up point is dominated by a sharp streak, see Figure 8.8 a), representing the scattering from the cylindrical jet shape, observed as well in the experimental results. Modeled SAXS patterns in the droplets regime, Figure 8.8 b), an oblate-prolate anisotropic pattern is presented being representative for the spherical geometry, characteristic for the droplets regime. Similar patterns were acquired in the experiment (see Figure 8.4 f).

Jets with and without fluctuations were modelled to understand their main role on the jet surface and consequently in the q-dependencies behavior. These waves were simulated using a wave amplitude of $A = 2$ μm and period of $t = 1$ μm.

The simulated SAXS scattering signal from the jet column, with and without fluctuations, break-up regime and droplets were analysed as a function of wave vector transfer q. The intensity decay was fitted by a power law exponent along the streak and at the center of droplets, similarly to the experimental data. The integrated region is depicted in Figure 8.8 a) and b), the exponents of q-dependencies β were calculated for a jet with and without fluctuations and for the droplets regime, presented in panel c).

For both regimes, the calculated data shows that the maximum β of the curve moves towards values of $\beta = 3$ and $\beta = 4$ for jet and droplets, respectively, as expected from theory. In the case of the jet modelled with fluctuations a slope of $\beta = 3.3$ is formed while a slope of $\beta = 2.9$ is obtained for the jet computed without fluctuations.

Form the model data, one can conclude that the presence of the fluctuations along the jet can be responsible for the β deviations observed in experimental data. In the droplets regime the exponents

are in agreement with both experimental and theory predictions. To understand the major contribution

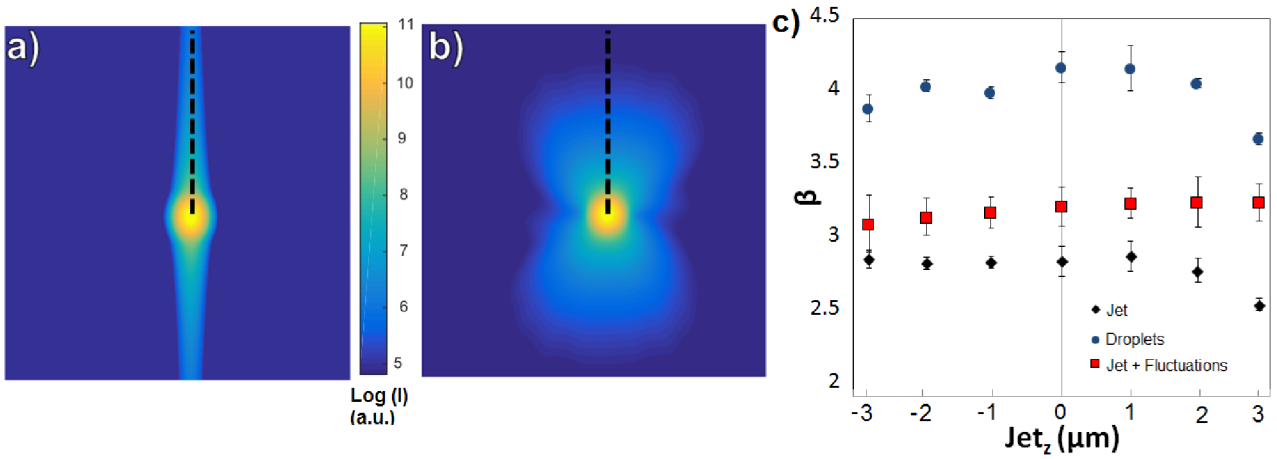

Figure 8.8: Simulated scattering patterns from: a) jet ($d_{jet} = 4$ μm) and b) droplets regimes ($d_{drop} = 8$ μm). The black straight line indicates where the analysis has been performed. c) Simulated q-dependencies taken across the jet without fluctuations (diamond), with simulated fluctuations (squares) and droplets regime (sphere).

of the fluctuations in the behavior of experimental data, a dependence of the wave amplitude and period as a function of q-dependencies of the integrated data along the jet regime was studied, see Figure 8.9. Waves with 0 μm $<$ A $<$ 2.5 μm and period $t = 1$ μm were simulated and the respective β of the integrated data at the jet centre calculated (Figure 8.9 a)). The graph shows a parabola correlation between the amplitude of the fluctuations and the slope observed at the centre of the jet which can be described by the equation: $\beta = 0.1128A^2 - 0.259A + 2.9801$. Note that the simulated

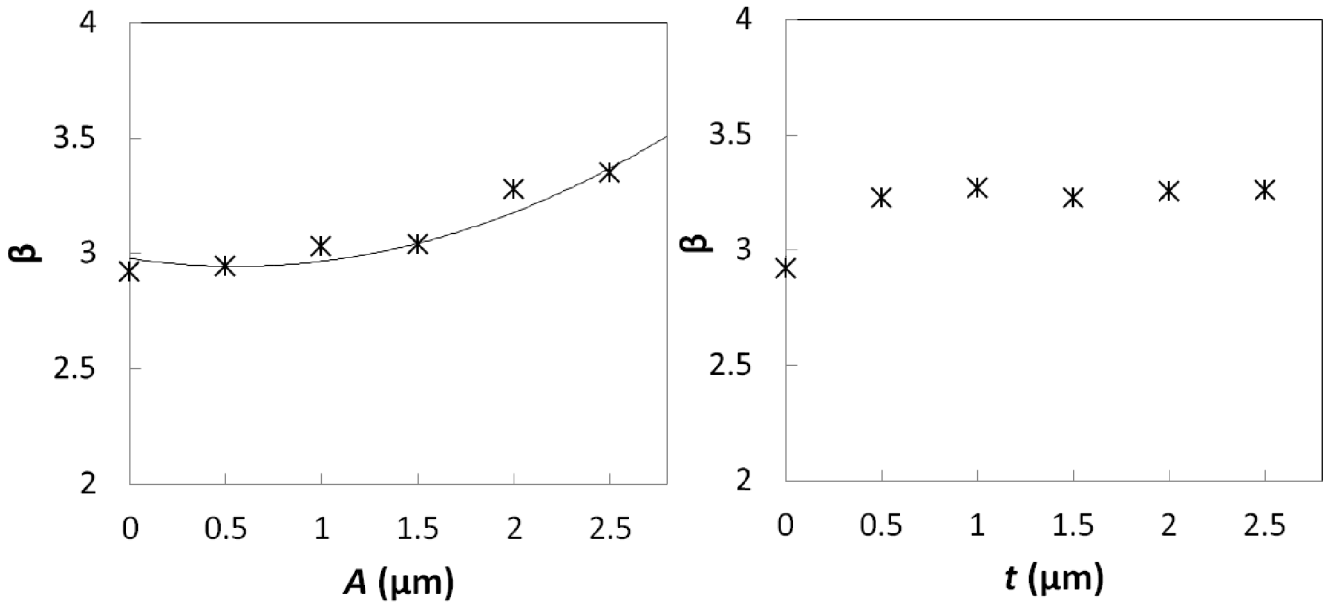

Figure 8.9: Simulated dependence of a) β vs A using a wave period of $t = 1$ μm and b) β vs t using a wave amplitude of $A = 2$ μm. The simulated jet diameter is $d_{jet} = 4$ μm. (Line is a guide to the eye).

fluctuations along the jet with $A = 0$ μm results in a $\beta \simeq 3$ agreeing with the value for cylindrical

shape predicted by theory.

In Figure 8.9 b) the wave period is shown as a function of β using a fixed $A = 2$ μm. As visible in the graph, the q dependence is independent of the wave period when measured at an $A = 2$ μm. Therefore it is possible to conclude that the slightly higher slope of $\beta = 3.2$ obtained experimentally compared to the cylindrical shape ($\beta = 3.0$) corresponds to the presence of the fluctuations which travel along the jet surface with an amplitude of $A \approx 2\mu$m and period $t \approx 1$ μm. Thus, such a simple geometrical model can describe the experimental data.

As demonstrated in chapter 7, different hematite particles shows different behavior along the microjet. In order to study the behaviour of a different sample in the jet by a SAXS analysis, sample H1 will be introduced in the next paragraphs.

A dispersion of spindle-shaped hematite in water, which characterization was given in Chapter 5, will be studied along the microjet using a micro beam size. Since hematite particles have a preferable orientation in shear flows, observed by the WAXS analysis (chapter 7) different anisotropic SAXS patterns are as well expected to be measured along and across the jet. Thus, a qualitative analysis to the scattering patterns at the different distances downstream the nozzle tip will be shown in this section.

SAXS patterns from hematite dispersion acquired at 75 μm and 500 μm downstream the nozzle tip are shown in Figure 8.10. The patterns were integrated along the streak direction, $\theta = \pi$, and perpendicular to it, $\theta = \pi$ / 2, as depicted in panels a) and b), respectively.

The strong streak reflecting the jet cylindrical shape at 75 μm from the nozzle tip as well as spherical scattering patterns representing the droplets regime are similar to the ones measured for water. Although nozzle parameters were similar for water and hematite measurements, the jet formed by the hematite dispersion appears at a tilt angle of about 20°, depicted in Figure 8.10 a). This can be explained by different sample properties, such as viscosity.

SAXS profiles from water and hematite dispersions are presented in Figure 8.10 c) by the angular integrated intensity, I, as a function of q. A similar behavior is observed for hematite dispersion data taken along and perpendicular to the streak. However, subtle differences in intensity, are observed. Most importantly, the curve's fall off follows the same power law. The intensity of both curves falls proportional to q^{-4} as expected for an orientational average of spindle-shaped particles, as observed for the static characterization of the sample in the section 8.2.1. In earlier studies [15] it was observed that the curve falls off differ for different angles and relative to the particle orientation. The form factor along particle major axis falls proportional to a power law with $I \propto q^{-6}$ while perpendicular to it a q^{-4} dependence was obtained [15]. However, in this experimental study the curves presented in Figure 8.10 c) show the same fall off. This result indicates the superposition of the scattering of jet shape effects and the sample scattering signal.

Comparing water and hematite dispersion, for both angular regions, only subtle differences in intensity along the streak region are visible, although the most important conclusion is that the fall off of the curves are similar. As results taken along the microjet do not show significant differences in the q-dependencies along the different angles, indicates that the scattering from cylindrical shape superimposes the scattering from particles.

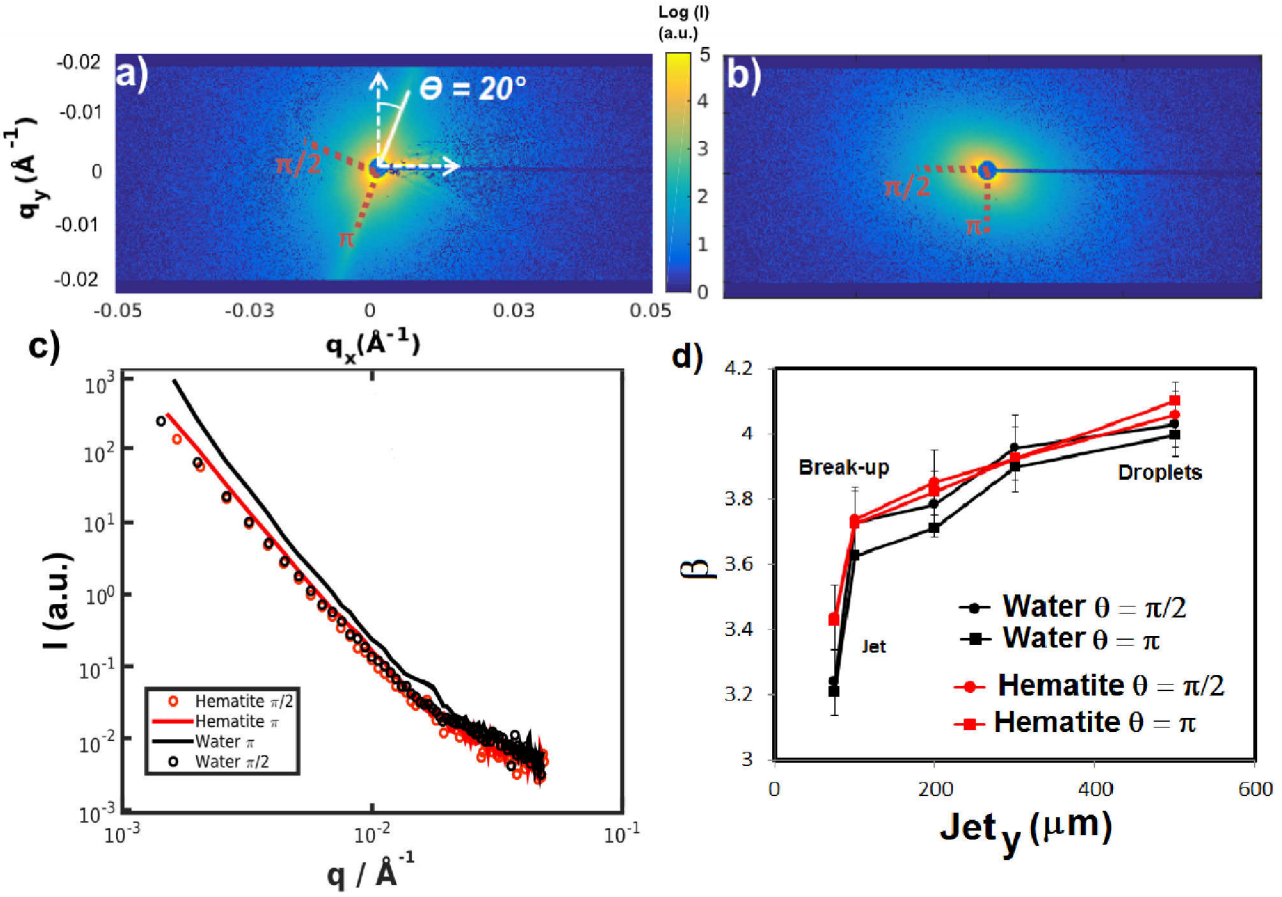

Figure 8.10: SAXS patterns from hematite dispersion acquired at the jet center and from different distance of nozzle tip: a) 75 μm and b) 500 μm, corresponding to jet and droplets regime respectively. The angle directions $\theta = \pi$ and $\theta = \pi/2$ used for the data analysis are depicted in both patterns. c) A log-log plot of the integrated intensity I as a function of momentum transfer q taken at jet regime, 75 μm downstream the nozzle tip. The scattering curves of water and hematite dispersion presents the integration along the streak direction, $\theta = \pi$, and and perpendicular to it ($\theta = \pi/2$). d) Comparison of q-dependencies measured at different distances along the jet for water and hematite dispersion along the different depicted angles.

A quantitative analysis of the q-dependencies of the SAXS curves is presented in Figure 8.10 d). Therein, β values taken at different angles, along the jet, break-up and droplets regimes are compared for water and hematite dispersion.

The jet regime is characterized by a slope of $\beta = 3.4$ for the hematite dispersions while a $\beta = 3.2$ was acquired for pure water. This small deviation agrees within experimental error bars. The droplets regime is represented by $\beta = 4$ for both samples. These slopes of the SAXS curves agreed to the β values expected from theory and simulation data from the respective shape contributions, taking into account the contribution of fluctuations acting on the jet regime. Thus, SAXS profiles from water and hematite dispersions taken along the microjet do not show significant differences when produced by a GDVN and using a focused microbeam. Both samples in study are as well in agreement with the simulated data.

8.4 Conclusion

In the present study a report on the impact of jet geometries on scattering patterns analysed by SAXS using microbeams sizes is shown. A detailed data analysis using water and a hematite dispersion is given by mapping the scattering signal over and across the jet, break-up and droplets regimes. Using SAXS combined with a micro-focused beam, a accurate way of liquid jet characterization is shown comparing experimental and modelled data.

Different anisotropic scattering signals were measured along and across the jet, break-up and droplets regimes. A strong streak was always present in jet region representing the scattering from the jet cylindrical shape. In contrast, scanning the droplets regime, a spherical anisotropic signal arises due to the scattering from the spheres' shape.

The anisotropy of SAXS patterns obtained experimentally from both samples are not sample dependent. The reason for this intense anisotropic signal is based on the scattering from the different jet shapes along the microjet. The scattering signal obtained over the jet is characteristic for the cylindrical shapes expected from theory and proven by simulations. The same conclusion can be made for the droplets regime where the experimental scattering signal reflects the expected one from spherical geometries, from both, theory and simulation studies.

The anisotropy of scattering patterns obtained along the microjet is dominated by the diffraction from the jet shapes what makes the extraction of the sample signal challenging. This fact can be explained based on the similar dimensions of the microjet and the microbeam sizes, which can be overcome by using larger jet diameters with a microbeam size, as done by Lehmkühler $et\ al.$ [101]. Therefore, in order to extract the scattering from samples over the scattering signal from the jet shape, the jet size and the size of the microbeam has to be taken into account.

Chapter 9

Summary and outlook

In the framework of this thesis two main topics have been studied:

1. A WAXS study on the behavior of spindle-shaped particles in a GDVN produced flow.

2. A SAXS study on the impact of microjet and microdroplet geometries on the scattering patterns.

For the realization of this PhD study, X-ray scattering experiments were performed at PETRA III at beamline P10.

Since liquid microjets produced by gas dynamical virtual nozzles have proven valuable for structural and time-resolved studies at synchrotron radiation facilities [15] and X-ray Free Electron Laser (XFEL) sources, the continuation of these studies is crucial and necessary.

The existing liquid jet setup [14], has been improved in the framework of this thesis, and used together with a GDVN system to produce the microjets. In this work the stability of the setup has been improved, increasing the reproducibility of the measurements. All procedures used for the jet characterization and nozzles exchanges have become faster and more precise. The collimated microjets were produced with different nozzle dimensions using the GDVN technique, originally developed by Gañán-Calvo [31]. Gas focused liquid jets with different diameters (2 μm - 30 μm) were obtained and the X-ray scattering measurements were performed along and across the microjet and the microdroplets.

As samples, spindle-shaped hematite particles dispersed in water have been used. They were synthesized with different aspect ratios and concentrations. The sample characterization was performed by TEM, HRTEM, SAED and XRD. Since these particles are known to align perpendicular to the direction of an external magnetic field [80], a static characterization of the spindles was performed under a magnetic field by X-ray scattering.

After a detailed particle characterization, the single crystallinity of the particles was confirmed as well as that the c-axis of the unit cell is oriented parallel to the particles' major axis. Due to their anisotropic shape these particles are known to be sensitive to shear flows. The behavior of spindle-shaped particles in the flow was characterized by a Bragg diffraction analysis using WAXS for different particle aspect ratios and flow rates. The azimuthal width of the discontinuous Debye Scherrer rings and their positions varied along the jet which indicates different particle orientations.

Particle orientation is produced by Pouseuille flow in the microtube where shear rates above $\dot{\gamma} = 10^4$ s^{-1} are achieved. Afterwards, the liquid is pressed out into a compressional zone where the jet collimation is performed. The sample is then stretched out into an extensional zone characterized by an alignment of the particles in the flow direction. The degree of orientation decreases slightly along the jet and no alignment was detected in the droplets regime. This behavior is explained by the cessation of shear upstream of the nozzle tip. Particles with a high aspect ratio showed a higher degree of alignment along the jet and at the jet centre.

The spindles showed a very high shear rotation coefficient along the jet when compared to the diffusional rotation by Brownian motion. The difference between these two values indicates that the particles behavior is dominated by the flow and shear cessation.

A model was used to quantify the results suggesting that the particles are not perfectly aligned along the flow direction, but always display a deviation along the c-axis. The c-axis deviation increases along the jet which results in larger widths of the discontinuous Debye Scherrer rings. In the droplet regime the Debye Scherrer rings are complete indicating a random particle orientation.

Thus, this study is a detailed characterization of the behavior of particles in shear flow produced by a GDVN, with special emphasis on how the particle aspect ratio favors the spindle orientation. This work has thus helped to predict the orientation of different shapes and dimensions of particles in flow from the sheared to the unsheared regime.

In the second part of this thesis, a SAXS study on microjets and microdroplets was performed. Therein, a detailed data analysis using water and aqueous hematite dispersions was performed. A map of the scattering signal along and across the jet, break-up and droplets regime was created. Furthermore, the data was modeled based on the jet geometry.

A strong streak was always present in the jet region representing the scattering from the cylindrical shape of the jet characterized by a q dependence of intensity $I \propto q^{-3}$. In the droplets regime the signal is isotropic due to the scattering from spherical shapes showing $I \propto q^{-4}$. Deviations have been observed in the experimental data such as $I \propto q^{-3.2}$ in the jet regime. This deviations were shown to arise when instabilities with amplitude $A = 2$ μm and period $t = 1$ μm were taken into account along the jet surface.

Anisotropic patterns were similar for both samples under study, in particular, being independent from sample shape or viscosity, despite of the different form factors expected for hematite. This observation indicates that in order to extract the scattering from samples over the scattering signal from the jet shape the size of the jet and the size of the microbeam has to be taken into account. To overcome this limitation, larger jets complemented with a micro-beam sizes should be used.

Future work related to fluids in flows may include:

- Simulation studies for the characterization of the shear formed by GDVN during the jet collimation are crucial for a better characterization of the flow created by a GDVN.

- So far, a detailed single particle study was presented in the framework of this thesis. Future

work including interparticle correlations (Expressed in the structure factor S(q) of the system) would be important. An equivalent study was performed using spherical silica particles showing direction-dependent modifications of the structure factor of the suspension, which indicate the formation of ordered clusters [101].

- By using diffraction limited storage rings (e.g. PETRA IV or ESRF-EBS) [120, 121] a more detailed jet characterization could be performed due to the smaller beam sizes available. The higher coherence of the beam and faster times scales will allows to measure the particles' dynamics using X-ray photon correlation spectroscopy [122–125].

- Liquid jets are often used at XFEL sources where new types of experiments such as particle imaging of biomolecules [126, 127] or correlation studies [128, 129] are performed. Therefore the flow alignment of such bio-molecules may need to be considered and taken into account in future experiments.

New developments related to the liquid jet setup should include:

- Increase the reproducibility of the GDVN fabrication.

- Implementation of piezo nozzles as shown in [8]. This new injection system facilitates the studies of supercooled liquids by the production of homogeneous sized and spaced droplets [105, 130].

- Implementation of a Raman spectrometer in the liquid jet setup to be able to have a more precise $in\ situ$ measurement of the temperature for the different sample systems used, as performed in [130].

Appendix A

List of hazardous substances

- **IUPAC name** : **Iron(III)cloride**

  Chemical formula: $FeCl_3$

  GHS Signal word: Danger

  GHS hazard statements: H290, H302, H314, H318

  GHS precautionary statements: P234, P260, P264, P270, P273, P280, P301+312, P301+330+331, P303+361+353, P363, P304+340, P310, P321, P305+351+338, P390, P405, P406, P501

  Danger symbol:

Figure A.1: GHS pictograms for Iron (III) cloride.

- **IUPAC name** : **Sodium dihydrogen Phosphate**

  Chemical formula: NaH_2PO_4

  GHS Signal word: Warning

  GHS hazard statements: H315, H319, H335

  GHS precautionary statements: P261, P264, P271, P280, P302+P352, P304+P340, P305+P351+P338, P312, P321, P332+P313, P337+P313, P362, P403+P233, P405, and P501

Danger symbol:

Figure A.2: GHS pictograms for Sodium dihydrogen Phosphate.

Appendix B

Different liquid jet experiments at P10

To understand the hematite particle behavior under a shear flow produced by a GDVN, four different X-ray experiments were performed at beamline P10 during the framework of this project. For that, different GDVN nozzles were produced with different inner-tube diameter as well as different samples were analysed, of which some TEM images, not shown in chapter 5, are presented in Figure B.1.

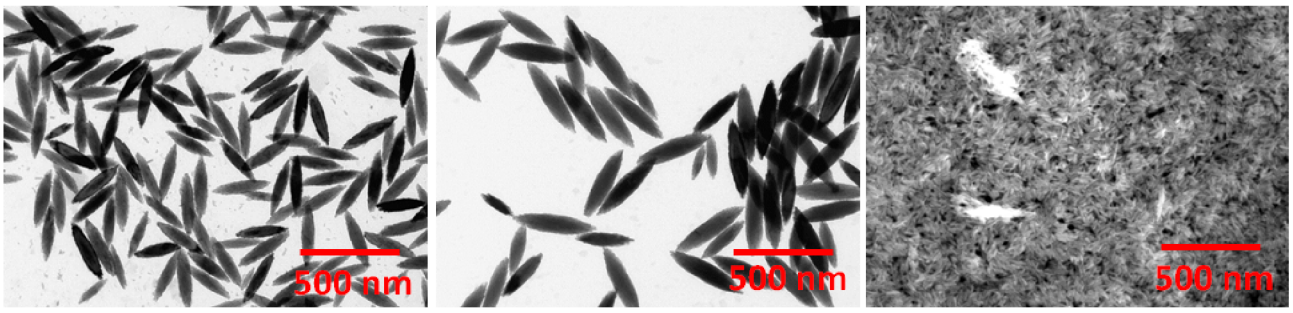

Figure B.1: TEM images of some examples of different spindle-shape hematite particles synthesized in the framework of this project, not shown in chapter 5. a) sample H4, $\nu = 5.5$, b) sample H5, $\nu = 4.0$ and c) sample H6, $\nu = 6.0$.

The first beamtime was restricted to SAXS regions with X-ray beam energy of E = 8 KeV, while the following ones where performed in wide angle regime using E = 13 KeV. Pilatus 300K was the detector used in each beamtime. A short summary on nozzles used at each beamtime is presented in table B.1.

Table B.1: Summary of different samples, nozzles parameters and jet sizes measured at different experiments.

Beamtime	Sample	Nozzle tube (μm)	Flow (μl/min)	Jet break-up (μm)
Exp. 1 - SAXS	H1, H4	20, 25	8-20	100 - 150
Exp. 2 - WAXS	H2, H5, H6	10, 20, 50	5-20	75 - 300
Exp. 3 - WAXS	H2, H5, H6, H7	20, 25, 50, 100	8 - 150	100 - 500
Exp. 4 - WAXS	H3, H8	20, 30, 50	8-20	100 - 300

In Figure B.2 different sub-figures showing the break-up of the jets obtained during the experiments using different flow rates and nozzles diameters are presented taken with high magnification

microscope.

Figure B.2: Images of different jet break-up obtained in different experiments, using different jet dimensions: a) 50 μm b) 20 μm and c) 10 μm.

Appendix C

Sample characterization via HRTEM - Sample H2

In addition to H3 sample characterization by HRTEM, shown in chapter 5, the characterization of sample H2 via HRTEM is here presented. The analysis was performed following the same steps explained in Chapter 5. From the SAED and high magnified images (Figure C.1) one can conclude a well defined single crystalline structure. From the crystalline structure arrangement it is possible to conclude that the orientation of the c-axis of the unit cell is parallel to the long-axis of the ellipsoid as for sample H3.

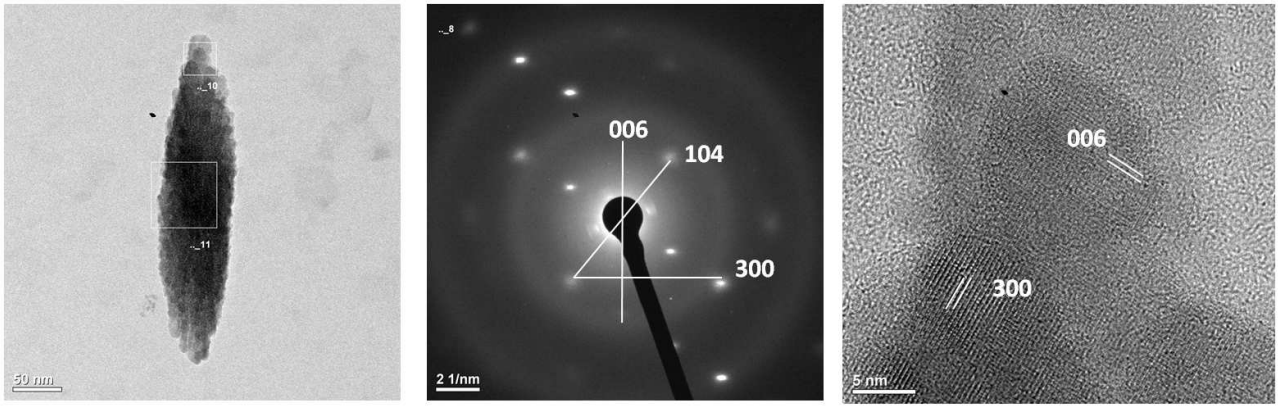

Figure C.1: HRTEM images of spindle-shaped hematite from sample H2.

Appendix D

SAXS model study

To better follow the SAXS signal acquired experimentally along the microjet and microdroplets a model study was created computing the scattering signals acquired along and across the jet and droplets. A sketch of the steps of the implemented code are shown in Figure D.1. The diffraction patterns along and across the microjet were simulated assuming a jet as a cylindrical shape with 4 μm diameter, which was afterwards projected to a 2D density map. A thickness function of a cylinder was calculated afterwards. This computational data is convoluted by a 2D Gaussian beam (3×3 μm ^{2}) by moving the jet in several steps across the beam which was assumed fixed. The step size performed was 1 μm similar to experimental data.

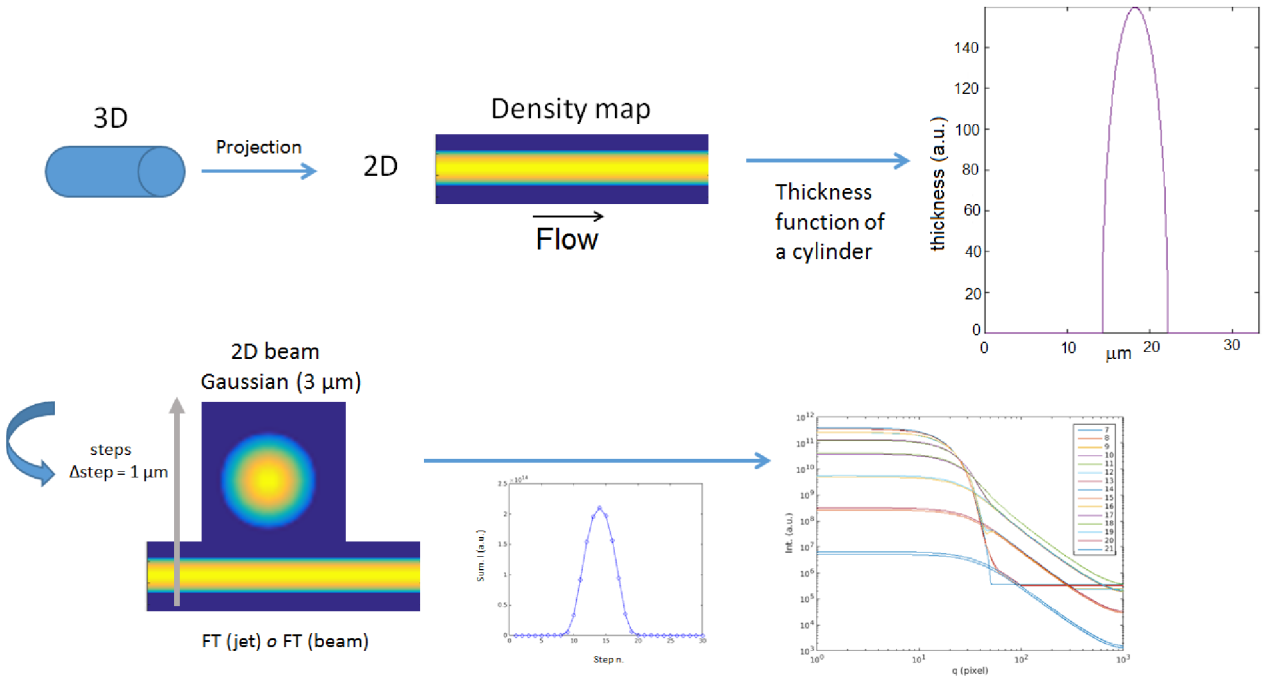

Figure D.1: Illustration of code steps on how the model study on jet shape was performed.

The scattering was modelled by the Fourier transform from the beam with the jet. Afterwards the sum of the intensity is plotted as a function of step number, resulting in a jet profile. The last step of the analysis is the integration of the intensity as a function of the wave vector q. The resulting slope is investigated in chapter 8.

The experimental jet surface fluctuations were modelled as well to explain deviations observed in the experimental data. Studies were performed changing the amplitude and the period of the fluctuations, see chapter 8.

The scattering patterns along and across the microdroplets were modelled as well assuming a sphere with 8 μm diameter as the droplets geometry. The steps of the code follow the same steps used for the jet, however, for the droplets regime a time-average over different droplets states was implemented and over different droplets positions along the flow direction.

Bibliography

[1] J. Eggers, E. Villermaux., *Rep. Prog. Phys.* **2008**, *71*.

[2] https://www6.slac.stanford.edu/news/2015-02-02-5-ways-put-tiny-targets-front-x-ray-laser.aspx (in Feb. 2018).

[3] G. D. Calvey, A. M. Katz, C. B. Schaffer, L. Pollack, *Structural Dynamics* **2016**, *3*, 054301.

[4] S. Lin, *Breakup of Liquid Sheets and Jets*, Cambridge University Press, **2003**.

[5] R. P. Grant, S. Middleman, *A.I.Ch.E. J.* **1966**, *2*, 669 –678.

[6] S. J. Leib, M. E. Goldstein, *The Physics of Fluids* **1986**, *29*, 952–954.

[7] E. J. Vega, J. M. Montanero, M. A. Herrad, A. M. Gan-Calvo, *Physics of Fluids 22, 064105* **2010**, *22*, 064105.

[8] T. Kalff, Master's thesis, Fachhochschule L*ü*beck, **2017**.

[9] F. Pinto, M. Meo., *Appl Compos Mater.* **2017**, *24*, 643–660.

[10] J. Wagner, *J. Appl. Cryst.* **2004**, *37*, 750.

[11] W. H. de Jeu, *Basic X-ray Scattering for soft matter*, Oxford, University Press, **2016**.

[12] R. L. Blake, R. E. Hessevick, T. Zoltai, L. Finger, *The American Mineralogist* **1966**, *51*, 123–129.

[13] *Reference data with the PDF-card-Nummer: 01-087-1166*.

[14] I. Steinke, M. Walther, F. Lehmkhler, P. Wochner, J. Valerio, R. Mager, M. A. Schroer, S. Lee, W. Roseker, A. Jain, M. Sikorski, S. Song, R. Hartmann, M. Huth, L. Strder, M. Sprung, A. Robert, P. H. Fuoss, G. Stephenson, G. Grbel., *Review of Scientific Instruments* **2016**, *87*, 1–6.

[15] I. Steinke, Ph.D. thesis, Hamburg University, **2015**.

[16] M. Sprung, *P10 Coherence Beamline User Guide*, **2016**, http://photon-science.desy.de/sites/site_photonscience/content/e58/e176720/e177229/e178737/e179091/e179098/e269721/P10_User_Guide_2016_eng.pdf.

[17] E. Mariotte, *Traite du mouvement des eaux et des autres corps fluides.*, P. E. Michallet (Ed.), **1686**.

[18] J. W. S. Rayleigh, *Proc. Lond. Math. Soc.* **1878**, *10*.

[19] J. B. Keller, S. I. Rubinow, Y. O. Tu., *Phys. Fluids,* **1973**, *16*, 2052.

[20] W. T. Pimbley, H. C. Lee, *IBM J. Res. Dev.,* **1977**, *21*, 21–30.

[21] J. Eggers, *Phys. Rev. Letters* **1993**, *71*, 3458–3460.

[22] M. Faubel, B. Steiner, J. P. Toennies, *J. Chem. Phys.* **1997**, *106*, 9013–9031.

[23] A. J. Mello, *Nature* **2006**, *442 (7101)*, 394–402.

[24] J. El-Ali, P. K. Sorger, K. F. Jensen., *Nature* **2006**, *442*, 403–411.

[25] B. H. Weigl, R. L. Bardell, C. R. Cabrera, *Adv. Drug Deliv. Rev.* **2003**, *55(3)*, 349–377.

[26] K. Tono, *High Power Laser Science and Engineering* **2017**, *5*, 1–7.

[27] A. M. Gan-Calvo, J. M. Montanero, *Physical Review E - Statistical, Nonlinear, and Soft Matter Physics* **2009**, *79*, 1–18.

[28] V. M. Aniskin, S. G. Mironov, A. A. Maslov, *Nanofluid* **2013**, *14*, 605–614.

[29] V. M. Aniskin, A. A. Maslov, S. G. Mironov, *Technical Physics Letters* **2011**, *37*, 1046–1048.

[30] S. D. Scroggs, G. S. Settles, *Exp. in Fluids.* **1996**, *21*, 401409.

[31] A. M. Gan-Calvo, *Physical Review L etters* **1998**, *80*, 285.

[32] G. M. Whitesides, A. D. Stroock, *Physics Today* **2001**, *54*, 42–48.

[33] J. M. Ng, I. Gitlin, A. D. Stroock, G. M. Whitesides., *Electrophoresis* **2002**, *23*, 3461–3473.

[34] S. Köster, T. Pfohl, *Mod. Phys. Lett. B.* **2012**, *26*, 1230018.

[35] L. Daubersies, J. Leng, J.-B. Salmon, *Lab Chip* **2013**, *13*, 910–919.

[36] D. Oberthuer, J. Knoka, M. O. Wiedorn, K. R. Beyerlein, D. A. Bushnel, E. G. Kovaleva, M. Heymann, L. Gumprecht, R. A. Kirian, A. Barty, V. Mariani, A. Tolstikova, L. Adriano, S. Awel, M. Barthelmess, K. Drner, L. P. Xavier, O. Yefanov, D. R. James, G. Nelson, D. Wang, G. Calvey, Y. Chen, A. Schmidt, M. Szczepek, S. Frielingsdorf, O. Lenz, E. Snell, P. J. Robinson, B. arler, G. Belak, M. Maek, F. Wilde, A. Aquila, S. Boutet, M. Liang, S. M. Hunter, P. Scheerer, J. D. Lipscomb, U. Weierstall, R. D. Kornberg, J. C. H. Spence, L. Pollack, H. N. Chapman, S. Bajt, *Scientific Reports* **2017**, *10*, 1–12.

[37] G. Nelson, R. A. Kirian, U. Weierstall, N. A. Zatsepin, T. Farag, T. Baumbach, F. Wilde, F. B. P. Niesler, B. Zimmer, I. Ishigami, M. Hikita, S. Bajt, S. Yeh, D. L. Rousseau, H. N. Chapman, J. C. H. Spence, M. Heymann, *Optics Express* **2016**, *24*, 261680.

[38] A. S. Soares, M. A. Engel, R. Stearns, S. Datwani, J. Olechno, R. Ellson, J. M. Skinner, M. Allaire, A. M. Orville, *Biochemistry* **2011**, *50*, 43994401.

[39] A. H. Lefebvre, *Atomization and sprays*, New York, Hemisphere, **1989**.

[40] L. Rayleigh, *Proc. R. Soc. Lond.* **1879**, *29*, 71–97.

[41] R. Zahoor, S. Bajt, B. Sarler, *Int. J. Hydromechatronics* **2018**, *1*, 222–237.

[42] O. Reynolds, *Phil. Trans. R. Soc. Lond.* **1883**, *174*, 935–982.

[43] C. Tropea, A. Yarin, J. F. Foss, *Handbook of Experiemntal Fluid Mechanics*, Spring, **2007**.

[44] R. E. Phinney, *AIChE Journal* **1972**, *18*, 432–434.

[45] D. P. Deponte, U. Weierstall, K. Schmidt, J. Warner, D. Starodub, J. C. H. Spence, R. B. Doak., *J. Phys. D: Appl. Phys* **2008**, *41*, 1–7.

[46] C. W. Mascosko, *Rheology Principles, Measurments and Applications.*, T. C. Wiley-VCH (Ed.), **1994**.

[47] R. W. Fenn, S. Middleman, *A. I. Ch. E. J.* **1969**, *15*, 379–383.

[48] S. P. Lin, R. D. Reitz., *Annu. Rev. Fluid Mech.* **1998**, *30*, 85–105.

[49] R. D. Reitz, F. V. Bracco, *Phys. Fluids* **1982**, *25*, 1730–1742.

[50] C. Dumouchel, *Exp. Fluids* **2008**, *45*, 371–422.

[51] D. Soederberg, Ph.D. thesis, Royal Institute of Technology- Department of Mechanics - Stockholm, **1999**.

[52] C. Weber, *ZAMM- J. of Applied Mathematics and Mechanics* **1931**.

[53] R. F. Probstein, *Physycschemical Hydrodynamics in Viscosity and Momentum Transport*, John Wiley & Sons , New York, **1994**.

[54] H. A. Barnes, *A handbook of Elementary Rheology*, Aberystwyth (Ed.), University of wales, Institute of Non-Newtonian Fluid Mechanics., **2000**.

[55] J. J. Stickel, R. L. Powell., *Annual Review of Fluid Mechanics* **2005**, *37*, 129–149.

[56] A. Guha, *Annu.Rev.Fluid Mech* **2008**, *40*, 311–341.

[57] A. Einstein, *Annalen der Physik* **1906**, *324*, 289–306.

[58] G. Batchelor, *Journal of Fluid Mechanics* **1972**, *52*, 245–268.

[59] I. M. Krieger, T. J. Dougherty, *Society of Rheology* **1959**, *137-152*, 3.

[60] N. J. Wagner, J. F. Brady, *Physics Today* **2009**, *62*, 27–32.

[61] T. J. Pedley, J. O. Kessler, *Annu. Rev. Fluid Mech.* **1992**, *24*, 313–358.

[62] M. B. Pinsky, A. P. Khain, *Atmos. Res.* **1998**, *47*, 69–86.

[63] J. A. Olson, R. J. Kerekes, *J. Fluid Mech.* **1998**, *377*, 47–64.

[64] G. B. Jeffery, *Proc. R. Soc. Lond. - A* **1922**, *102*, 161–179.

[65] G. I. Taylor, *Proc. R. Soc. Lond. - A* **1923**, *103*, 58–61.

[66] F. Toschi, E. Bodenschatz, *Annu. Rev. Fluid Mech.* **2009**, *41*, 375–404.

[67] F. Lundell, D. Soderberg, H. Alfredsson, *Annu. Rev. Fluid Mech.* **2011**, *43*, 195217.

[68] R. J. Kerekes, *N. P. and Paper Research J.* **2006**, *21*, 100–114.

[69] I. Teraoka, N. Ookubo, R. Hayakawa, *Phys Rev Lett* **1985**, *55*, 27122715.

[70] B. J. Trevelyan, S. G. Mason., *J. of Colloid Sci* **1951**, *6*, 354367.

[71] D. D. Carlo, *Lab. Chip* **2009**, *9*, 3038–3046.

[72] D. Z. Gunes, R. Scirocco, J. Mewis, J. Vermant, *Journal of Non-Newtonian Fluid Mechanics* **2008**, *155*.

[73] C. M. Zettner, M. Yoda., *J. Fluid Mech.* **2001**, *442*, 241266.

[74] M. Trebbin, D. Steinhauser, J. Perlich, A. Buffet, S. V. Roth, W. Zimmermann, J. Thiele, S. Förster, *PNAS* **2013**, *110*, 6706–6711.

[75] T. Rosen, C. Brouzet, S. V. Roth, F. Lundell, L. D. Soderberg, *arXiv:1711.02489v1 [cond-mat.soft]* **2017**.

[76] O. Bernstein, M. Shapiro, *J. Aerosol Science* **1994**, *25*, 113136.

[77] M. Parsheh, M. Brown, C. Aidun, *J. Fluid Mech.* **2005**, *545*, 245269.

[78] J. Als-Nielsen, *Elements of modern X-ray Physics 2nd ed.*, John Wiley and Sons, Ltd Publication, **2011**.

[79] B. D. Cullity, *Elements of X-ray Diffraction 2nd ed.*, E. M. Cohen (Ed.), Addison-Wesley Publishing Company Inc., Reading Massachusetts, USA., **1959**.

[80] C. Markert, B. Fischer, J. Wagner., *J. Appl. Cryst.* **2011**, *44*, 441–447.

[81] T. W. Hamann., *Dalton Trans.* **2012**, *41*, 7830.

[82] F. S. Freyria, B. Bonelli, M. Tomatis, M. Ghiazza, E. Gazzano, D. Ghigo, E. Garrone, B. Fubini., *Chem. Res. Toxicol.* **2012**, *25*, 850861.

[83] Y. Lin, G. Yuan, S. Sheehan, S. Zhou, D. Wang, *Energy Environ. Sci.* **2011**, *4*, 4862.

[84] A. K. Patra, S. K. Kundu, A. B. Kim, *Nanoscale* **2016**, *8*, 365–377.

[85] F. Bodker, M. Hansen, C. Koch, K. Lefmann, S. Morup, *Phys. Rev. B* **2000**, *61*.

[86] T. Neuberger, B. Schpf, H. Hofmann, M. Hofmann, B. von Rechenberg, *J. Magn. Magn. Mater.* **2005**, *293*.

[87] F. Bodker, S. Morup, M. S. Pedersen, P. Svedlindh, G. T. Jonsson, J. L. Garcia-Palacios, F. J. Lazaro, *J. Magn. Magn. Mater.* **1998**, *177-181*.

[88] Z. Jing, S. Wu, *Mater. Letters* **2004**, *58*, 3637–3640.

[89] R. Strobel, S. E. Pratsinis, *Adv. Powder Technol.* **2009**, *20*.

[90] R. C. Chikate, K. Jun, C. V. Rode, *Polyhedron* **2008**, *27*, 933–938.

[91] T. Sugimoto, Y. Wang, H. Itoh, A. Muramatsu, *Colloids and Surfaces A: Physicochemical and Engineering Aspects* **1998**, *134*, 265–279.

[92] R. Zboril, M. Mashlan, D. Petridis, *Chem. Mater.* **2002**, *14*, 969–982.

[93] R. Vandenberghe, E. V. San, E. D. Grave, *Czech. J. Phys.* **2001**, *51*, 663–675.

[94] M. Ozaki, S. Kratohvil, E. Matijevi, *J. Colloid Interface Sci.* **1984**, *102*, 146–151.

[95] A. Nack, J. Seifert, C. Passow, J. Wagner, *J. Appl. Cryst.* **2018**, *51*, 1–10.

[96] W. Wu, X. Xiao, S. Zhang, J. Zhou, L. Fan, F. Ren, C. Jiang, *J. Phys. Chem. C* **2010**, *114*, 16092–16103.

[97] S. Mitra, S. Das, K. Mandal, S. Chaudhuri, *Nanotechnology* **2007**, *18*, 1–9.

[98] V. Pecharsky, P. Zavalij, *Fundamentals of Powder Diffraction and Structural Characterization of Materials*, N. Y. Second Springer (Ed.), **2009**.

[99] A. M. Ganan-Calvo, D. P. DePonte, M. A. Herrada, J. C. H. Spence, U. Weierstall, R. B. Doak, *Small* **2010**, *6*, 822–824.

[100] A. V. Zozulya, S. Bondarenko, A. Schavkan, F. Westermeier, G. Grubel, M. Sprung, *Optic Express* **2012**, *20*, 18967– 18976.

[101] F. Lehmkühler, I. Steinke, M. Schroer, B. Fischer, M. Sprung, G. Grübel, *J. Phys. Lett.* **2017**, *8*, 3581–3585.

[102] S. Monjezi, J. D. Jones, A. K. Nelson, J. Park, *Nanomaterials* **2018**, *8*, 1–19.

[103] C. Passow, Ph.D. thesis, Mathematisch-Naturwissenschaftlichen Fakultt der Universitt Rostock, **2015**.

[104] J. Wagner, C. Markert, B. Fischer, L. Muller, *PRL* **2013**, *110*, 1–5.

[105] J. A. Sellberg, C. Huang, A. T. McQueen, N. D. Loh, H. Laksmono, D. Schlesinger, R. G. Sierra, D. Nordlund, C. Y. Hampton, D. Starodub, D. P. DePonte, M. Beye, C. Chen, A. V. Martin, A. Barty, K. T. Wikfeldt, T. M. Weiss, C. Caronna, J. Feldkamp, L. B. Skinner, M. M. Seibert, M. Messerschmidt, G. J. Williams, S. Boutet, L. G. M. Pettersson, M. J. Bogan, A. Nilsson, *Nature* **2014**, *510*, 381–384.

[106] A. P. Leong, X. Yu, Z. H. Zhou, G. J. Jensen, *Methods Enzymol.* **2010**, *482*.

[107] D. A. Shapiro, H. N. Chapman, D. DePonte, R. B. Doak, P. Fromme, G. Hembree, M. Hunter, S. Marchesini, K. Schmidt, J. Spence, D. Starodub, U. Weierstall, *J. Synchtron Rad.* **2008**, *15*, 593–599.

[108] M. R. Wilson, *Jourbal of Molecular Liquids* **1996**, *68*, 23–31.

[109] R. Zahoor, S. Bajt, B. Sarler, *Int. J. of Multiphase Flow* **2018**, 1.

[110] M. Schlenk, E. Hofmann, S. Seibt, S. Rosenfeldt, L. Schrack, M. Drechsler, A. Rothkirch, W. Ohm, J. Breu, S. Gekle, S. Frster, *Langmuir* **2018**, *34*, 4843–4851.

[111] P. Butler, *Curr Opin Colloid Interface Sci.* **1999**, *4*, 214–221.

[112] D. Popp, N. D. Loh, H. Zorgati, U. Ghoshdastider, L. T. Liow, M. I. Ivanova, M. Larsson, D. P. DePonte, R. Bean, K. R. Beyerlein, C. Gati, D. Oberthuer, D. Arnlund, G. Brnden, P. Berntsen, D. Cascio, L. M. G. Chavas, J. P. J. Chen, K. Ding, H. Fleckenstein, L. Gumprecht, R. Harimoorthy, E. Mossou, M. R. Sawaya, A. S. Brewster, J. Hattne, N. K. Sauter, M. Seibert, C. Seuring, F. Stellato, T. Tilp, D. S. Eisenberg, M. Messerschmidt, G. J. Williams, J. E. Koglin, L. Makowski, R. P. Millane, T. Forsyth, S. Boutet, T. A. White, A. Barty, H. Chapman, S. L. Chen, M. Liang, R. Neutze, R. C. Robinson., *Cytoskeleton* **2017**, *74*, 471–481.

[113] R. Zahoor, G.Bela, S. Bajt, B. arler, *Microfluidics and Nanofluidics* **2018**, *22*, 1–20.

[114] T. Rosen, N. Mittal, S. V. Roth, P. Zhang, L. D. Soderberg, F. Lundell, *arXiv:1801.07558 [cond-mat.soft]* **2018**.

[115] B. Marmiroli, F. Cacho-Nerin, B. Satori, J. Perez, H. Amenitsch, *J. Synchtron Rad.* **2014**, *21*, 193–201.

[116] M. P. Hentschel, R. Hosemann, A. Lange, B. Uther., *Acta Cryst.* **1987**, *A43*, 506–513.

[117] M. Priebe, S. Kalbfleisch, M. Tolkiehn, S. Kster, B. Abel, R. J. Davies, T. Salditt, *New Journal of physics* **2010**, *12*, 2–11.

[118] J. Plomp, J. G. Barkerb, V. de Haana, W. Bouwmana, A. van Wella, *Nuclear Instruments and Methods in Physics Research A* **2007**, *574*, 324–329.

[119] D. T. Grubb, N. S. Murth, *Macromolecules Article* **2010**, *43*, 1016–1027.

[120] C. G. Schroer, I. Agapov, W. Brefeld, R. Brinkmann, Y.-C. Chae, H.-C. Chao, M. Eriksson, J. Keil, X. N. Gavald, R. Rhlsberger, O. H. Seeck, M. Sprung, M. Tischer, R. Wanzenberg, E. Weckert, *J. Synchrotron Rad.* **2018**, *25*, 1–14.

[121] E. Weckert, *IUCrJ* **2015**, *2*, 230–245.

[122] G. Grübel, F. Zontone, *J. Alloys Compd.* **2004**, *362*, 3–11.

[123] G. Grübel, A. Madsen, A. Robert, *X-ray photon correlation spectroscopy (XPCS) in Soft Matter Characterization*, Springer Netherlands., **2008**.

[124] A. Madsen, A. Fluerasu, B. Ruta., *Synchrotron Light Sources and Free-Electron Lasers*, Springer International Publishing, **2015**.

[125] O. G. Shpyrko, *J. Synchrotron Rad.* **2014**, *21*, 1057–1064.

[126] H. N. Chapman, P. Fromme, A. Barty, R. A. White, T. A.and Kirian, A. Aquila, M. S. Hunter, J. Schulz, D. P. DePonte, U. Weierstall, R. B. Doak, F. R. N. C. Maia, A. V. Martin, I. Schlichting, L. Lomb, N. Coppola, R. L. Shoeman, S. W. Epp, R. Hartmann, D. Rolles, A. Rudenko, L. Foucar, N. Kimmel, G. Weidenspointner, P. Holl, M. Liang, M. Barthelmess, S. Caleman, C.and Boutet, J. Bogan, M. J.and Krzywinski, S. Bostedt, C.and Bajt, L. Gumprecht, B. Rudek, B. Erk, A. Schmidt, C.and Hoemke, D. S. L. Reich, C.and Pietschner, G. Hauser, H. Gorke, J. Ullrich, S. Herrmann, G. Schaller, F. Schopper, H. Soltau, K.-U. Kuehnel, M. Messerschmidt, S. P. Bozek, J. D.and Hau-Riege, M. Frank, C. Y. Hampton, R. G. Sierra, D. Starodub, G. J. Williams, J. Hajdu, N. Timneanu, M. M. Seibert, J. Andreasson, A. Rocker, O. Joensson, M. Svenda, S. Stern, K. Nass, R. Andritschke, C.-D. Schroeter, F. Krasniqi, M. Bott, K. E. Schmidt, X. Wang, I. Grotjohann, J. M. Holton, T. R. M. Barends, R. Neutze, S. Marchesini, R. Fromme, S. Schorb, D. Rupp, M. Adolph, T. Gorkhover, I. Andersson, H. Hirsemann, G. Potdevin, H. Graafsma, B. Nilsson, J. C. H. Spence, *Nature* **2011**, *470*, 73–77.

[127] S. Boutet, L. Lomb, G. J. Williams, T. R. M. Barends, A. Aquila, R. B. Doak, U. Weierstall, D. P. DePonte, R. L. M. M. Steinbrener, J.and Shoeman, A. Barty, T. A. White, S. Kassemeyer, R. A. Kirian, M. M. Seibert, P. A. Montanez, C. Kenney, R. Herbst, P. Hart, J. Pines, G. Haller, S. M. Gruner, H. T. Philipp, M. Tate, M. W.and Hromalik, L. J. Koerner, N. v. . Bakel, J. Morse, D. Ghonsalves, W.and Arnlund, M. J. Bogan, C. Caleman, R. Fromme, C. Y. Hampton, M. S.

Hunter, L. C. Johansson, G. Katona, C. Kupitz, M. Liang, A. V. Martin, K. Nass, L. Redecke, N. W. D. Z. N. A. Stellato, F.and Timneanu, D. Schafer, J. Defever, R. Neutze, P. Fromme, J. C. H. Spence, H. N. Chapman, I. Schlichting, *Science* **2012**, *337*, 362–364.

[128] F. Lehmkühler, P. Kwasniewski, W. Roseker, B. Fischer, M. Schroer, K. Tono, T. Katayama, M. Sprung, M. Sikorski, S. Song, J. Glownia, M. Chollet, S. Nelson, A. Robert, C. Gutt, M. Yabashi, T. Ishikawa, G. Grübel., *Sci. Rep.* **2015**, *5*, 17193.

[129] M. O. Wiedorn, S. Awel, A. J. Morgan, K. Ayyer, Y. Gevorkov, H. Fleckenstein, N. Roth, L. Adriano, R. Bean, K. R. Beyerlein, J. Chen, J. Coe, F. Cruz-Mazo, T. Ekeberg, R. Graceffa, M. Heymann, D. A. Horke, J. Knoska, V. Mariani, R. Nazari, D. Oberthür, A. K. Samanta, R. G. Sierra, C. A. Stan, O. Yefanov, D. Rompotis, J. Correa, B. Erk, R. Treusch, J. Schulz, B. G. Hogue, A. M. Ganan-Calvo, P. Fromme, J. Küpper, A. V. Rode, S. Bajt, R. A. Kiriang, H. N. Chapman, *IUCrJ* **2018**, *5*, 1–11.

[130] C. Goy, M. A. C. Potenza, S. Dedera, M. Tomut, E. Guillerm, A. Kalinin, K. Voss, A. Schottelius, N. Petridis, A. Prosvetov, G. Tejeda, J. M. Fernández, C. Trautmann, F. Caupin, U. Glasmacher, R. E. Grisenti., *Physical Review Letters* **2018**, *120*, 1–6.

Own publications

Publications directly related to the thesis

1. I. Steinke, M. Walter, F. Lehmkühler, J. Valerio et al. Rev. Sci. Instrum. 87, 063905 (2016)

Publications not directly related to the thesis

1. J. Valerio, S. Bernstorff, S.S. Funari. Eur. Pharm. J., 64, 1, (2017)

2. Z. Yin, H. Löche, J. Rehanek, C. Goy, A. Kalinin, A. Schottelius, F. Trinter, P. Miedema, A. Jain, J. Valerio, P. Busse, F. Lehmkühler, J. Möller, G. Grübel, A. Madsen, J. Viefhaus, R. E. Grisenti, M. Beye, A. Erk, S. Techert. X-ray spectroscopy with variable line spacing based on reflection zone plate optics. $Optic\ letters\ in\ print\ (DOCID: 339934)$.

3. F. Lehmkühler, J. Valerio, D. Sheyfer, W.Roseker, M. A. Schroer, B. Fischer,K. Tono, M. Yabashi, T. Ishikawae and G. Grübel. Dynamics of soft nanoparticle suspensions at hard X-ray FEL sources below the radiation damage threshold. $In\ review$.

Declaration on oath

”I hereby declare on oath, that I have written the present dissertation by my own and have not used other than the acknowledged resources and aids. The submitted written version corresponds to the version on the electronic storage medium. I hereby declare that I have not previously applied or pursued for a doctorate (Ph.D. studies).

.....

Date, signature

Acknowledgements

Firstly, I would like to express my sincere gratitude to my supervisor Prof. Dr. Gerhard Grübel and my co-supervisor Prof. Dr. Horst Weller for giving me the opportunity to work on this project, and the financial support to DESY and PIER. To Prof. Dr. Gerhard Grübel I am thankful for welcoming me in his group where I scientifically grew up. For all his support on my Ph.D topic and related research, for sharing his immense knowledge, enthusiasm and insightful comments. I am proud to be part of your group.

Besides my advisor, I would like to thank to Dr. Felix Lehmkühler his guidance helped me in all the time of research. I benefit a lot from his motivations and expertise and the fruitful discussions. I could not have imagined this thesis writing process without his support and his green pen. Thank you very much Felix!

I would like to thank the rest of my group colleagues with whom I shared my last four years, thanks for being always present.

First, to colleagues I shared the office Dina Sheyfer, Michael Koof, Nele Striker, Martin A. Schroer, and Magnus Berntsen thank you guys for all scientific and non-scientific fruitful discussions coffees and the fun moments together.

To Felix Lehmkühler for being always friendly and a very good adviser in science and non-science related topics, thanks as well for the beers together and fun times.

I would like to thank to Ingo Steinke for all his support at the beginning, to share with me his expertise in the liquid jets topic. For our scientific and non-scientific enjoyable discussions.

To Michael Walther, who helped me with the liquid jet setup improvements, his support before and during the beamtimes.

I thank as well as to Torben Kalff for his good work during his bachelor thesis and the invaluable help during the beamtime.

Thanks to Verena Markmann for her help, the liquid jet project continues in ”good hands”.

To Avni Jain to share with me her love and knowledge for science and to be always friendly.

To Irina Lokteva for our long and fruitful discussions science and non-science related, her advice and her precious help. Thanks for our coffees and lunch discussions, thank you for being my friend.

To Lara Frenzel to be a very friendly colleague. Always ready to help, thanks for our conversations, thanks for the fun, beers and runs together.

To Wojciech Roseker for giving me always good advices, his corrections, and help. Thank you to be the boss of our running group, thanks for our serious and non-serious conversations, coffees, fun moments and beers.

To Michael Koof to be always ready to help, our fruitful discussions, his constant help. I thank him as well for the caffeine time, in short to be my friend.

To Dina Sheyfer as well, thank you very much for every moment we shared during this time (and were a lot). Thanks for the coffees, and to be always present.

To Rustam Rysov for being very friendly, always ready to help with everything, thanks Rustam for your support.

Leonard Mueller, Andre Kobs, and Matthias Riepp despite the different topics they were very nice colleagues always supporting in giving good advices.

To Donatella Rosetti, thanks to be always friendly and ready to help.

Many thanks as well to P10 beamline (PETRA III) staff for the technical support during the experiments: Dr. Michael Sprung, Dr. Alexey Zozulya, Dr. Fabian Westermeier and Daniel Weschke. As well as to all my collaborators who provide their support for the success of the beamtimes: Dr. Martin Schroer, Dr. Michael Höltig, Dr. Irina Lokteva, Dr. Ingo Steinke, Dr. Felix Lehmkühler, Dr. Avni Jain, Dr. Dina Sheyfer, Lara Frenzel, Michael Koof, Michael Walther, Torben Kalff, Dr. Jyotsana Lal, Prof. Dr. Martin Trebbin, Dr. Diana Monteiro, Dr. Sebastian Bommel, Mohammad Vakili and Ramakrishna Vasireddi. Thank you very much to all for the sleepless nights we were working together and for the stimulating discussions.

Furthermore, I would like to thank Dr. Irina Lokteva, Dr. Birgit Fischer and Dr. Andreas Korwowski for the samples characterization. To Dr. Dina Sheyfer, Dr. Felix Lehmkühler and Dr. Michael Sprung for their help with model studies.

My sincere thanks also go to Dr. Sergio S. Funari, who opened for me the DESY doors. Thank you, Sergio, to be always present. I benefit a lot from his huge experience not only scientific but as well as a friend.

Now to my Portuguese crew:

Ao Prof. Dr. Eurico Melo, o meu ”padrinho da ciência” muito obrigada por tudo o que me transmitiu e ainda me ensina. Este trabalho também é um pouco seu.

Aos amigos que Hamburgo me deu: Diana, Joana, Isabel, Guida e familia o meu muito obrigada, a vossa presenca na minha vida tornou esta caminhada muito mais fácil e sempre com um sorriso.

A toda a minha famlia que sempre me apoiou, especialmente aos meus pais e á minha irmã. Uma parte deste trabalho também é vossa, aos meus pais por saberem dar o ”empurrão” no momento exacto, sempre presentes em todas as minhas decisões. Á minha irmã por ser uma parte de mim e quem me ensinou o que é sentir tanto orgulho em alguém.

Last but not the least, ao Luís por ”embarcar” em tudo comigo nestes longos anos.